Design of a pacemaker for animal biomedical research on pulmonary arterial hypertension

Fanny Pan

université PARIS-SACLAY

Design of a pacemaker for animal biomedical research on pulmonary arterial hypertension

Développement d'un pacemaker pour la recherche biomédicale animale dans le cadre de l'hypertension artérielle pulmonaire

Thèse de doctorat de l'université Paris-Saclay

École doctorale n° 575, Electrical, optical, bio-physics and engineering (EOBE)
Spécialité de doctorat: Electronique, Photonique et Micro-Nanotechnologies
Graduate School: Sciences de l'ingénierie et des systèmes
Référent: Faculté des sciences d'Orsay

Thèse préparée dans le **Laboratoire de Génie Electrique et Electronique de Paris**, (Université Paris-Saclay, CentraleSupélec, CNRS)
sous la direction d'**Anthony KOLAR**, Maître de Conférences,
et le co-encadrement d'**Emilie AVIGNON-MESELDZIJA**, Maîtresse de Conférences

Thèse soutenue à Paris-Saclay, le 27 mars 2024, par

Fanny PAN

Composition du jury

Membres du jury avec voix délibérative

Souhil MEGHERBI Professeur des universités, Université Paris Saclay	Président
Rachid BOUCHAKOUR Professeur des universités, IM2NP, Aix-Marseille Université	Rapporteur & Examinateur
Sylvain FERUGLIO Maître de conférences HDR, LIP6, Sorbonne Université	Rapporteur & Examinateur
Catherine ALGANI Professeur des universités, CNAM EPN EEAM-EASY	Examinatrice

THESE DE DOCTORAT

NNT : 2024UPAST029

université PARIS-SACLAY

ÉCOLE DOCTORALE
Physique et ingénierie : Electrons, Photons, Sciences du vivant (EOBE)

Titre: Développement d'un pacemaker pour la recherche biomédicale animale dans le cadre de l'hypertension artérielle pulmonaire.....
Mots clés: Stimulateur cardiaque, Rat, Circuit intégré, Hypertension artérielle pulmonaire

Résumé: L'hypertension artérielle pulmonaire (HTAP) est une maladie cardiovasculaire progressive et rare touchant entre 15 et 50 individus pour 1 million dans le monde. Elle se caractérise par une élévation anormale de la pression au niveau des artères pulmonaires, pouvant conduire à une insuffisance cardiaque droite sévère, et demeure à ce jour incurable.

La recherche biomédicale sur les maladies cardiovasculaires s'appuie largement sur l'utilisation de modèles animaux, notamment les rats, pour étudier une pathologie sur l'ensemble de leur durée de vie, avec un échantillon de population important. La fréquence cardiaque est fortement impliquée dans l'émergence et la progression de nombreuses maladies, ce qui en fait une cible thérapeutique très intéressante. Dans l'optique d'explorer son impact sur la progression de l'HTAP, ces travaux ont pour objectif de développer un pacemaker programmable implantable chez le petit animal. Les pacemakers sont des dispositifs médicaux implantés délivrant des impulsions électriques au cœur afin de déclencher sa contraction. Dans le cadre de cette thèse, notre attention s'est portée sur la conception de la partie fondamentale d'un pacemaker : la stimulation. La documentation existante sur les stimulateurs cardiaques tend à être limitée et protégée, notamment celle concernant les circuits de stimulation. Ainsi, les objectifs de ces travaux sont doubles : expérimenter et valider *in vivo* une onde stimulatrice adéquate et concevoir un circuit pour la générer qui soit potentiellement implantable, c'est-à-dire dans une technologie intégrée et de très faible consommation.

Des expériences *in vivo* réalisées avec un prototype FPGA sur des rats à l'Hôpital Marie Lannelongue ont validé non seulement la forme d'onde, mais aussi les ordres de grandeur électriques et temporels nécessaires pour une stimulation efficace et sans risque pour l'animal. Ces résultats nous permettent de fixer le cahier des charges pour le développement du circuit intégré d'un générateur d'impulsions avec une méthodologie reposant sur la conception d'éléments ultra-faible consommation. Le circuit et les simulations ont été réalisés en 0,18 µm, dans la technologie XFAB XH018.

L'architecture proposée repose sur un pont en H et permet, avec le jeu de commande adapté, de générer une stimulation biphasique de fréquence programmable. Elle est de plus composée de deux multiplicateurs de tension commandés par un oscillateur dans le domaine du kHz et d'un oscillateur à relaxation dans la gamme de la dizaine de Hz. Afin de minimiser la consommation totale du circuit, ce second oscillateur a été conçu suite à une étude de l'état de l'art des techniques ultra-faible consommation (e.g., Stacking, Reverse Body Biasing, Dynamic Leakage Suppression Logic - DLS), qui a conduit à la conception *ad hoc* de portes logiques de type DLS. Cette technique récente, réservée à des opérations basse fréquence (<100 Hz), consiste en l'ajout, à une porte logique standard, d'un NMOS relié à Vdd et d'un PMOS relié à GND, et dont les grilles bouclent sur la sortie, ce qui permet de placer les transistors dans un état de 'super-cut-off', et donc de réduire drastiquement les fuites de courant.

L'ensemble du circuit de stimulation consomme 112 µW dont 100 µW sont directement consommés par le pont en H pour la stimulation du cœur qui a besoin de deux impulsions d'au moins 30 µA par période d'onde comme établi grâce aux tests *in vivo*. La partie oscillateur dans le domaine du kHz avec ses remises en forme et l'un des multiplicateurs consomme 9,9 µW. Enfin, grâce à l'approche ultra-faible consommation adoptée dans cette conception, l'ensemble oscillateur à relaxation et synthèse de commande ne consomme que 1,8 µW soit 1,6 % de l'ensemble du circuit.

Le circuit proposé génère ainsi une impulsion biphasique à des fréquences comprises entre 6,8 et 10,1 Hz, soit 400 et 600 bpm, répondant au cahier des charges pour une stimulation chez le petit animal dans le cadre de l'étude de l'HTAP.

Title: Design of a pacemaker for animal biomedical research on pulmonary arterial hypertension

Keywords: Artificial pacemaker, Rat, Integrated circuit, Pulmonary arterial hypertension

Abstract: Pulmonary arterial hypertension (PAH) is a rare, progressive cardiovascular disease that affects an average of 15 to 50 individuals per 1 million worldwide. It is characterized by an abnormal rise in pressure in the pulmonary arteries, which can lead to severe right heart failure, and remains incurable to this day.

Biomedical research on cardiovascular diseases heavily relies on the use of animal models, particularly rats, which allow for the study of a pathology over their entire lifespan, with a large sample population. Heart rate is strongly implicated in the onset and progression of many pathologies, making it a very interesting therapeutic target. In the pursuit of exploring its impact on the progression of PAH, the objective of this work is to develop a programmable pacemaker that can be implanted in small animals.

Pacemakers are implanted medical devices delivering electrical impulses (stimulation) to the heart to trigger its contraction. In this thesis, we focused on the design of the fundamental part of a pacemaker: pacing. Existing literature on pacemakers tends to be limited and safeguarded, particularly regarding stimulation circuits. Hence, our work had two main objectives: to test and validate *in vivo* a suitable pacing waveform, and to design a circuit for generating it that is potentially implantable, i.e. in an integrated technology and with a very low power consumption.

In vivo experiments conducted using an FPGA prototype on rats at the Marie Lannelongue Hospital validated not only the shape of the stimulating waveform but also the electrical and temporal orders of magnitude required for efficient and safe animal stimulation. These results allowed us to set the specifications for designing an integrated pulse generator circuit, employing a methodology centered around the design of ultra-low power elements. The circuit and simulations were implemented using XFAB XH018 0.18 µm technology.

The proposed architecture is based on an H-bridge structure and, with the appropriate control set, can generate a biphasic stimulation at a programmable frequency. It also comprises two voltage multipliers controlled by an oscillator in the kHz range and a relaxation oscillator in the ten Hz range. In order to minimize the total power consumption of the circuit, this second oscillator was designed following a state-of-the-art study of ultra-low power techniques (e.g., Stacking, Reverse Body Biasing, Dynamic Leakage Suppression Logic - DLS), which led to the *ad hoc* design of DLS logic gates. This novel technique, reserved for low frequency operations (<100 Hz), consists of adding, to a standard CMOS gate, a header NMOS connected to Vdd and a footer PMOS connected to ground, with their gate looped on the output node, driving the transistors in a 'super-cut-off' state, thus drastically reducing current leakage. The entire stimulation circuit consumes 112 µW, of which 100 µW is consumed directly by the H-bridge for the stimulation of the heart, which requires two pulses of at least 30 µA per wave period, as established by the *in vivo* tests. The oscillator in the kHz range with its reshaping and one of the multipliers consumes 9.9 µW. Finally, thanks to the ultra-low power approach adopted in this design, the relaxation oscillator and control synthesis assembly consume only 1.8 µW, i.e. 1.6 % of the stimulation circuit's total consumption.

Therefore, the proposed circuit generates a biphasic impulse at frequencies ranging between 6.8 and 10.1 Hz, translating to 400 and 600 bpm, meeting the specifications for small animal stimulation within the scope of studying PAH.

Remerciements

Ce manuscrit est le fruit de trois années de doctorat pleines de rebondissements et je tiens à exprimer ma profonde gratitude à toutes les personnes qui ont contribué de près ou de loin à sa réalisation.

Tout d'abord, je remercie chaleureusement l'ensemble des membres de mon jury de thèse d'avoir accepté de faire partie de ce comité et pour l'intérêt porté à mon travail: Messieurs Rachid Bouchakour et Sylvain Feruglio en qualité de rapporteurs et Madame Catherine Algani et Monsieur Souhil Megherbi en tant qu'examinateurs. Je tiens également à exprimer ma reconnaissance à Messieurs Robert Sobot et Mathieu Thevenin, qui ont par ailleurs fait partie de mon comité de suivi. Ce fut un plaisir d'échanger avec vous.

J'aimerais remercier Madame Delphine Mika, et Messieurs David Boulate et Frédéric Perros, initiateurs de ce projet, pour toute l'aide et l'expertise qu'ils ont pu apporter et les moyens mis en place pour les expériences in vivo. Cette thèse n'aurait littéralement pas vu le jour sans vous.

Je remercie vivement ma formidable équipe encadrante, composée de mon directeur Anthony Kolar et ma co-encadrante Emilie Avignon-Meseldzija, pour leurs conseils, leur disponibilité et leur contribution tout au long de cette grande aventure académique. Merci de m'avoir permis d'évoluer dans un environnement plein de bienveillance.

Merci à l'ensemble des membres du département Electronique, pour leur gentilesse, en particulier Béa sans qui ces trois années auraient été beaucoup moins sympathiques, et Hugo avec qui nous formions le trio CSEI. Et un grand merci à l'équipe de volley et du body balance pour tous les bons moments passés.

J'aimerais aussi exprimer ma profonde gratitude à ma famille, belle-famille et mes amis pour leur soutien moral tout au long de ces trois années, avec une mention spéciale pour Martin et Vincent U. pour avoir lu et corrigé mon manuscrit. Votre aide fut des plus précieuses.

Enfin je souhaite dédier une reconnaissance toute particulière à Martin pour son soutien inconditionnel, sa patience et sa compréhension pendant les moments de doute et de stress qui ont accompagnés cette thèse. Sa présence a été le pilier sur lequel j'ai pu m'appuyer dans ces moments difficiles (et oh combien ils étaient nombreux !).

List of acronyms and abbreviations

Acronyms and abbreviations in brackets are those used in the French summary of the thesis.

AV	Atrioventricular
bpm	Beats per minute
BL	Baseline
BPEG	British Pacing and Electrophysiology Group
CF (FC)	Cardiac frequency (Fréquence cardiaque)
CPM	Conventional pacemaker
CO (DC)	Cardiac output (Débit cardiaque)
CRT	Chronic resynchronization therapy
CTAT	Complementary to Absolute Temperature
CVD	Cardiovascular disease
DAP	Diastolic arterial pressure
DAC (CNA)	Digital to analog converter (Convertisseur numérique-analogique)
DCP	Dickson charge pump
DIBL	Drain Induced Barrier Lowering
DLS	Dynamic leakage suppression
DVM	Dickson voltage multiplier
ECG	Electrocardiogram
EMI	Electromagnetic interference
FDA	Food and Drug Administration
FPGA	Field-programmable gate array
HR	Heart rate
IC	Integrated circuit
IVA	Ivabradine
LPM	Leadless pacemaker
LV	Left ventricle
LUT	Look-up table
MAP	Mean arterial pressure
mPAP (PAPm)	Mean pulmonary arterial pressure (Pression artérielle pulmonaire moyenne)
NASPE	North American Society of Pacing and Electrophysiology
PAH (HTAP)	Pulmonary arterial hypertension (Hypertension artérielle pulmonaire)
PCB	Printed circuit board
PTAT	Proportional to Absolute Temperature
PVR (RVP)	Pulmonary vascular resistance (Résistance vasculaire pulmonaire)
PVT	Process, voltage and temperature
PWP	Pulmonary wedge pressure

RBB	Reverse body biasing
ROSC	Relaxation oscillator
RV	Right ventricle
SAN	Sinoatrial node
SAP	Systolic arterial pressure
SV (VES)	Stroke volume (Volume d'éjection systolique)
TPR (RPT)	Total pulmonary resistance (Résistance pulmonaire totale)
ULP	Ultra-low power
VCO	Voltage controlled oscillator
WHO	World Health Organisation
WSPH	World Symposium on Pulmonary Hypertension
WU	Wood Units
XOSC	Crystal oscillator

Contents

List of Figures

List of Tables

Résumé de la thèse en Français

Chapitre 1 : Le cœur et les stimulateurs cardiaques

L'hypertension artérielle pulmonaire

L'hypertension artérielle pulmonaire (HTAP) est une maladie cardiovasculaire chronique rare qui affecte en moyenne 15 à 50 individus pour 1 million dans le monde, et se manifeste le plus souvent chez les femmes âgées de 30 à 60 ans [1]. Elle se caractérise par une élévation anormale de la pression au niveau des artères pulmonaires, ce qui peut entrainer une insuffisance cardiaque droite sévère. C'est une maladie progressive qui provoque l'épaississement et la rigidification des parois des artères pulmonaires, rendant plus difficile la circulation du sang dans ces dernières (Figure 1). Il en résulte une augmentation de la pression artérielle pulmonaire moyenne (PAPm), c'est-à-dire la pression mesurée avant que le sang n'arrive aux poumons, et une augmentation de la résistance vasculaire pulmonaire (RVP), ce qui oblige le côté droit du cœur à fournir un effort plus conséquent pour pomper le sang dans les poumons.

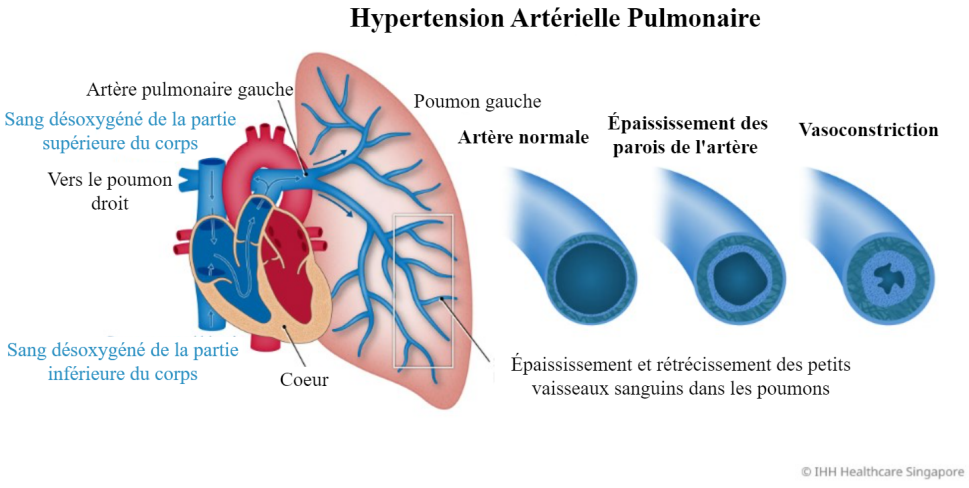

Figure 1: L'hypertension artérielle pulmonaire (figure extraite de [2])

Les premiers symptômes se manifestent, entre autres, sous forme de fatigue extrême, de palpitations, de syncopes ou d'essoufflement lors d'efforts intenses en premier lieu puis, lorsque la maladie progresse, lors d'activités quotidiennes. Ces symptômes sont relativement communs pour cette catégorie de pathologie, ce qui conduit souvent à un diagnostic tardif. Malgré l'existence de nombreux traitements palliatifs pharmacologiques (anticoagulants, vasodilatateurs, oxygénothérapie) ou chirurgicaux pour les cas plus sévères (transplantation cardiopulmonaire), l'HTAP demeure à ce jour incurable. Les recherches en cours continuent à explorer de potentielles interventions thérapeutiques [3, 4, 5].

Dans ce contexte de maladie cardiaque, la fréquence cardiaque (FC) joue un rôle crucial car le débit cardiaque (DC), soit la quantité de sang pompée par le cœur, dépend de cette fréquence cardiaque - en plus du volume d'éjection systolique (VES)-, et intervient dans le calcul de la résistance pulmonaire totale (RPT) comme le montrent les équations suivantes.

$$DC[L/min] = FC[/min] \cdot VES[L] \tag{1}$$

$$RPT = \frac{PAPm}{DC} \tag{2}$$

D'après les équations 1 et 2, il est raisonnable de supposer que l'abaissement de la fréquence cardiaque puisse ralentir l'augmentation de la résistance pulmonaire. Cette hypothèse constitue la base de l'exploration de l'influence potentielle de la modulation de la fréquence cardiaque sur la physiopathologie de l'HTAP, ouvrant la voie à un nouvel axe de recherche pour un traitement curatif. Dans le domaine de la recherche cardiovasculaire, les études sur des modèles animaux permettent d'obtenir de précieuses informations sur le fonctionnement de la maladie et d'étudier de potentielles stratégies de traitement. Bien qu'aucun modèle animal ne soit idéal, les rats sont particulièrement utilisés pour l'étude de maladies telles que l'HTAP. Cela est dû notamment à plusieurs similarités anatomiques et physiologiques avec l'Homme, mais aussi à leur coût relativement faible et leurs cycles de reproduction courts qui en font un choix pratique et rentable pour mener des expériences contrôlées et des études de long terme. Dans cette optique, le déploiement d'un stimulateur cardiaque contrôlable, implantable chez le petit animal, devient essentiel.

Les stimulateurs cardiaques

Les stimulateurs cardiaques sont des dispositifs médicaux implantables conçus pour délivrer des impulsions électriques contrôlées au cœur, semblables à celles générées naturellement par le nœud sinusal, afin d'assurer une activité cardiaque régulière et efficace. Les stimulateurs cardiaques traditionnels, couramment appelés pacemakers, se composent de deux éléments principaux : un

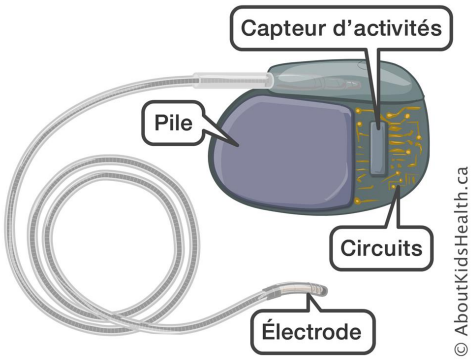

Figure 2: Le stimulateur cardiaque (figure extraite de [7])

générateur d'impulsions, abritant les circuits électroniques et la batterie (qui représente une part importante de la taille et du poids du dispositif), et de sondes, qui établissent la connexion entre le boîtier et les tissus cardiaques, à la fois pour surveiller l'activité cardiaque intrinsèque (détection), et pour délivrer des signaux de dépolarisation (stimulation) [6]. La stimulation est déclenchée lorsqu'il y a une différence de potentiel entre les deux électrodes de la/des sondes qui entraîne la dépolarisation des cellules cardiaques. Les améliorations technologiques significatives dans la conception des circuits intégrés ont conduit au développement de dispositifs plus sophistiqués, plus petits, plus fiables et dotés d'une plus grande autonomie. Ces progrès ont considérablement amélioré la qualité de vie les patients souffrant de troubles cardiaques et sont devenus un outil essentiel dans la régulation du rythme cardiaque.

Des études sur les maladies cardiovasculaires ont déjà été entreprises à l'aide de stimulateurs cardiaques chez des mammifères de plus grande taille, tels que des chiens, des chats ou des porcs [8, 9, 10, 11], mais la petite taille des souris et des rats nécessite des adaptations plus conséquentes vis à vis des stimulateurs cardiaques standard. Ainsi, de nouvelles approches ont été développées pour étudier une stimulation efficace chez le petit animal [12, 13, 14, 15]. Cependant, aucune de ces méthodes ne répond au cahier des charges de l'étude de la fréquence cardiaque dans le contexte de l'HTAP, qui exige une stimulation programmable prolongée et très précise d'un groupe de rats en étant le moins invasif possible.

Cette thèse est une étape vers le développement d'un stimulateur cardiaque pour rat, répondant aux exigences physiologiques uniques de l'animal, en commençant par la conception du circuit de stimulation générant l'impulsion qui va être délivrée au cœur. Ainsi, la spécification de la forme d'onde de stimulation est fondamentale. Ce paramètre étant fortement corrélé à la consommation de la batterie, il est impératif de trouver le bon compromis entre efficacité et préservation de l'énergie.

Chapitre 2 : Spécification de l'onde de stimulation

Stimulation proposée

L'impulsion électrique dans les stimulateurs cardiaques est définie par son amplitude (en volts) et sa durée (en millisecondes). L'énergie minimale nécessaire pour stimuler le cœur, appelée seuil de stimulation, peut varier en raison de divers facteurs tels que l'activité physique, les médicaments ou les caractéristiques des électrodes. Le compromis entre amplitude, durée et consommation, qui peut être illustré par la courbe force-durée (Figure 3), doit être considérée pour définir une stimulation efficace, sans danger et énergétiquement optimale [6, 16, 17, 18].

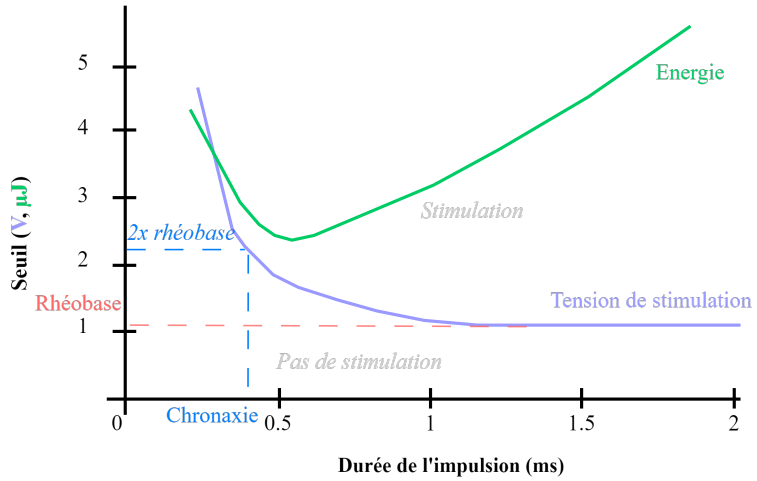

Figure 3: Courbe force-durée

Dans le cadre de cette thèse, nous cherchons à augmenter la fréquence cardiaque du rat jusqu'à des niveaux hyperphysiologiques, ciblant des fréquences cardiaques entre 400 et 600 battements par minute (bpm) (ce qui correspond à des périodes d'impulsion de 100 à 150 ms) contre 240 à 400 bpm pour un rythme normal. Les deux formes d'ondes de stimulation typiques sont monophasique et biphasique, la recherche privilégiant les formes biphasiques car elles sont moins énergivores, permettent de considérer un seuil de tension plus bas et présentent moins de risques vis-à-vis des tissus [19, 20, 21, 22]. La stimulation biphasique comprend deux impulsions : une courte impulsion négative déclenchant la dépolarisation, et une impulsion positive plus tardive pour restaurer l'état de charge neutre des tissus cardiaques [23]. Ces impulsions prennent la forme de décharge dont il existe plusieurs types présentant différents avantages et inconvénients. Les formes d'ondes triangulaires telles que les rampes et les exponentielles sont préférées pour leur efficacité énergétique et leurs effets physiologiques sur le cœur [19, 24]. Tenant compte de ces éléments, et en

se basant sur la stimulation de Lahtinen et al. [25], deux formes d'onde biphasiques, l'une avec une décharge linéaire et l'autre exponentielle, ont été choisies pour la stimulation chez les rats, dans le but de comparer leur efficacité. Elles sont toutes deux présentées sur la Figure 4.

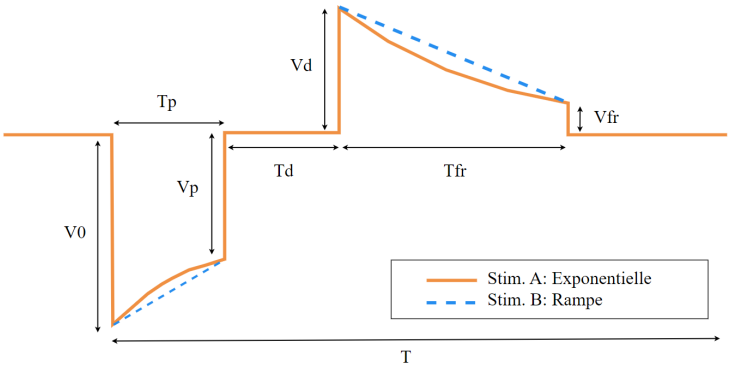

Figure 4: Stimulation proposée avec décharge exponentielle (ligne continue) ou rampe (ligne pointillée)

Validation expérimentale de la stimulation choisie

Après avoir choisi une forme d'onde de stimulation, nous avons procédé à l'évaluation de son efficacité pour une stimulation réelle chez le rat. Pour ce faire, nous avons mené deux expériences in vivo sur des rats provenant de la plateforme AnimEx (Châtenay-Malabry, France)[1].

L'objectif de la première expérience était d'évaluer la validité des stimulations biphasiques sélectionnées en rétablissant une fréquence cardiaque normale de 300 à 400 bpm chez un rat sain, après qu'elle ait été réduite à environ 200 bpm à l'aide d'un composant pharmacologique appelé ivabradine (IVA). Les expériences et leurs résultats ont fait l'objet d'un article de conférence présenté à ICECS 2021 [26].

Pour l'expérience, nous avons utilisé un prototype de générateur d'impulsions programmable que nous avons implémenté sur un FPGA, capable de délivrer une forme d'onde configurable à des fréquences de stimulation fixes de 250, 300 et 400 bpm. Le schéma bloc de ce prototype est illustré Figure 5a. La stimulation biphasique avait une amplitude crête à crête de 8 V, et nous avons incorporé une résistance variable dans notre prototype pour ajuster finement

[1]Toutes les expériences ont été réalisées conformément aux principes directeurs de la Communauté européenne concernant les soins et l'utilisation des animaux (2010/63/UE, 22 septembre 2010), aux directives du comité d'éthique local (CREEA Ile-de-France Sud) et au décret français n° 2013-118 du 1er février 2013 relatif à la protection des animaux utilisés à des fins scientifiques (JORF n° 0032, 7 février 2013, p. 2199, texte n°24). Les autorisations de pratiquer des expérimentations animales conformément à ce décret ont été obtenues auprès du ministère français de l'Agriculture, de l'Agroalimentaire et de la Forêt (accord n°B 92-019-01).

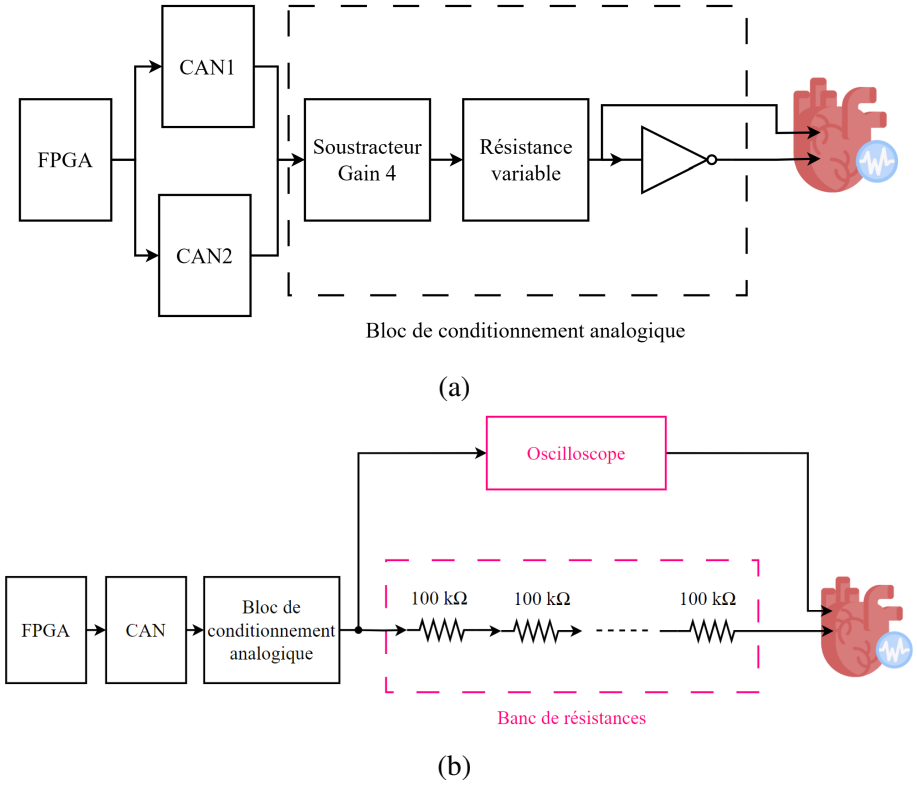

Figure 5: Schéma bloc du prototype utilisé lors des tests *in vivo* chez le rat (a) pour la validation de la stimulation proposée, (b) pour la spécification des ordres de grandeur de courant

cette amplitude et atténuer les dommages potentiels aux tissus. La fréquence et la forme de l'impulsion pouvaient être ajustées dynamiquement pendant la stimulation. Le circuit était alimenté par $\pm$ 5 V et avait une consommation globale d'environ 56,7 mW pour chaque forme d'onde. Nous avons de plus conçu un circuit imprimé (PCB) comprenant les composants nécessaires pour la conversion analogique du signal sortant du FPGA.

L'évolution de la fréquence cardiaque et celle de la pression artérielle ont été mesurées à plusieurs moments: juste après avoir eu accès au cœur, 10 minutes après l'administration d'IVA puis lors la stimulation électrique de l'oreillette droite à l'aide des formes d'onde A et B (1 minute), en alternance avec des périodes de repos sans stimulation (5 minutes). Ainsi, cette expérience a permis de montrer l'efficacité du système pour rétablir une fréquence cardiaque normale chez le rat, et a contribué à la validation de deux formes d'ondes de stimulation, avec une décharge exponentielle ou linéaire (sans disparité significative remarquée quant à leur efficacité), et d'une architecture système flexible qui permet d'ajuster en temps réel les paramètres de cette stimulation

tels que la fréquence, l'amplitude et la forme de la décharge.

La deuxième expérience a été menée afin de déterminer une plage de courant acceptable qui garantit une stimulation du cœur stable et efficace tout en étant suffisamment faible pour préserver l'intégrité des cellules cardiaques. Durant cette expérience, une version modifiée du prototype utilisé précédemment a été employée. Son schéma bloc est illustré Figure 5b. Ces expériences ont abouti à deux conclusions principales. Tout d'abord, un courant minimum de 30 µA est nécessaire pour stimuler efficacement le cœur du rongeur lors de l'utilisation de la forme d'onde biphasique sélectionnée. Ensuite, en se basant sur cette valeur de courant, nous avons estimé que la charge du stimulateur cardiaque peut être modélisée avec une résistance équivalente de 133 kΩ à notre site de stimulation, ce qui correspond aux modèles utilisés dans l'étude de [27].

Chapitre 3 : Conception du circuit de stimulation intégré

Dans le cadre de cette thèse, nous nous concentrons sur la conception du circuit intégré de la partie fondamentale d'un pacemaker : la stimulation. Le circuit a été réalisé en 0,18 µm, dans la technologie XFAB XH018 et les simulations ont été effectuées grâce à Cadence.

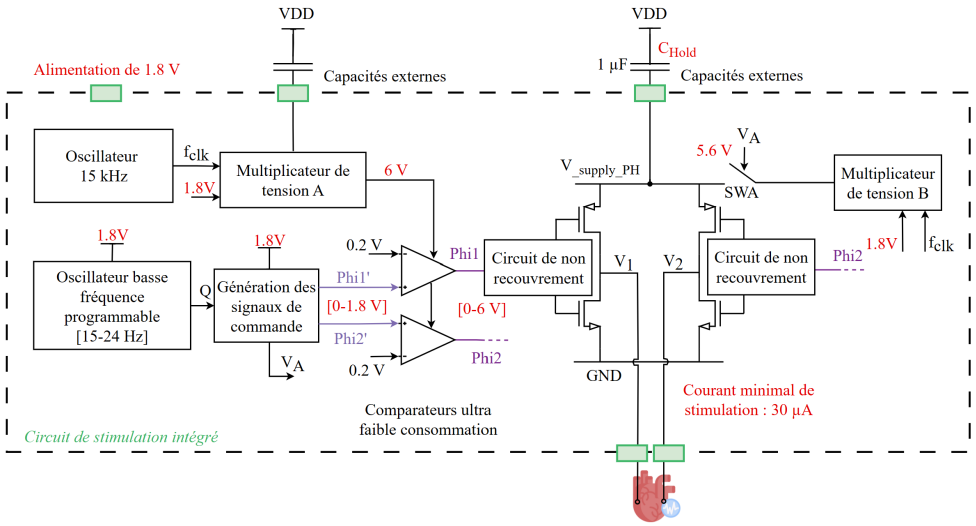

Figure 6: Schéma bloc du circuit de stimulation

Notre revue de la littérature, ainsi que nos expériences in vivo sur les rats validant et spécifiant la forme d'onde, nous ont amené à proposer l'architecture présentée Figure 6. Elle repose sur un pont en H, permettant d'obtenir un signal de forme biphasique, grâce à un jeu de commandes adapté orchestrant

la charge ou décharge d'une capacité et gouvernant la polarité de la tension appliquée au cœur. Les signaux de commande pour le pont en H, ainsi que sa tension d'alimentation et la stimulation sont représentés Figure 7.

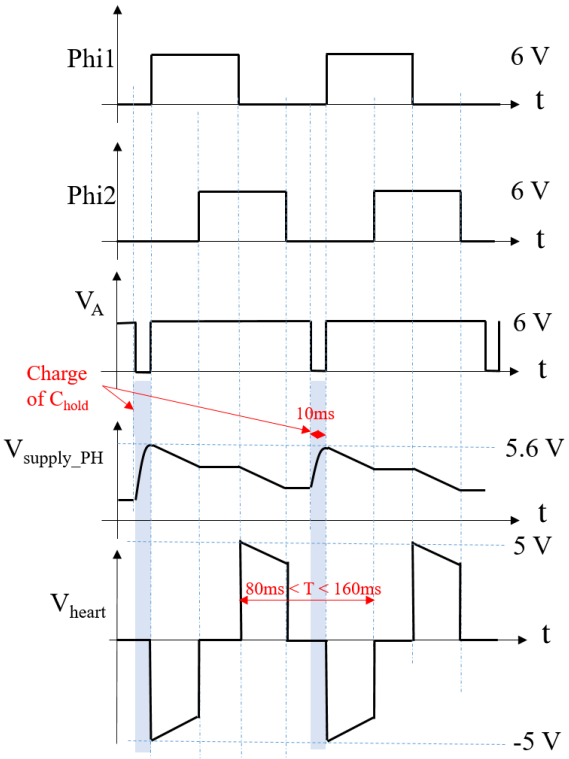

Figure 7: Signaux du circuit de stimulation

Afin d'obtenir une amplitude de stimulation suffisante, cette capacité, externe, a une valeur de 1 µF et une tension de 5,6 V provenant d'un multiplicateur de tension alimente le pont en H. En effet, nous avons vu dans le chapitre précédent qu'un courant minimal de 30 µA est nécessaire pour une stimulation efficace, et en considérant la charge du pacemaker modélisé par une résistance de 133 kΩ, la tension d'alimentation du circuit de 1,8 V n'est pas suffisante pour répondre à ce besoin. Le circuit comporte donc deux multiplicateurs de tension, pilotés par un oscillateur dans le domaine du kHz. Le premier (multiplicateur B), reposant sur un multiplicateur capacitif, sert à l'alimentation du pont en H et doit ainsi avoir un temps de réponse assez court pour recharger le condensateur à chaque répétition de la stimulation. Le second, appelé multiplicateur A, s'appuie sur l'architecture du multiplicateur Dickson pour générer une tension continue de 6 V pour les commandes du pont en H. Ces commandes sont obtenues à partir d'un oscillateur à relaxation (ROSC) programmable dans la gamme de la dizaine de Hz suivi d'un circuit de mis en forme. Elles sont ensuite remodelées de [0-1,8] V à [0-6] V à l'aide d'un comparateur à très faible consommation alimenté par le dit multiplicateur.

La fréquence d'oscillation du ROSC dépend de la capacité totale équivalente d'un banc de condensateurs programmable ainsi que du courant fourni par des sources qui permettent de charger et décharger cette capacité. Cela permet de générer des oscillations à des fréquences variables allant de 15,3 à 23,8 Hz, soit deux fois supérieures à celles ciblées pour le rat.

Dans le but de minimiser la consommation totale du circuit, cet oscillateur à relaxation a été conçu suite à une étude de l'état de l'art des techniques ultra-faible consommation (e.g., Stacking, Reverse Body Biasing, Dynamic Leakage Suppression Logic - DLS), qui a conduit à la conception ad hoc de portes logiques de type DLS. Cette technique récente, réservée à des opérations basse fréquence (<100 Hz), consiste en l'ajout, à une porte logique standard, d'un NMOS relié à Vdd et d'un PMOS relié à GND, et dont les grilles bouclent sur la sortie, ce qui permet de placer les transistors dans un état de 'super-cut-off', et donc de réduire drastiquement les fuites de courant. Les simulations pire cas effectuées en utilisant des sources de courant et de tension idéales ont montré la robustesse des différents blocs du circuit vis à vis des variations PVT à la fréquence d'opération visée.

Chapitre 4 : Résultats et discussion

La Figure 4.1 présente les signaux de stimulation biphasiques ainsi que la forme d'onde de courant correspondante générés par le circuit proposé. Bien que seules les formes d'ondes de fréquences les plus basses (6,8 Hz) et les plus élevées (10,1 Hz) soient représentées par soucis de clarté, il est important de noter que ces formes d'onde peuvent être obtenues à différentes fréquences en fonction de la combinaison de condensateurs dans l'oscillateur à relaxation comme présenté dans la Table 1. L'amplitude crête à crête de la stimulation est de 9 V, allant de -5 V à 4 V. En outre, le courant de chaque forme d'onde dépasse 30 µA, ce qui correspond au seuil requis pour une stimulation efficace comme établi lors des tests in vivo.

L'ensemble du circuit de stimulation consomme 112 µW dont 100 µW est directement consommé par le pont en H pour la stimulation du cœur, qui a besoin de deux impulsions d'au moins 30 µA par période d'onde, comme établi grâce aux tests in vivo. Le bloc du circuit comprenant l'oscillateur de fréquence 15 kHz avec ses remises en forme et le multiplicateur A consomme 9.9 µW. Enfin, grâce à l'approche ultra-faible consommation adoptée dans cette conception, l'oscillateur à relaxation dans le domaine de la dizaine de hertz et la synthèse de commande pour le pont en H ne consomment que 1,8 µW soit 1,6 % de la consommation totale du circuit de stimulation.

Nous avons comparé le circuit de stimulation proposé aux circuits intégrés existants dans la littérature. La Table 2 résume les points clés de cette comparaison.

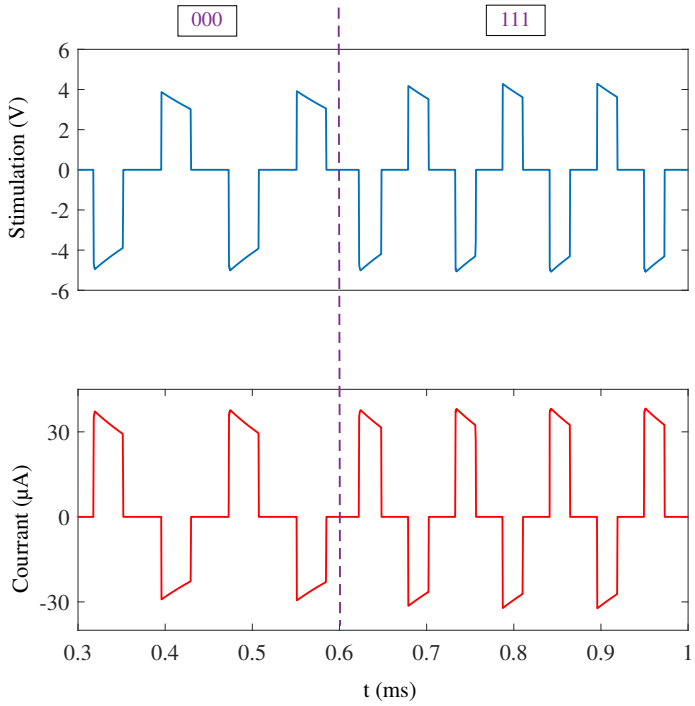

Figure 8: Amplitude de la stimulation et courant correspondant à 6,8 et 10,1 Hz

Combinaison	Capacité (pF)	Fréquence (Hz)	Fréquence (bpm)
000	3,8	6,8	408
001	4,13	7,1	432
010	4,46	7,6	456
011	4,79	8	480
100	5,12	8,4	504
101	5,45	8,9	534
110	5,78	9,5	570
111	6,11	10,1	606

Table 1: Fréquence de la stimulation proposée en fonction de la valeur du condensateur

Dans l'ensemble, le circuit décrit dans cette thèse se distingue par rapport à la littérature actuelle grâce à la combinaison de deux caractéristiques : il est capable de fournir la tension d'impulsion la plus élevée et une large gamme de fréquences adaptées à notre application, tout en conservant une consommation d'énergie relativement faible. Il est donc très bien adapté pour répondre aux besoins spécifiques de l'étude de l'HTAP sur un modèle de rat. En effet, le fait de disposer de larges gammes de tension et de fréquence permet d'explorer de manière plus complète l'impact de la fréquence cardiaque dans l'HTAP, et une très faible consommation d'énergie permettra de mener des expériences sur le long terme avec une petite batterie adaptée à la taille de l'animal.

Conclusion et Perspectives

Le circuit proposé génère une impulsion biphasique, à des fréquences comprises entre 6,8 et 10,1 Hz, soit 400 et 600 bpm, répondant au cahier des charges pour une stimulation chez le rat dans le cadre de l'étude de l'HTAP. Ce travail constitue une première étape vers une importante série d'études de recherche réparties sur de multiples domaines, et un travail plus approfondi reste évidemment essentiel pour mettre au point un appareil entièrement adapté au petit animal.

Une première piste d'amélioration concerne la conception des sources de tension et de courant utilisées dans le circuit. En effet, comme évoqué dans le Chapitre 3, les sources utilisées pour les références de tension sont encore idéales. Il est donc nécessaire de concevoir le circuit pour établir les références appropriées. De plus, la valeur de courant des sources contenues dans le ROSC, influence fortement la fréquence et le rapport cyclique des oscillations. Une étude approfondie mérite donc d'être entreprise pour améliorer les sources de courants réalisées pour le circuit étant donné l'aspect critique de ces sources sur le fonctionnement de l'oscillateur.

Bien que nous ayons réalisé le layout et la simulation post-layout de certains blocs, notamment les composants DLS, il nous reste encore à entreprendre le layout de l'ensemble du circuit et effectuer son analyse post-layout. Ces simulations, prenant en compte les capacités parasites, sont essentielles pour obtenir une représentation plus précise du comportement et des performances du circuit. De plus, elles offriront des informations sur la surface totale occupée par le circuit.

L'étude étant limitée à des tests aigus, il n'a pas été possible d'évaluer les effets à long terme de la stimulation proposée. Des expériences plus longues sont d'ores et déjà envisagées à l'aide du prototype FPGA susmentionné, en attendant une première version du circuit intégré de stimulation. D'un point de vue médical, ces tests permettront de tirer des premières conclusions sur l'influence de la fréquence cardiaque sur un modèle d'HTAP chez le rat. D'un point de vue électronique, ils permettront de tester et d'améliorer les caractéristiques du circuit (et d'en envisager de nouvelles). La bibliothèque de portes logiques DLS à très faible consommation développée dans le cadre de cette thèse ouvre déjà la voie à l'implémentation d'algorithmes numériques complémentaires pour le stimulateur cardiaque. Par exemple, cela pourrait inclure la détection de la fréquence cardiaque sur un ECG intégré pour vérifier que le cœur du rat bat à la fréquence attendue. Une adaptation de l'amplitude de stimulation pourrait également être envisagée. L'ajustement de l'intensité de la stimulation en fonction des changements physiologiques en temps réel dans le corps permettrait de garantir l'efficacité de la stimulation pour chaque individu tout en s'assurant qu'elle ne comporte aucun risque pour les tissus cardiaques,

en évitant la sur- ou la sous-stimulation. L'utilisation de ce petit dispositif de stimulation pourrait être étendue, non seulement à d'autres animaux de laboratoire, mais aussi à des animaux domestiques. Dans une autre mesure, un dispositif de cette taille pourrait offrir des perspectives pour répondre aux besoins des nouveau-nés, qui rencontrent encore des défis importants pour trouver des dispositifs adaptés.

	JSSC04 [28]	TBioCas11 [29]	Nature2017 [30]	Nature2019 [14]	TBioCas19 [31]	AICSP19 [32]	TBME22 [33]	Circuit proposé
Technologie	0,5 µm	0,35 µm	-	-	0,18 µm	0,18 µm	0,18 µm HV	0,18 µm
Type de stimulation	Tension	Tension	Tension	Tension + Optique	Tension	Tension	Tension/Courant	Tension
Amplitude max.	7,5 V	3,2 V	2 V	2,2 V	3,6 V	3 V	5,5 V	9 Vpp
Fréquence de stim.	-	0,5 - 31,25 Hz	1 Hz	5 - 10 Hz	-	100 Hz -100 kHz	1 Hz	6,8-10,1 Hz
Durée de la stim.	0,5 ms	0,63 - 1,94 ms	1 ms	250 ms	0,3 ms	-	0,2- 1 ms	25-35 ms
Consommation totale	8 µW	48 µW	1 mW	6 mW	1 W	-	1 mW	111,7 µW
Composants externes	Sondes + Cap.	Sonde + Spire + Batteries + Cap.	-	Sonde + µLED + Antenne	Spire + LED + Cap.	Crystal	Spire + LED + Résistance + Cap.	Cap.

Table 2: Comparatif des performances

General introduction

This Ph.D. thesis arises from a collaboration between CentraleSupelec and two INSERM (French National Institute of Health and Medical Research) research units: U999, which specializes in the study of mechanisms responsible for pulmonary arterial hypertension (PAH) and therapeutic innovation, and U1180, specialized in cardiovascular signaling and physiology, with an interest in fundamental mechanisms that regulate heart rate.

Given that cardiovascular conditions are the leading cause of death worldwide and there exists a positive correlation between heart rate values and total mortality, exploring the modulation of the heart rate holds significant promise as a therapeutic intervention.

As such, the medical community aims to investigate, through animal research, the impact of heart rate modulation in cardiopulmonary physiology and pathophysiology, specifically in the context of pulmonary arterial hypertension.

PAH is a rare, progressive heart condition characterized by abnormally high blood pressure in the pulmonary arteries, which can ultimately lead to right heart failure. Early-stage symptoms often include fatigue, difficulty breathing, and syncopal episodes. As the condition progresses, heavier symptoms such as hoarseness, swelling of the face and legs (indicative of right heart failure), or bluish skin discoloration of the extremities may manifest. While the cause of PAH is most often unknown, hereditary genes, HIV infections or the use of certain drugs increase the risk. To date, there is no cure and, only palliative treatments in the form of medication or transplantation aim to improve the patient's quality of life.

In heart-related disorders, the cardiac frequency plays a critical role, and its exploration holds great potential for uncovering new therapeutic approaches. To our current knowledge, existing pharmacological compounds do not allow for the exclusive increase of cardiac frequency without affecting other cardiac parameters such as contractility and blood pressure. Therefore, we decided to take on an electrical approach with the design of a cardiac stimulator. As much of the research on cardiovascular diseases relies heavily on animal models, particularly rats, our goal is to develop a controllable cardiac pacemaker implantable in small animals to modulate their heart rate. The device must be adapted to the animals, in terms of size, but also regarding the waveform's

amplitude and frequency, which are directly related to rat physiology.

Currently, there is no commercially available pacemaker tailored for small animals, such as rats, mice or other small mammals compatible with chronic (i.e. long-term) implementation. However, its development has noteworthy implications and potential benefits in cardiac physiopathology research. Such device application comes with stringent constraints, notably with regard to the reduced dimension and ultra-low power features linked to the necessity of its implantability.

Hence, the main objective of this thesis is to progress towards the conception of an integrated pacemaker circuit, starting with the design of the pulse generator.

Chapter 1 begins by presenting an overview of the heart, offering essential background information and technical details on pacemakers. In Chapter 2, we delve into the specification of the pacing waveform and explore the orders of magnitude for efficient stimulation. Chapter 3 centers on the design of the integrated stimulation circuit, detailing the individual performances of the different blocks composing our pulse generator, while Chapter 4 describes the intricate block that allows to obtain high voltage levels from a 1.8 V supply before presenting the global simulation results of the entire circuit, offering a review of its performances and comparing it with the literature. The concluding chapter, Chapter 5, synthesizes the findings and suggests potential avenues for future exploration.

Chapter 1

The Heart and Cardiac Pacemakers

1.1 Introduction

This chapter aims to provide an overview of the cardiac system for a better understanding of the need and application of artificial cardiac pacemakers in patients suffering from heart-related conditions. We begin with a simple explanation of what the heart is, what it is supposed to do, and how it works. We then briefly discuss pulmonary arterial hypertension, a rare cardiovascular disease in which we want to explore the role of cardiac frequency. The last section of this chapter elaborates on the principle of pacemakers, introducing both transvenous and more recent leadless devices before reviewing the literature on systems used in and/or aimed at animals.

1.2 Understanding the heart

1.2.1 The cardiac system

The blood circulatory system

The heart is a four-chambered organ that pumps blood throughout the body. For this purpose, it is laterally separated into two sides (right/left) by a thin muscular wall called the septum. Each side is composed of a "receiving" upper chamber, called the atrium (pl. atria), and a "pumping" lower chamber, called the ventricle. Heart valves at the exit of each chamber prevent the backflow of blood, as pictured in Figure 1.1a.

The organ is at the center of what we call the circulatory system. In mammals, this system is composed of two circulations in series: systemic circulation and pulmonary circulation (Figure 1.1b).

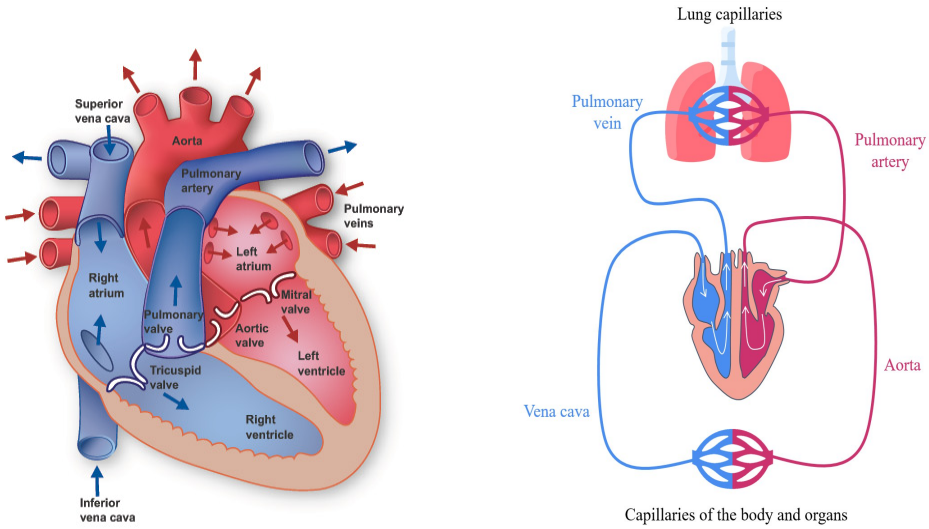

(a) (b)

Figure 1.1: (a) Blood circulatory system of the heart (figure issued from [34]), (b) Double circulation

Systemic circulation corresponds to a pump, namely the left heart, where the left atrium receives oxygenated and decarboxylated blood from the pulmonary veins. The blood then flows into the left ventricle, which ejects it from the heart through the aorta. Systemic blood flow and pressure are generated in the aorta. The aorta and the downstream arteries provide oxygen and nutrients to the rest of the body. Ensuingly, the blood from the upper and lower body, called systemic venous flow, which is now poor in oxygen and rich in carbon dioxide, is delivered through the superior and inferior vena cava to the start of the pulmonary circulation: the right atrium.
The pulmonary circulation has a pump, namely the right heart, that admits the oxygen-depleted and hypercarboxylated systemic venous blood flow in the right atrium. The right ventricle expels the venous blood flow to the lungs through the pulmonary arteries, where the pulmonary arterial blood flow and pressure are generated. In the lungs, the pulmonary artery blood flow is replenished with oxygen and impoverished in carbon dioxide before returning through the pulmonary veins to the left atrium, where the systemic circulation starts. Since the pulmonary arterial resistances (pressure over cardiac output ratio) are 6 times lower than the systemic resistances, the pulmonary artery pressure is 6 times lower than the systemic arterial pressure. This circulation repeats every time the heart beats and corresponds to continuous synchronized cycles of contraction phases (systole), where the blood is ejected from the ventricles, and relaxation phases (diastole), where they are filled with blood. In humans, the heart pumps around 5 liters of blood each minute at rest (a volume that can increase four to seven times during intense activity [35]), and

beats approximately 100 000 times a day, that is to say, more than 3.5 billion times in a lifetime [34]. The volume of blood pumped by the heart, known as cardiac output (CO), is equal for both systemic and pulmonary circulations. As shown in equation 1.1, it can be calculated as the product of the heart rate (HR), i.e., the number of heartbeats per minute (bpm), by the volume of blood ejected from one ventricle (right or left) at every contraction, called stroke volume (SV). The CO is measured in liters per minute.

$$CO[L/min] = HR[/min] \cdot SV[L] \tag{1.1}$$

The electrical activity

The pumping function of the heart is controlled by the heart's electrical conduction system (Figure 1.2), which helps the muscle to contract in a synchronized fashion. The atrium contraction is triggered by the spontaneous depolarization of special cardiac cells, known as pacemaker cells, clustered in the sinoatrial (SA) node, a small node in the right atrium. The term depolarization refers to the electrical potential of a cell shifting to a negative state before reverting to its resting potential. About 60 to 80 times a minute, the SA node initiates an electrical impulse that spreads throughout both atria to stimulate them, expulsing the blood to the ventricles. The impulse then travels to the atrioventricular (AV) node, where it is slowed down before reaching both ventricles through the two branches of the His-Purkinje network. This induces ventricular contractions and blood ejection from the ventricles into the pulmonary and systemic circulations.

Cardiac electrical activity can be recorded in the form of an electrocardiogram (ECG) [35, 37]. Electrodes placed on the chest, wrists and legs, detect the electrical signals generated by the heart cells. Each cardiac event derived from the propagation of the electrical activity is represented by a wave or segment, labeled by the letters P to U, resulting in the waveform pictured in Figure 1.3.

- P wave represents the atrial depolarization and contraction.
- PR interval is the time needed for the electric signal to travel from the SA node to the AV node.
- QRS complex corresponds to ventricular depolarization and contraction, which marks the firing of the AV node. (Meanwhile, the atria are repolarizing but the signal is buried in the QRS complex).
- ST segment is a plateau phase between the end of the ventricular depolarization and the beginning of ventricular repolarization. It corresponds to the period where the ventricles are contracting and pumping blood.

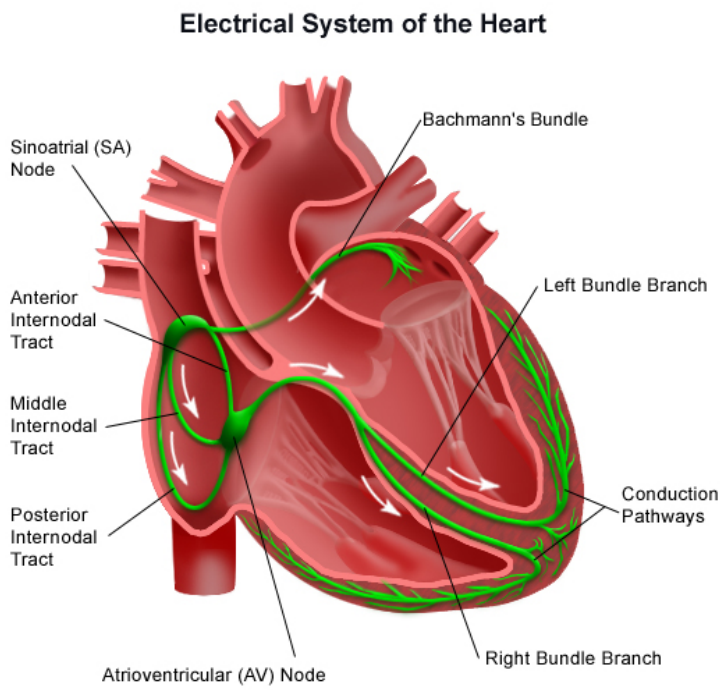

Figure 1.2: The heart's electrical conduction system (figure issued from [36])

- QT interval indicates the time taken for ventricular depolarization and repolarization. Its duration varies with cardiac frequency (shorter when the frequency increases and vice versa).

- T wave depicts the end of ventricular repolarization (relaxation)

- In some individuals a wave of small amplitude and low frequency, called the "U wave", can be observed following the T wave but its origin remains unclear.

As these waves directly reflect physiological events, their morphology and duration give crucial information on a patient's condition. ECGs are particularly used in the detection of arrhythmias [35], which regroup a variety of conditions marked by irregular heart rhythms caused by abnormalities in the electrical impulses of the heart muscle. The most common is fibrillation, where the heart rate is irregular and chaotic, causing the random and rapid twitching of the atria. One way to determine the type of arrhythmia is by measuring the HR, also called cardiac frequency (CF), by counting the number of QRS in a minute. At rest, a standard HR ranges from 60 to 100 beats per minute (bpm) in adults. However, it may be influenced by a multitude of factors including age, exercise, emotions and some medications.

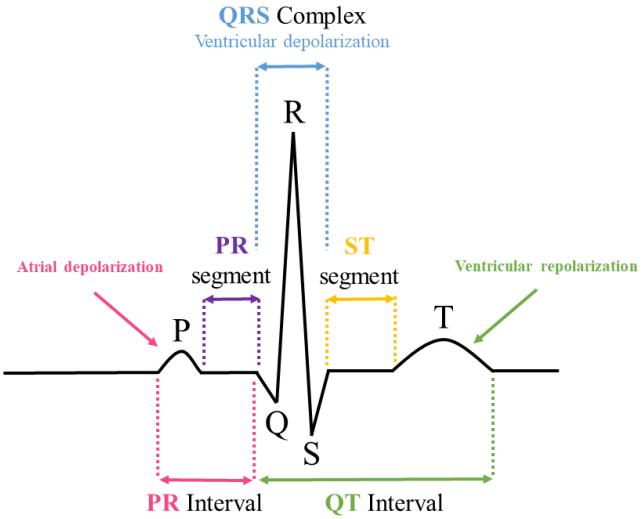

Figure 1.3: Characteristic points of an ECG

1.2.2 Heart conditions

According to the World Health Organisation (WHO) [38], cardiovascular diseases (CVD) are the leading cause of death worldwide, accounting for nearly one-third of all death each year, with more than 17 million in 2019. They regroup a multitude of disorders affecting the heart and its function, such as heart attacks, coronary artery disease or stroke. In this section, our attention is directed towards pulmonary arterial hypertension, a rare condition that serves as the primary focus of our study.

Pulmonary arterial hypertension

Pulmonary arterial hypertension (PAH) is a severe chronic cardiovascular condition characterized by abnormally high blood pressure in the pulmonary arteries. It has an estimated prevalence of around 15-50 cases per million individuals worldwide and is most commonly found in women aged between 30 and 60 [1]. PAH is a progressive disorder that causes the walls of the pulmonary arteries to thicken and stiffen, making it harder for blood to flow through them (Figure 1.4). This results in an increased mean pulmonary arterial pressure (mPAP), i.e., the pressure measured before the blood arrives at the lungs, and pulmonary vascular resistance (PVR), putting a strain on the right side of the heart as it has to put more effort into pumping blood through the lungs. Quantitatively, as reported by the 6th World Symposium on Pulmonary Hypertension (WSPH) [39], the disease is defined by an mPAP exceeding 20 mmHg, a pulmonary wedge pressure (PWP) less than or equal to 15 mmHg, and a PVR greater than 3 WU at rest [40, 41]. In opposition, a healthy

patient's typical values range between 12-16 mmHg, 6-12 mmHg, and less than 2 WU, respectively. Early symptoms generally come in the form of persistent fatigue and shortness of breath during heavy or everyday exercises, depending on the severity of the disease (running or carrying heavy loads at first, climbing stairs, or even walking in more advanced stages). Chest pain, palpitations, and fainting episodes are also frequent. As the disease progresses, individuals may experience swelling of the face, legs, and abdomen and even abnormal bluish skin discoloration due to low blood oxygen levels. Eventually, if left untreated or in more advanced stages, PAH can lead to right heart failure [42].

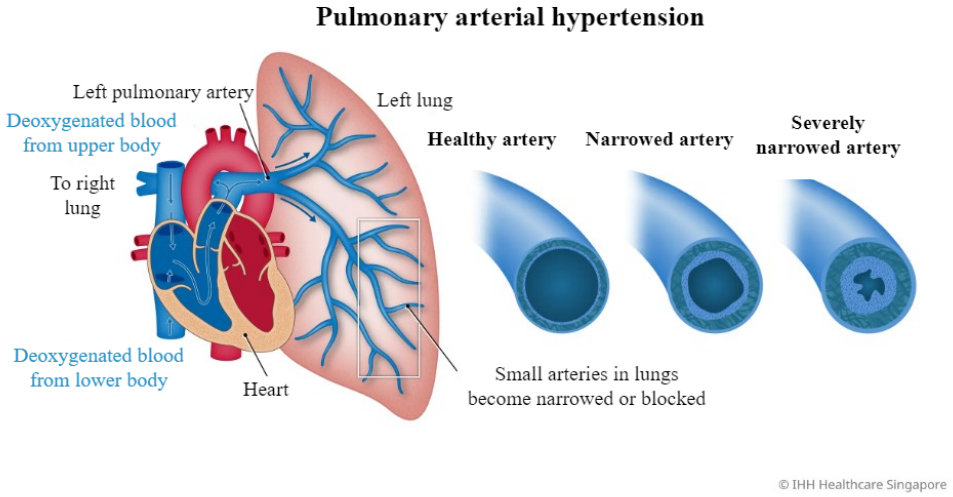

Figure 1.4: Pulmonary arterial hypertension (figure issued from [2])

Due to its nonspecific and mild symptoms similar to many other heart or lung conditions, PAH is often underdiagnosed or misdiagnosed as it is determined by ruling out all other causes. This results in an average delay of 2 to 3 years before the correct diagnosis, while the disease has progressed to a more advanced stage [43]. While predominantly idiopathic (of unknown cause), genetic predispositions, connective tissue diseases such as scleroderma or lupus, HIV infection, or certain drugs like diet pills or methamphetamines can be associated with PAH [42, 44]. Although there is no cure, medical care and palliative treatment can help reduce symptoms and improve the patient's quality of life as the pathology progresses. Presently, available treatment options primarily offer palliative relief, and ongoing research is concentrated on exploring potential therapeutic interventions [3, 4, 5]. The conventional approach is by preventive measures (limitation of physical efforts, contraindication to stays at high altitude locations, contraindication against pregnancy) in addition to medication (vasodilators, diuretics, and anticoagulants, depending on the symptoms) and possibly oxygen therapy. A lung or heart-lung transplant may be required

in the most severe cases. Under conventional treatment alone, the prognosis for the idiopathic form of PAH stayed poor, with a median survival of 2.8 years from the time of diagnosis [45, 43]. However, recent advancements in the disease therapy and management, allowed to push the post diagnosis survival rate back to an estimated 7-year median according to the REVEAL registry records [46, 47].

In this type of heart-related disease, the cardiac frequency plays a significant role as the cardiac output, i.e., the blood pumped by the heart, depends on this cardiac frequency, and is used in the calculation of the total pulmonary resistance (TPR).

$$TPR = \frac{mPAP}{CO} \tag{1.2}$$

Drawing from equations 1.1 and 1.2, it is reasonable to posit that lowering the heart rate has the potential to slow down the increase of the pulmonary resistance. This hypothesis forms the basis for exploring the potential influence of heart rate modulation on the pathophysiology of PAH, opening the path to a novel research axis for curative treatment. To our current knowledge, existing pharmacological compounds do not allow for the exclusive increase of cardiac frequency without affecting other cardiac parameters such as contractility and blood pressure. With this in mind, we decided to take on an electrical approach with the design of a controllable cardiac pacemaker implantable in small animals.

1.2.3 The use of rat models in medical research

As previously mentioned, major progress in the treatment of PAH has led to improved life expectancy for patients. However, this improvement stays modest, highlighting the ongoing need for research in pursuit of new therapeutic solutions. In cardiovascular research, studies on animal models contributes to invaluable insight into the disease pathophysiology and the investigation of potential treatment strategies. While no animal model is ideal, rats are particularly valuable in studying conditions like PAH, owing to some physiological and anatomical resemblance to humans, including the four heart chambers [48, 49]. For instance, similar values can be observed in cardiopulmonary parameters. In anaesthetized rats, a mean aortic pressure ranges from 71 to 93 mmHg, and the right atrial pressure is approximately 2 to 8 mmHg. This is comparable to the measured values in humans with 70 to 90 mmHg and 2 to 7 mmHg respectively [50].

In addition, their relatively low cost, ease of handling, and short reproductive cycles render rats a practical and cost-effective choice for conducting controlled experiments and longitudinal studies in the context of studies like PAH [51, 52, 53, 54, 55]. Indeed, rats have a relatively short lifespan (∼2.5

to 3.5 years). Hence, we can easily "accelerate" the disease mechanism and recapitulate characteristic features seen in humans, giving the opportunity to study the effects of cardiac frequency in cardiovascular conditions throughout a life cycle and testing the effectiveness and safety of new drugs or treatments. Moreover, their fast and large reproduction provides real statistical value, making them worthwhile assets for research. However, one must keep in mind that being small rodents, rats cardiac frequency is faster than humans', with their heart beating at an average rate comprised between 240 and 400 bpm, that can be increased to 550 bpm during exercise [56, 57]. This major difference is to be taken into consideration for the design of our pacemaker.

Animal research is an important aspect of scientific discovery, but we need to ensure that animals are treated ethically and that their use is justified. To this end, researchers must follow the 3Rs principle, which was first introduced in 1959 by Russell and Burch [58]. The 3Rs stand for:

- Replacement, as in using non-animal models when alternative methods like cell cultures or computer models are applicable.
- Reduction, which involves minimizing the number of animals used in experiments by carefully designing studies and using data from previous research.
- Refinement, referring to optimizing the trial conditions so as to cause as little harm as possible to the test animals, by improving housing, handling and surgical procedures.

By respecting these principles, scientific research can be conducted humanely and rigorously while minimizing the use of animal models.

1.3 Artificial cardiac pacemakers

The introduction of artificial pacemakers has dramatically impacted the treatment of various heart conditions that cause irregular or slow heartbeats. With more than 1 million implantations worldwide per year as of 2011 [59], a number bound to keep increasing, they remain the only known effective long-term therapy to this day. Artificial cardiac pacemakers are small battery-powered implantable devices developed to deliver controlled electrical impulses, similar to those naturally generated by the SA node, into the heart muscle to ensure regular and effective heart activity. Over the years, significant technological improvements in integrated circuit design have led to the development of more sophisticated devices that are smaller, more reliable, and have increased battery autonomy. In half a century, the device weight went from 113 g [60] to 20 g for traditional pacemakers and down to 1.75 g for their more recent leadless

counterparts [61], notably thanks to the development of high energy density batteries as stated by [62]. Features such as rate responsiveness, multisite pacing or MRI compatibility, to cite a few, have further contributed to the enhancement of these devices. These advancements have greatly improved the outcomes for patients with heart conditions and have become an essential tool in the management and treatment of various heart conditions.

1.3.1 Conventional pacemakers

Conventional or transvenous pacemakers (CPM) consist of two main components: a pulse generator and one to three leads (Figure 1.5a). The pulse generator, also referred to as «can», is a small hermetically sealed case (∼20 cm^3) typically made of biocompatible materials like titanium alloy, housing the electronic circuitry, including the one that generates the electrical impulses, and a battery. The battery, generally composed of lithium-iodine, takes up a significant portion of the device's size and weight, and has an average longevity of 10 to 15 years following the patient's requirements. A few months prior to the anticipated depletion of the battery, a surgical procedure akin to the initial implantation is performed to replace the whole device. The leads are thin flexible wires insulated by biocompatible material (generally silicone or polyurethane) that connect the can to the cardiac tissues either to monitor intrinsic cardiac activity (sense) or deliver depolarizing signals (pace) through their tip electrodes [6].

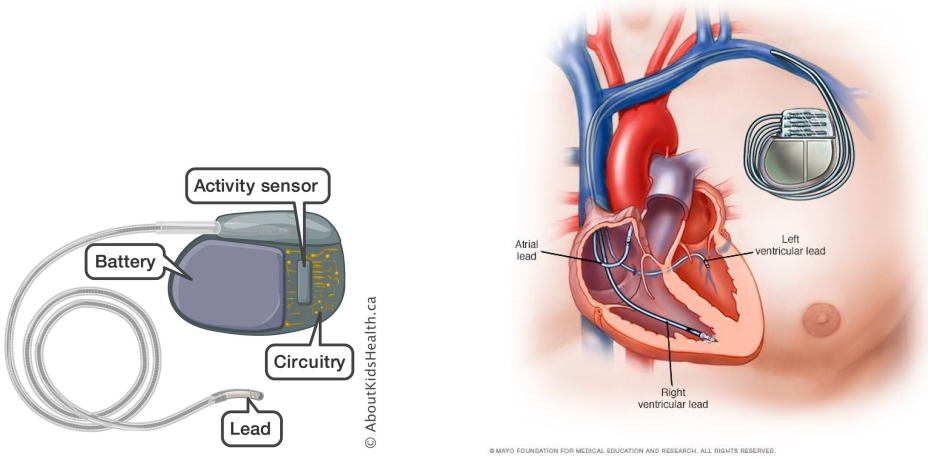

(a) (b)

Figure 1.5: (a) Block diagram (figure issued from[7]), (b) Implantation site of a triple chamber pacemaker (figure issued from [63])

As illustrated in Figure 1.5b, the pacemaker is generally implanted subcutaneously through minor surgery in a muscle pocket created beneath the

collar bone, while the leads are threaded into the relevant chamber(s) of the heart through a large vein, thus the appellation transvenous pacemaker. The electrodes are then either screwed in or tined into the heart muscle.

Stimulation is initiated when there is a potential difference between the two electrodes. Pacemaker leads are either unipolar or bipolar as presented in Figure 1.6. In unipolar pacing, the cathode, i.e., the electrode serving as the negative pole for delivering the pacing pulse, is at the tip of the lead. Meanwhile, the pacemaker can acts as the anode, or positive pole. In contrast, bipolar systems have both the anode and cathode located on the same pacing lead, with electrons flowing from the proximal ring (anode) to the lead tip (cathode) [16, 64, 65]. As the anode-cathode distance is longer in unipolar leads, the energy required to depolarize the myocardium is higher. This often results in large pacing artifacts on the ECG due to the excitation of body tissues around the pacemaker. On the other hand, bipolar leads have both the anode and cathode within the heart, minimizing the risk of these artifacts and making them less susceptible to oversensing noncardiac signals such as electromagnetic interference (EMI) or skeletal muscle activity. Thanks to the enhancements that have resulted in more robust and safer designs, bipolar leads have become standard and the use of unipolar pacing is no longer prevalent [66, 62].

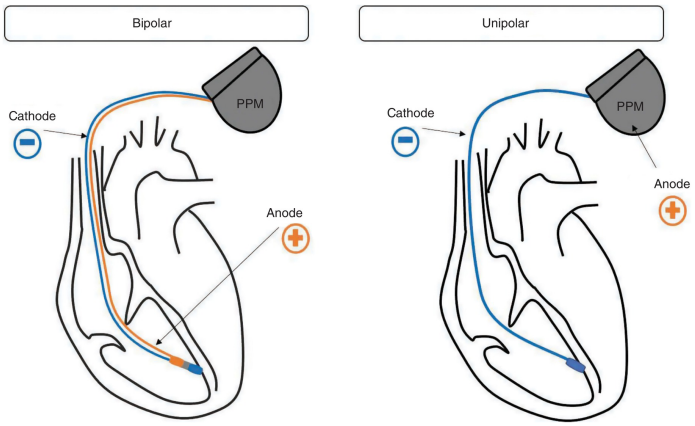

Figure 1.6: Bipolar VS unipolar leads (figure issued from [67])

The complexity in cardiac stimulator systems has evolved enormously since the first fully self-contained pacemaker implantation. The device, implanted in October 1958 by Dr. Ake Senning, was developed by Rune Elmqvist and operated for only 3 hours. Another identical device was implanted the following day, and an additional 26 pacemaker replacements were required over 43 years. Despite the mitigated success, this marked a milestone in the history of cardiac pacing. In 1960, after two years of preclinical trials, Wilson Greatbach's pacemaker device was successfully implanted by Dr. William Chardack in a elderly patient suffering from complete AV block. This achievement extended

the patient's life by another year and a half. Greatbach's cardiac stimulator [60], was limited to ventricular pacing and utilized a blocking oscillator to generate a square, narrow pacing pulse, followed by an amplifier for a greater output. The schematic is represented in Figure 1.7.

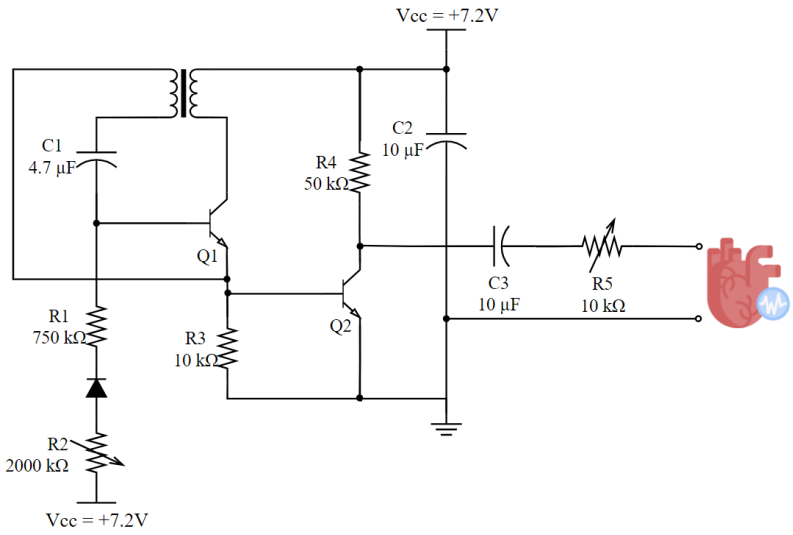

Figure 1.7: Schematic of the first implantable pacemaker by [60]

The stimulation was induced at a fixed rate of 60 bpm, preset before the implantation, without consideration for the intrinsic heart activity. This could potentially lead to ventricular fibrillation or arrhythmia, as the heart was confused about whether it should follow its inherent pulse or the one delivered by the pacing system. To address the issue, sensing amplifier circuits were integrated to amplify and normalize intrinsic depolarization signals (P wave or QRS complex) and filter unwanted signals such as repolarization signals (T wave) or far-field signals (generated by the body tissues the electrode is not connected to and EMI) [68, 65]. This incites the system to trigger a response only to a sensed electrical signal or, more precisely, to the absence of it, marking the beginning of what we call demand pacemakers [69], which has become the basis of all modern pacemakers. As the stimulus occurs only when needed, the battery is better preserved.

In contemporary pacemaker designs, most devices are equipped with additional built-in sensors that measure characteristic physiological parameters, including oxygen demand, body movement or contractility [62, 70, 65, 71]. This feature allows the pacemaker to offer a rate-adaptive stimulation that helps the heart adjust its rate to meet the body's demand, which fluctuates throughout the day according to our level of physical activity. Here again, the battery management is optimized as the stimulation is adapted to the patient's needs. Figure 1.8 depicts a block diagram of a rate-responsive pacemaker, also referred to as synchronous pacemakers, in opposition to their fixed-rate (or

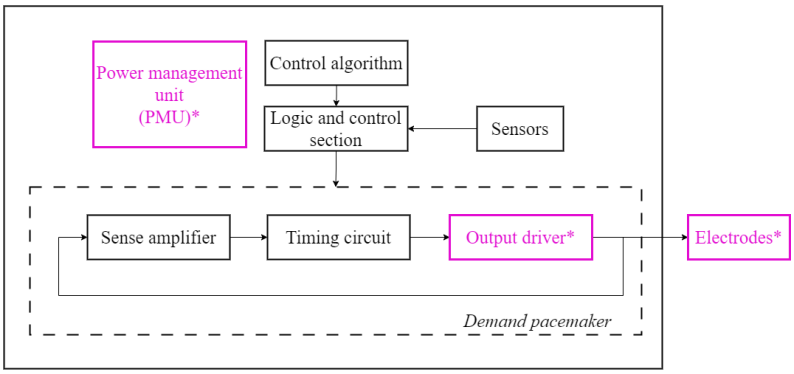

Figure 1.8: Block diagram of a rate-adaptive pacemaker system

asynchronous) counterparts.

Depending on the heart condition, the number and type of chambers in which the leads are implanted can differ, resulting in different types of pacemakers:

- Single-chamber pacemakers, which have one lead in either the right atrium or the right ventricle;
- Dual-chamber pacemakers, where two leads are implanted: one in the right ventricle and one in the right atrium; they are used to synchronize the contraction of the atria and the ventricle.
- Biventricular pacemakers (also called CRT-P for cardiac resynchronization therapy pacemaker), with leads in the right atrium, right ventricle, and left ventricle (via the Coronary Sinus vein), for patients with severe heart failure, to synchronize the contraction of all the chambers.

Pacemakers are thus categorized by a sequence of up to 5 letters, called the NBG code, developed by the North American society of Pacing and Electrophysiology (NASPE) and the British Pacing and Electrophysiology Group (BPEG). It refers to the system's possible pacing modes (e.g., AAIR) of operation as reported in Table 1.1 [6].

Position I	Position II	Position III	Position IV	Position V
Chamber(s) paced	Chamber(s) sensed	Response to sensing	Programmability, rate modulation	Antitachyarrhythmia function(s)
O = None A = Atrium V = Ventricle D = Dual (A + V)	O = None A = Atrium V = Ventricle D = Dual (A + V)	O = None T = Triggered I = Inhibited D = Dual (T + I)	O= None P = Simple programmable M = Multiprogrammable C = Communicating R = Rate modulation	O = None P = Pacing S = Shock D = Dual (P + S)

Table 1.1: The NASPE/BPEG Generic (NBG) Pacemaker Code

1.3.2 Leadless pacemakers

Technological developments in miniaturized electronics, low power integrated circuits, or catheter-based delivery systems cleared the path for the emergence of leadless cardiac pacemakers, a concept of long interest for cardiologists. Such a device allows one to overcome the shortcomings of conventional pacemakers as the latter are still prone to long-term complications and non-negligible risks of infection despite their efficiency. Most commonly lead-related, they include venous obstruction, insulation failure, or dislodgement and occur in approximately 9 - 12 % of all patients according to [72, 73]. Leadless pacemakers (LPM) take the form of a self-contained pill-shaped system, around one-tenth the volume of transvenous pacemakers, with comparable battery longevity depending on the pacing settings. They are placed directly in the right ventricle through a catheter in the femoral vein, as depicted in Figure 1.9a. The minimally invasive procedure [74, 75] eliminates the risk of pocket infection and scarring that could occur with CPM, also resulting in shorter recovery times.

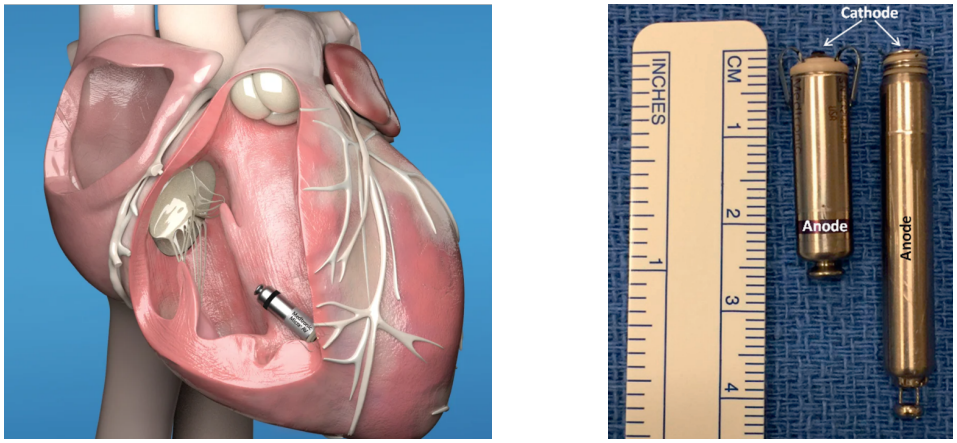

(a) (b)

Figure 1.9: (a) Leadless pacemaker implanted in the RV (figure issued from [76]), (b) Size comparison between the Micra TPS (25.9mm × 6.7mm) and Nanostim LCP (42mm × 5.99mm) (figure issued from [77])

While the idea of a self-contained device has been around since the 1960s [78], LPMs made their debut in 2012 with St Jude Medical's Nanostim Leadless Cardiac Pacemaker (LCP). The device received the CE mark in 2013 and had been implanted worldwide between 2013 and 2016 before being recalled due to battery deficiencies that appeared in a higher number of devices than initially anticipated [72]. They were followed by Medtronic's' Micra Transcatheter Pacing system (TPS) and most recently Abbott (which bought St Jude Medical in 2016) Aveir VR Leadless Pacemaker (LP) [79], both of which received FDA approval in 2016 and 2022 respectively. As of today, they are the only

two models available for implantation in humans (Boston Scientific is also developing its own leadless defibrillator system, the Empower MPS, which is currently in trials). Figure 1.9b shows the size difference between the Micra and the Nanostim implants.

The 0.8 cc MICRA and 1.3 cc AVEIR are respectively affixed to the heart muscle using 4 self-expanding nitinol tines and have an active screw-in helix fixation [80, 77]. LPMs are primarily designed for single chamber pacing (VVIR) limiting the number of eligible patients. However, as of July 2023, Abbott has received FDA approval for a dual chamber pacing system consisting of two communicating devices, one in the right atrium and one in the right ventricle [81, 82].

In most cases, the pacemaker can be safely retrieved through a procedure akin to the implantation [83, 84]. However, certain factors, such as fibrosis where body tissues scar around the device, or challenges due to inaccessibility to the device's docking button, the leadless pacemaker may be lodged within the heart. One solution is to deactivate the device before implanting a new one next to it. This raises the consideration of how many devices can be safely implanted within the heart and the potential complications it may entail [85, 84]. [86] have stated that up to three devices could be implanted in an adult, but this highlights again the need for serious reflection regarding the battery capacity in such a compact system. With ongoing research and development, we can expect even more refined and versatile leadless pacemakers in the future, further enhancing the quality of life for patients in need of pacing therapies.

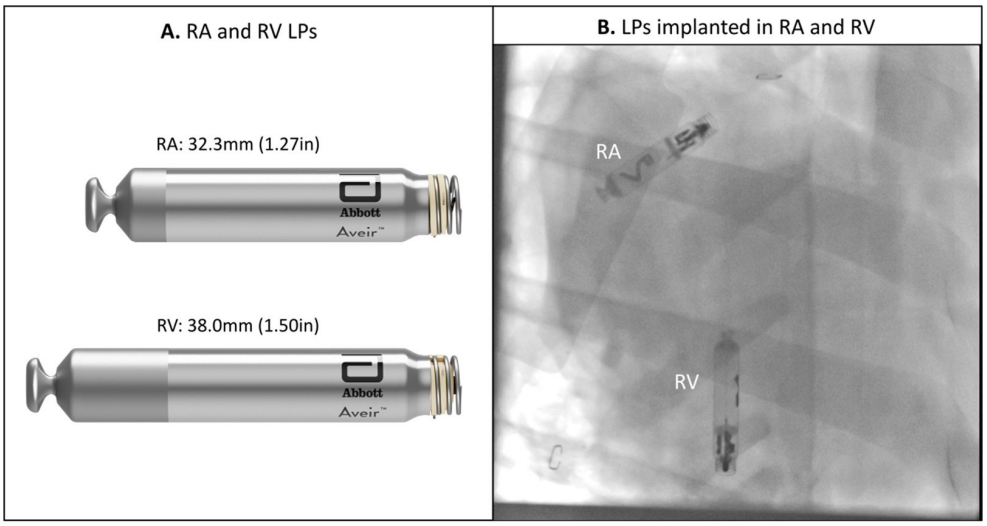

Figure 1.10: AVEIR DR implantation [82]

1.3.3 Pacemaker in animals

As discussed previously, using animal models can accelerate research on the mechanisms of cardiovascular diseases, including PAH. These diseases have been studied using pacemakers in larger mammals, such as dogs, cats or pigs [8, 9, 10, 11], but the small size of mice and rats necessitates more important adaptations to standard pacemakers. Therefore, new approaches had to be developed to enable the conduct of effective pacing studies in these smaller animals.

A first approach of a fully implanted pacemaker for mice was described in 2013 by Laughner et al [12], in co-development with Boston Scientific and Medtronic. Using both a battery-powered and a wireless-powered device, they were able to pace mice for 30 days, with a survival rate post-surgery of 90% (n=10).

This study showed the superiority of the wireless approach (1.11b) compared to the battery-powered method (1.11a), primarily due to its approximately 80% reduction in size, which highly enhanced post-operative survival rates in mice and also extended the device's lifespan while reducing overall costs. However, it is important to note some limitations of this approach. Pacing capabilities were confined to a 30-day window, limiting the duration of studies on the effects of pacing. Additionally, the device lacked programmability, limiting the scope of experiments it could be used in. Furthermore, wireless pacing meant intermittent sessions under anesthesia, as an external power induction device was required. Despite advancements in survival rates, there were still indications that the device was not entirely well-tolerated by mice.

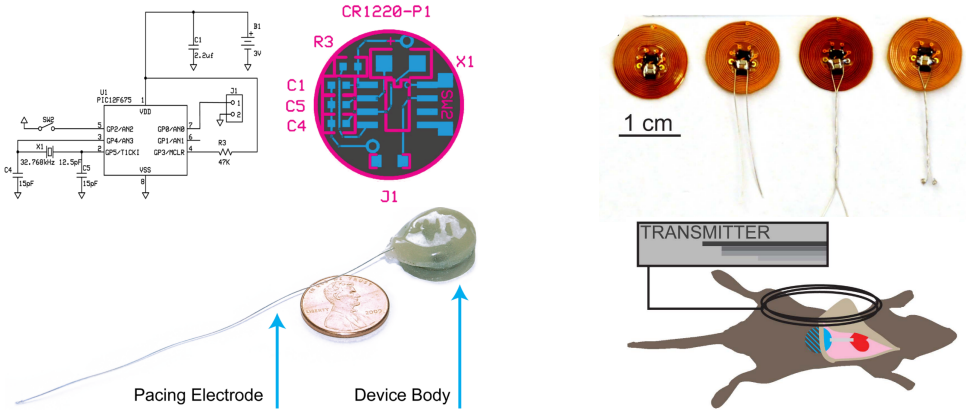

(a) (b)

Figure 1.11: (a) Battery-powered approach, (b) Wirelessly-powered approach [12]

In 2018, Hulsmans et al.[13] introduced another interesting approach with the aim of facilitating long-term pacing studies in mice, especially for conditions like arrhythmia and heart failure. To do so, they repurposed the leadless

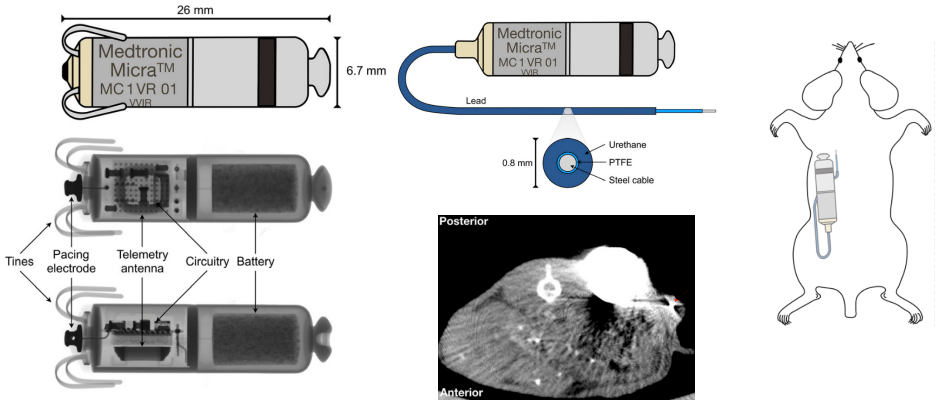

Figure 1.12: Implantation of a customized Micra TPS in a mouse [13]

Micra pacemaker, which currently holds the distinction of being the smallest pacemaker utilized in humans worldwide. In their adaptation, they replaced the tines and pacing electrode with a flexible lead, as depicted in Figure 1.12, and reprogrammed the software to surpass the clinical pacing rate limit of 170 bpm, enabling it to reach up to 1200 bpm to match the mice's heart rate. The device was surgically implanted in a dorsum pocket of the mouse, with the lead tunneling through and being attached to the heart using a superficial suture.

This method was well-tolerated by mice and allowed previously complicated long-term pacing studies to be performed on the rodent, including the treatment of complete heart block and bradycardia, as well as the establishment of a chronic mouse model of tachypacing-induced cardiomyopathy. However, while the Micra is remarkably small, its size remains significant for rats, potentially making it too invasive.

In his paper, Gutruf et al. [14] presented a wireless and battery-free multimodal pacemaker able to deliver both electrical and optical pacing, shown on Figure 1.13a. This multimodal pacing allows to study the long-term effects of optogenetic pacing by potentially mitigating the complications associated with chronic electric pacing (such as increased impedance or inflammation). The system uses μ-ILED to stimulate light-responsive proteins to induce cell depolarization. Additionally, the battery-free nature of the device makes it lightweight, small, and flexible. This study showcased the potential for a minimally invasive device compact enough to be fully implanted in rats and mice. However, its wirelessly-powered model necessitates animals to remain in close proximity to a power source. Also, the primary focus of this approach was to demonstrate the applicability of optogenetics for cardiac pacing, which deviates from the central objective of this thesis.

A more recent approach, presented by Choi et al. [15] in 2021, addresses the invasiveness associated with temporary pacing solutions used in hospitals. These solutions require implantation, sustained presence, and subsequent re-

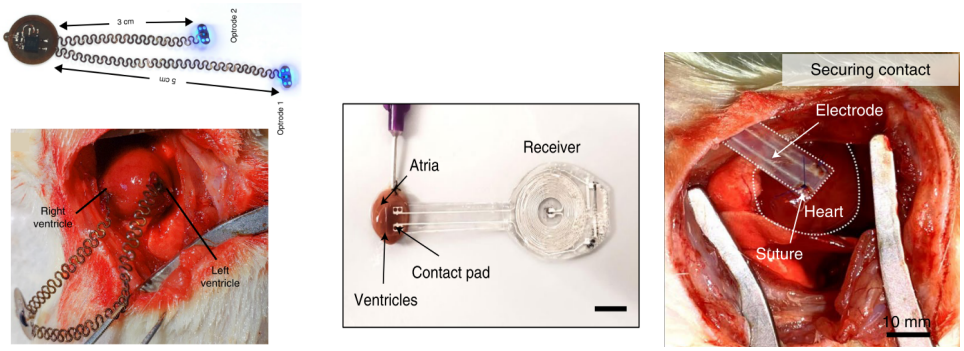

(a) (b) (c)

Figure 1.13: (a) Optogenetic stimulator [14], (b) Ex vivo demonstration on mouse heart, (c) *In vivo* implantation in rat model [15]

moval over a span of days or weeks. They successfully demonstrated a leadless, fully implantable, and completely bioresorbable pacemaker, without batteries, capable of effectively pacing in vivo rat models, among others. The device underwent both ex vivo (Figure 1.13b) and in vivo (Figure 1.13c) testings, providing pacing rates of 400-450 bpm, before completely resorbing after 46 days. This approach paves the way for a new generation of temporary cardiac pacemakers that operate independently without the need for external support and do not require removal after treatment. However, it is important to note that it does not align entirely with the long-term objectives of this thesis, as the pacemaker is not designed for extended studies. Additionally, the tested range of beats per minute (400-450 bpm) may not encompass the precise pacing requirements for studying PAH, which would ideally cover a range of cardiac frequencies up to 600 bpm.

As we have explored, various interesting and successful methods have been developed for pacing rats and mice. However, none of these methods were sufficiently specific for the study of cardiac frequency in the context of PAH, which demands prolonged and highly precise pacing of a group of rats with minimal invasiveness, preferably with a tunable stimulation frequency.

1.4 Conclusion

In this chapter, we focused on introducing fundamental knowledge of the heart and artificial cardiac stimulators to prepare for what follows. We have also explained the underlying motivation driving the development of a pacemaker for rats.

The evolution of artificial pacemakers from their inception to their current state of advanced technology underscored their pivotal role in treating various heart conditions. The emergence of LPM offered a promising alternative, avoid-

ing potential complications associated with traditional pacemakers, generally lead- or implant-related. This breakthrough, along with the advent of wireless and battery-free multimodal pacemakers, highlighted the constant drive towards more efficient, minimally invasive, and long-lasting pacing solutions.

Pulmonary arterial hypertension, a rare and severe cardiovascular condition, poses significant challenges in diagnosis and treatment. As such, our research intends to explore the modulation of heart rate in cardiopulmonary physiology to unlock essential insights into PAH and potentially broaden the therapeutic landscape for this condition.

The study of this fundamental mechanism goes through animal research, particularly with rats, and demands the use of an implantable cardiac pacing device adapted to rodents. The need for such a device is underscored by the lack of available systems tailored to small animal models and fitting our study requirements.

This thesis stands as a significant step towards the development of such device, meeting their unique physiological demands, starting with a primary focus on the design of the pulse generator. Indeed, while many aspects demand attention, one crucial element is the specification of the stimulation waveform, as it serves the main purpose of a cardiac pacemaker. This parameter is highly correlated with battery consumption, making it imperative to strike the right balance between efficacy and power preservation.

The next chapter will therefore discuss the different parameters to take into consideration to provide a clear specification of the stimulation waveform.

Chapter 2

Specification of the stimulation waveform

2.1 Introduction

As presented in the previous chapter, the primary function of a pacemaker is to generate and deliver a stimulating pulse (or pacing pulse) to induce myocardial cell depolarization. The characteristics of this pulse, which takes the form of a waveform signal, establish the stimulation's efficiency and the energy drawn from the power supply. A suitable waveform is thus key to the design of a reliable and low-power device. This chapter sets out to establish the appropriate stimulation for cardiac pacing in rodents. The framework for specifying the stimulus is divided into two main sections. The first part seeks to review equivalent models for the pacing load and investigate pacing waveforms employed in current devices, providing further insight for formulating a theoretical waveform. The second section outlines two acute in vivo experiments conducted on rats, which helped assess the validity of our proposed stimulation.

2.2 Pacemaker load and stimulation waveform

2.2.1 Model of the pacemaker load

To understand the intricate electrical behavior of the heart, researchers have developed equivalent electrical circuit models that aim to replicate the complex interactions among cardiac cells and their surrounding tissues. Ranging from relatively straightforward to more elaborate, these models serve as invaluable tools for simulating cardiac activity, predicting arrhythmias, and designing cardiac devices. Here, we will present a quick overview of the typical equivalent electrical circuit models used to represent the heart tissue to identify a suitable circuit model for the pacemaker load.

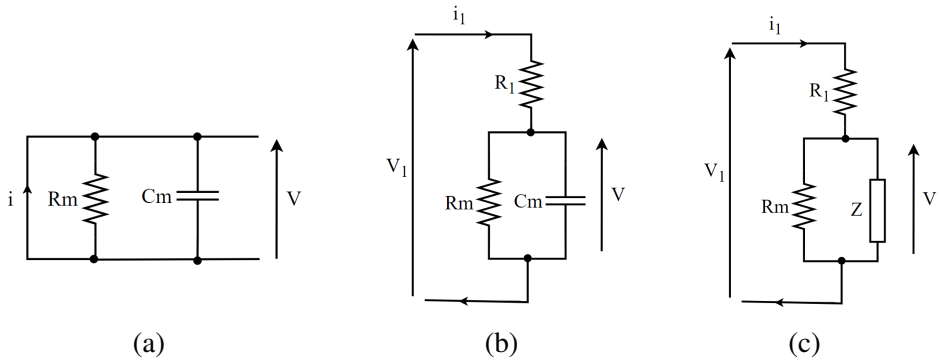

Figure 2.1: (a) Equivalent model of the cardiac cells used by Klafter in [24], (b) Equivalent model of the pacemaker load used by De Visme et al. in [87], (c) Cole-Cole model

The majority of circuit models integrate resistors and capacitors in various arrangements to simulate tissue, and their values generally depend on the characteristics of the tissue [88].

In his study of 1973, Klafter [20] considered the model proposed by Myers and Parsonnet in order to find an energy optimized stimulation. This model comprised a parallel arrangement of a resistance Rm and a capacitance Cm, intended to depict the membrane resistance and capacitance of a cell (Figure 2.1a). However, this circuit model did not account for the minimal "energy dissipation in the load or the least energy consumption from the battery", which was highlighted by De Visme et al. [87]. In their own work on optimal pacing pulses, De Visme and Furness aimed to address these limitations by considering a more faithful electrical model [87] using Lapicque model. This model, depicted in Figure 2.1b, is very commonly employed to represent body tissues and often used to simulate the stimulation of the nerve membrane. It relies on a resistor of R1 in series with a capacitor Cm in parallel with another resistor Rm, wherein R1 symbolizes the resistance of the intracellular fluid, while Rm and Cm are the resistance and capacitance of the membrane, respectively [89, 88]. Based on Lapicque model, more advanced equivalent circuit can be found by replacing the capacitance with an impedance Z, serving as circuit representations of the Cole-Cole equation, which characterizes tissue properties (Figure 2.1c).

Using De Visme work [87] as a reference, [27] undertook the development of a pacemaker with the following load configuration: R1 = 1 kΩ and R = 100 kΩ and C = 300 pF. These values will be kept in mind for our model.

2.2.2 Stimulation waveform

The electrical impulse delivered is defined by its pulse amplitude (measured in volts) and pulse duration (measured in milliseconds). The minimum amount

of electrical energy needed to capture the heart, that is, successfully stimulate it, is called the stimulation threshold. As it is inherent to the individual, it may fluctuate due to changes in body activity, medication, or electrode characteristics, among others. As stated by [25], a pulse of sufficient amplitude must be applied to stimulate excitable tissues effectively. Similarly, to prevent damage to body tissues and reduce pain in the patient, it is preferable to have a longer pulse duration for depolarization to dissipate into the surrounding tissue. The extended pulse width also allows for a lower threshold voltage, which, at some point, becomes independent of the duration [90]. However, it must be taken into account that, for a given amplitude, a longer duration means more energy delivered, leading to higher power consumption. The strength-duration curve, depicted on Figure 2.2, plots the exponential relationship between the pulse amplitude and pulse duration, which gives a good depiction of the trade-off between the two, for an efficient battery-optimized stimulation [6, 16, 17, 18]. Two main points are to be considered: the rheobase (in V), defined as the threshold voltage, i.e. minimal amplitude, resulting in capture at an infinitely long pulse duration, and the chronaxie (in ms), the minimal time duration at twice the rheobase amplitude. It is highly relevant when designing a pacemaker as it approximates the waveform that paces with the lowest energy [91].

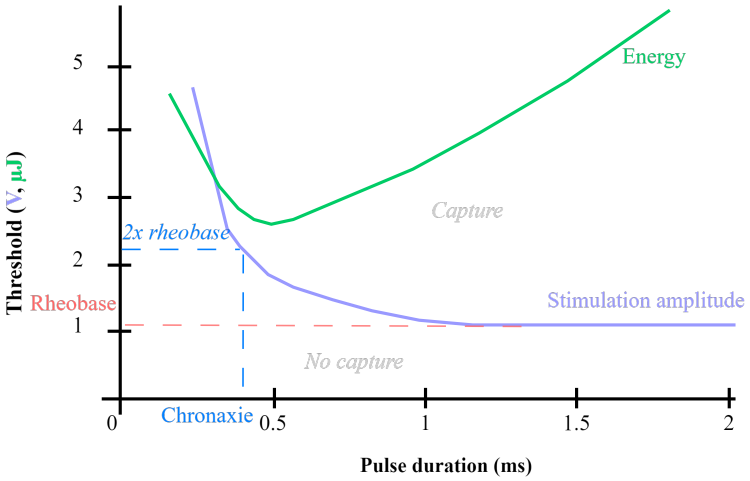

Figure 2.2: Strength duration curve

Any waveform on or above the strength-duration curve ensues cell depolarization. However, as the threshold might vary, safety margins are set to ensure capture (typically twice the amplitude threshold or three times the pulse threshold) [6, 17, 16]. In rats, a typical heart rate falls within the range of 240 to 400 bpm as seen in Chapter 1. However, for our research, we contemplate elevating the heart rate to upper frequency and hyperphysiological ranges, targeting cardiac frequencies between 400 to 600 bpm, corresponding to pulse periods of 100 to 150 ms, following equation 2.1 [16].

$$T[ms] = \frac{60000}{RATE[bpm]} \tag{2.1}$$

In future investigations, we might consider rate adaptive features. Indeed, as the heart adapts its rhythm to the higher frequency, if the stimulation is slower than the animals' intrinsic heartbeat, the effect of the pacemaker will not be perceived.

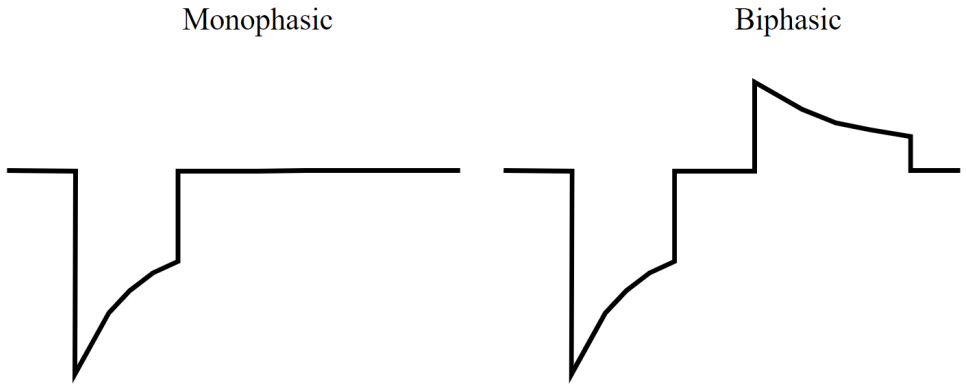

Figure 2.3: Exemples of monophasic and biphasic truncated exponential waveforms

There are two typical waveforms generally used for pacing: monophasic and biphasic (Figure 2.3). Early implantable pacemakers or defibrillators mainly considered square-shaped monophasic pulses. Still, studies by [19, 20, 21] have shown that biphasic shapes are found to be more optimal in terms of battery efficiency and voltage thresholds, in addition to being safer for the tissue [22]. Typically, the biphasic stimulation [21, 25, 92] consists of two pulses: a first short negative (cathodal) pulse of high amplitude to trigger the depolarization of the cardiac cells, followed by a delayed, longer positive (anodal) recharge pulse, for the heart tissue to return to a charge neutral state (Figure 2.4)[23]. This biphasic shape lowers the pacing threshold and prevents the degradation of the heart tissue caused by ions gathering around the electrodes. Besides, triangular forms, such as ramps ("sawtooth") or exponentials, are preferred by Roy et al.[19] and Klafter [24] over square or rectangular ones for their lower energy consumption and more significant physiological effect on the heart. The consensus is that a ramped waveform would offer stimulation with minimal energy consumption. However, it's noteworthy that manufacturers have not adopted this pulse shape for implantable pacemakers but rather mainly rely on capacitive discharge that gives more of an exponential shape, as, as Stokes said in [93], "the "optimum" waveform takes more energy to generate than it saves".

The choice of stimulation waveform for cardiac pacing is crucial. While monophasic square-shaped pulses were once common, extensive research favors

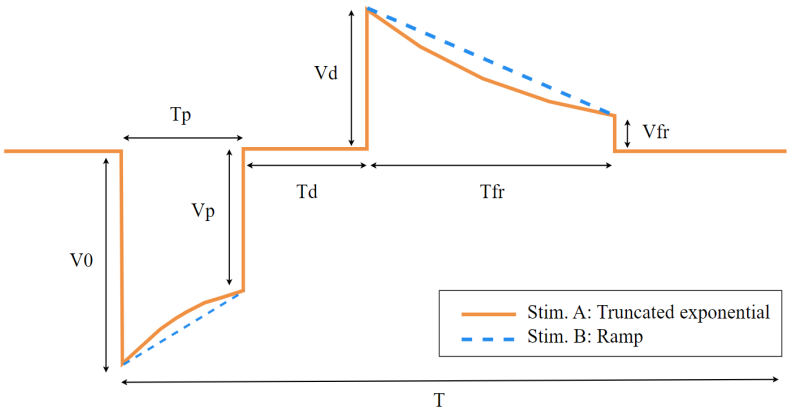

Figure 2.4: Stimulation waveform with an exponential (solid line) or ramp (dotted line) discharge

biphasic waveforms due to their efficiency, safety, and lower tissue damage. Triangular waveforms like ramps and exponentials offer energy savings and physiological benefits. Given these considerations, we decided to settle on a biphasic stimulation with either linear or exponential discharge for pacing in rats and compare their efficiency. Both waveforms are displayed on Figure 2.4. Times and voltage references, based on Lahtinen et al.'s [25] pacing pulse for later references.

2.3 Waveform validation through in vivo experimentation

After establishing potential stimulation waveforms, we proceeded to assess their efficiency in actual pacing in rats. To achieve this, we conducted a first in vivo experiment. The objective was to restore a normal heart rate of 300 to 400 bpm in a healthy rat, after it had been pharmacologically reduced to around 200 bpm using ivabradine (IVA). The experiments and their results were the subject of a conference paper presented at ICECS 2021 [26]. All experiments were carried out according to the European Community guiding principles in the Care and Use of Animals (2010/63/UE, 22 September 2010), the local Ethics Committee (CREEA Ile-de-France Sud) guidelines, and the French decree no. 2013-118, 1 February 2013 on the protection of animals used for scientific purposes (JORF no. 0032, 7 February 2013, p2199, text no. 24). Authorizations to perform animal experiments according to this decree were obtained from the Ministère français de l'Agriculture, de l'Agroalimentaire et de la Forêt (agreement no. B 92-019-01). We used one adult male Sprague Dawley rat from the AnimEx platform (Châtenay-Malabry, France).

2.3.1 Pacing module description

We used an FPGA-based prototype of a programmable pulse generator capable of delivering a configurable waveform at fixed pacing rates of 250, 300 and 400 bpm for the study. The block diagram of the system is shown in Figure 2.5. It had two operable biphasic shapes: a truncated exponential (referred to as A), based on Lahtinen et al.'s [25] work, and a ramp shape (referred to as B) proposed by Roy et al. [19] in accordance with our literature review. However, any waveform at any potential cardiac frequency could be programmed.

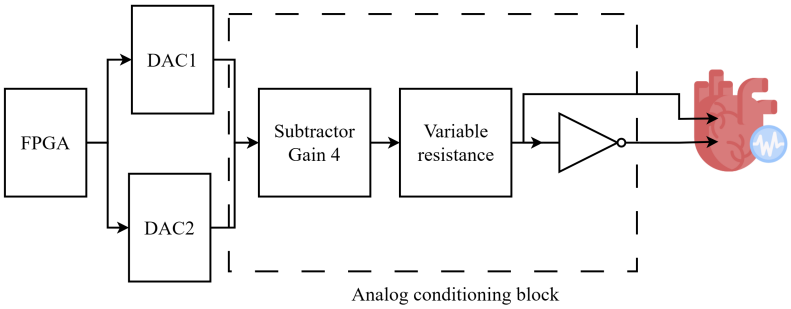

Figure 2.5: Experimental bank for pacing

A differential stimulation, achieved by combining the pulse with its inverted form, is delivered to the heart through a bipolar electrode. It has a peak-to-peak amplitude of 8 V, and we incorporated a variable resistance into our design to finely adjust the waveform's amplitude and mitigate potential tissue damage. Both the frequency and waveform could be dynamically adjusted during pacing. The circuit was powered with $\pm$ 5 V and had an overall power consumption of approximately 56.7 mW for each waveform.

In our design, the generation of these pulses was based on the architecture portrayed in Figure 2.6. This architecture named Stimulation takes as inputs the desired frequency and waveform type settings, as well as an On/Off State command. It produces a signal representing the stimulation waveform, another signal for offset elimination in the waveform, and control signals for the 12-bit D/A Converters (MCP4821). Below, we will elaborate on the behavior of the components instantiated in the Stimulation block, following the waveform signal's generation process.

First, we have a clock unit manager Clock_unit that generates a 3.125 MHz clock from the FPGA's 50 MHz system clock.

Then, the block named Control_unit produces three sets of signals:

- Signals responsible for synchronizing and controlling the parallel-to-serial converters.
- Signals to command the Digital-to-Analog Converters (DACs) (refer to Figure 2.7a).

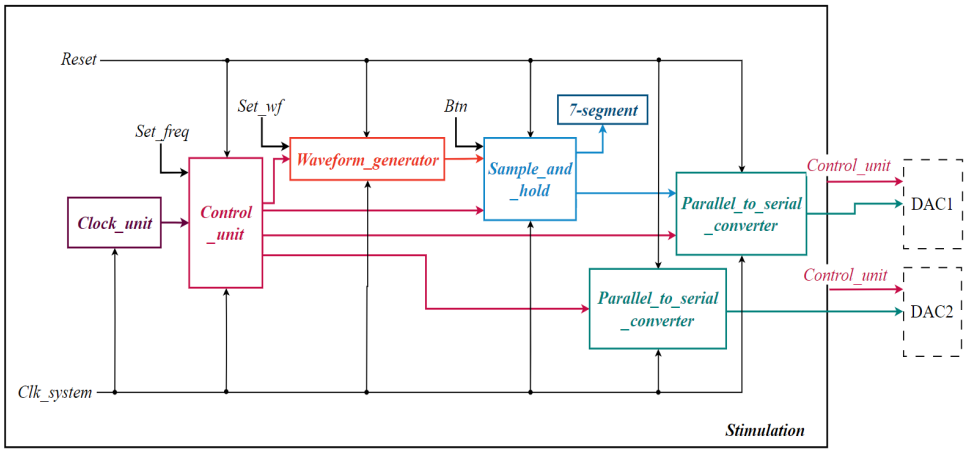

Figure 2.6: Architecture of the programmable pulse generator

- Signals that define the characteristics of the pacing waveform to be generated.

This third group includes time constants (Tp, Td, Tfr, and T) which correspond to the time intervals mentioned in Lahtinen et al. [25] where T represents the pulse width of the stimulation, Tp and Tfr denote the durations of the negative and positive discharges respectively and Td is the time delay between the two discharges as displayed in Figure 2.4.

For our validation purposes, a pair of switches, represented by a 2-bit vector Set_freq, defines the pulse rate of the stimulation ("00" for 250 bpm, "01" for 300 bpm, and "11" for 400 bpm). This pulse rate value is then transmitted to the Sample_and_hold block.

Furthermore, this Control_unit block generates a 1 V step signal, programmed on 12 bits, which is later used to eliminate the offset from the Waveform_generator block output.

This Waveform_generator block outputs the stimulation pulses in the form of a 12-bit signal, which is satisfactory for our application. The choice between stimulation waveform A or B is determined by the value of the Set_wf switch ('0' or '1'). It is important to note that the amplitude of this output is four times smaller than required and is offset by 1 V. This design choice ensures that the biphasic nature of the signal is not compromised and falls within the range of the DAC output, which in our case spans from 0 and 4.095 V.

To reduce the complexity and thus the computing power, the truncated exponential waveform is obtained by fetching its values from lookup tables (LUT) rather than using a filter. The exponential values in the LUTs were calculated beforehand based on equations (2.2) and (2.3).

$$For\ 0 < t \leq T_p : V(t) = V_0.e^{\frac{t}{T_p}.ln(\frac{V_p}{V_0})} + 1 \tag{2.2}$$

$$For\ T_d < t \leq T_{fr} : V(t) = V_d.e^{\frac{(T_d - t).ln(\frac{V_{fr}}{V_d})}{T_d - T_{fr}}} + 1 \tag{2.3}$$

The values for the linear waveform were computed in situ (FPGA) using equations (2.4) and (2.5) as these operations have low computational demands. The truncation after the division is managed by 12 significant bits.

$$For\ 0 < t \leq T_p : V(t) = \frac{V_p - V_0}{T_p}.t + V_0 + 1 \tag{2.4}$$

$$For\ T_d < t \leq T_{fr} : V(t) = \frac{V_d - V_{fr}}{T_d - T_{fr}}.t + \frac{V_{fr}.T_d - V_d.T_{fr}}{T_d - T_{fr}} + 1 \tag{2.5}$$

The Sample_and_hold block takes the output of the Waveform_generator and retains its value. If the state of the attached button is '0', it produces a 1V step signal, which is canceled by the offset of the Control_unit, resulting in no stimulation output. In the case of a '1' encoding, the stimulation signal remains unchanged. Correspondingly, the 7-segment block displays either "OFF" or the value received from the Control_unit depending on the button state.

Finally, the Parallel_to_serial_converter adds 4 configuration bits, needed for the DAC to initiate its write command, to the 12-bit stimulation waveform signal. It then converts the resulting 16-bit signal to a serial format and transmits it to the DAC (Figure 2.7a).

The correct amplitude adjustment and offset suppression are accomplished by employing a subtractor circuit with a gain of 4. This circuit is placed after the DAC and utilizes both the previously mentioned step signal and the stimulation signal.

To demonstrate the viability of our system, we have implemented our architecture on FPGA (10M50DAF484C7G). It uses 3% of the LUTs and logic elements, along with only 95 registers, proving the lightness of our programmable pacing architecture. We then designed a printed circuit board (PCB) mounted with the necessary components for the analog conversion. The resulting prototype is shown in Figure 2.7b.

2.3.2 Experimental validation

The experimental protocol aimed to demonstrate that the programmable pulse generator could successfully restore a physiological heart rate following pharmacologically induced reduction. The rodent was put under anesthesia with 5 % isoflurane inhalation before tracheotomy was performed to facilitate mechanical ventilation. Anesthesia was sustained at 2 % isoflurane concentration. In order to obtain real-time measurements of arterial blood pressure, a fluid-filled catheter was surgically introduced into the left carotid artery. This catheter was linked to a disposable transducer, allowing for continuous arterial pressure

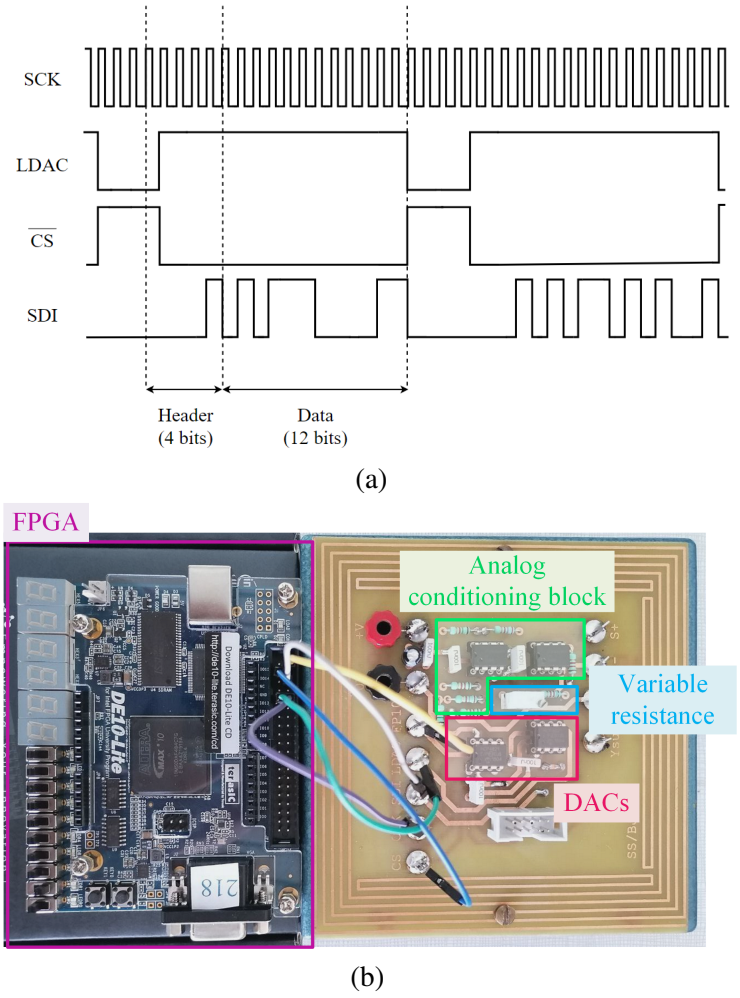

Figure 2.7: (a) DAC control signals, (b) Prototype used for the in vivo experiments

monitoring. The acquired arterial pulse waveforms were captured and recorded via the LabChart 8 software (AD Instruments). The right atrium, which served as the stimulation site (Figure 2.8), was accessed through a median sternotomy procedure.

Throughout the experimental protocol, the assessment of effective cardiac stimulation was carried out through visual examination of both the heart itself and the frequency of the pulse wave. The values corresponding to heart rate, as well as systolic, diastolic, and mean blood pressures (abbreviated as SAP, DAP, and MAP, respectively), were quantified during the post-processing phase. Figure 2.13b depicts these pressures' recordings from a second experiment. The tests proceeded as illustrated in Figure 2.9.

We measured the evolution of the heart rate and arterial blood pressures at distinct phases :

- At baseline (BL), following successful access to the heart,

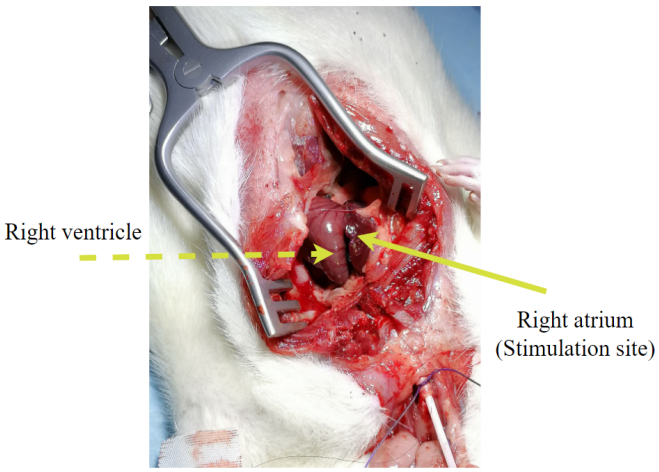

Figure 2.8: Stimulation site (RA)

- 10 minutes after the administration of IVA (5 mg/kg) which reduced the heart rate to approximately 220 bpm,
- During the application of electrical stimulation to the right atrium, using both A and B waveforms. These stimulation sequences were interspersed with periods of rest (REST) where no stimulation was applied.

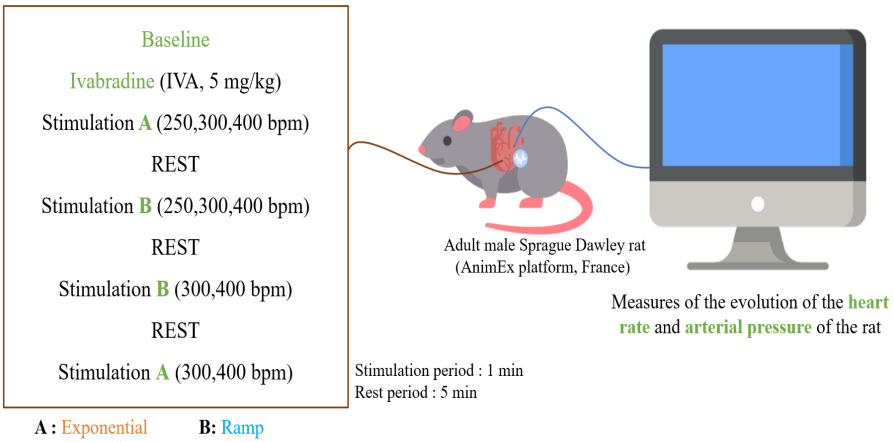

Figure 2.9: Experimental protocol for waveform validation in rats. BL: without stimulation baseline; IVA: Ivabradine without stimulation; A/B (250, 300, 400 bpm): stimulation with waveform A or B at 250, 300 or 400 bpm, respectively

For both waveforms A and B, we recorded the heart rate and arterial pressures during stimulation sessions at rates of 300 and 400 bpm. Each stimulation session lasted for approximately 1 minute to ensure the establishment of hemodynamic stability. Between these active stimulation phases, we allowed for resting periods lasting 5 minutes. The heart rate measurements

were derived from the analysis of 10-second samples obtained during periods of stable hemodynamic conditions. The electrode tips were manually positioned on the right atrium to facilitate impulse transmission and induce the desired stimulation. Table 2.1 summarizes the measures taken during the tests. The electrical stimulation at 250 bpm, being very close to the animal's heart rate (approximately 220 bpm), proved to be ineffective and led to ventricular fibrillation (which was resolved through resuscitation maneuvers) and hemodynamic compromise. As a result, we opted to utilize pacing rates of 300 and 400 bpm for subsequent tests. Applied pacing pulses at 300 and 400 bpm resulted in stable heartbeats at the desired rates for both waveforms, and we found no significant disparity in the efficacy of the stimulation. A sample of the blood pressure measured before and during the exponential stimulation is shown in Figure 2.10.

Condition	**Stim. rate (bpm)**	**SAP (mmHg)**	**DAP (mmHg)**	**MAP (mmHg)**	**Measured HR (bpm)**
Baseline	-	99	61	73	325
IVA	-	84	40	55	217
Stim. A	300	97	48	75	300
Stim. A	400	90	64	68	398
REST 1	-	95	50	65	217
Stim. B	300	86	40	57	300
Stim. B	400	64	28	41	400
REST 2	-	121	75	92	229
Stim. B	300	97	41	67	300
Stim. B	400	82	47	50	398
REST 3	-	125	86	103	230
Stim. A	300	88	48	63	271
Stim. A	400	65	28	40	400

Table 2.1: Stim. A: stimulation with waveform A; Stim. B: stimulation with waveform B. bpm: beats per minute; SAP: systolic arterial pressure; DAP: diastolic arterial pressure; MAP: mean arterial pressure; HR: heart rate.

Measurements of blood pressure and cardiac frequency obtained during

these in vivo experiments in rats have validated the effectiveness of our system in restoring physiological heart rates in the animals. Through experimental validation, this study contributes to the assessment of two heart-stimulating waveforms for rats, -with an exponential or linear discharge-, and a flexible architecture allowing for real-time integration and modification of the waveform's frequency, amplitude, and shape.

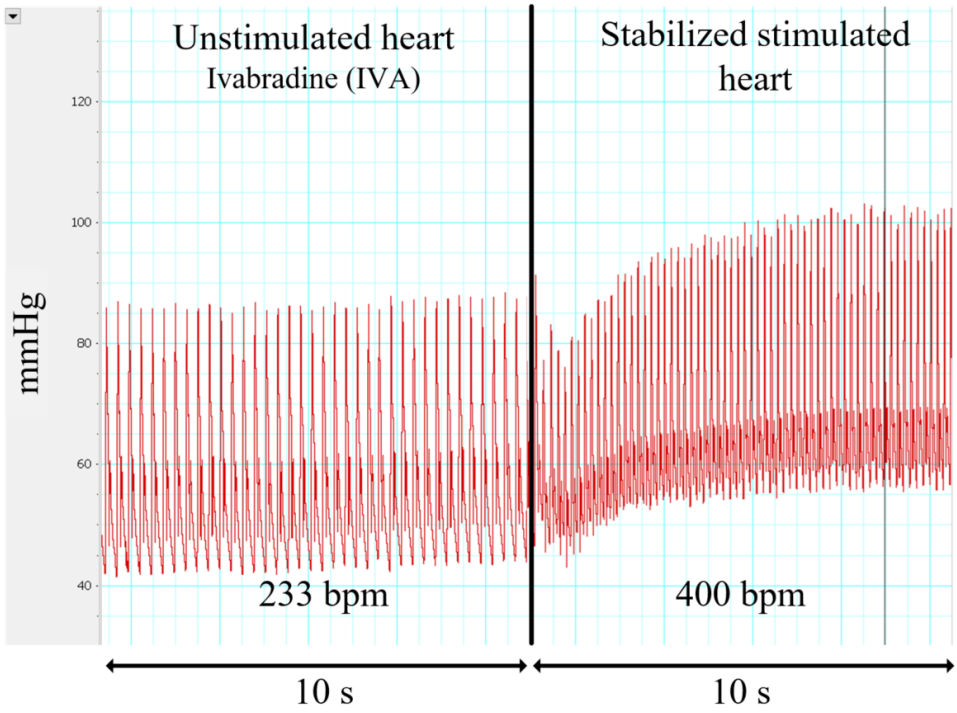

Figure 2.10: Samples of arterial pulse pressure. Left hand side panel: without atrial stimulation with the pulse generator (unstimulated heart) but with pharmacologically reduced heart rate with Ivabradine (IVA) injection (heart rate measured at 233 bpm). Right hand side: right atrial stimulation with the pulse generator at 400 bpm resulting in an increased measured heart rate (400 bpm).

During the study, we also observed a variability in the value of heart impedance, ranging from 0.2 to 1.2 MΩ. It should be noted that these measurements were taken on the heart right after it was removed at the end of the experiment, which explains the higher values observed compared to those mentioned in Section 1. It is crucial to emphasize that excessive current level has the potential to harm body tissues or result in necrosis, hindering effective pacing. Unlike humans who can easily communicate feelings of pain or discomfort, assessing these sensations in animals poses a greater challenge. Therefore, we now want to establish the optimal range of allowable current to ensure both safe and effective cardiac stimulation in rodents.

2.4 Minimum pacing current specification

In the previous study, we validated a pacing waveform for cardiac stimulation in small rodents, confirming the suitability of the shape, frequency, and differential voltage of our stimulation. Yet, the appropriate range of current has not been measured and a notable variation in cardiac impedance has been highlighted. This variability can be attributed to the dependence of the tissue on several biological factors, as well as the placement of the pacing electrodes, making it challenging to evaluate beforehand. However, measuring and adjusting the current is relatively straightforward. Excessive current can potentially harm body tissues or result in necrosis, hindering effective pacing. While humans can easily communicate pain or discomfort, evaluating these sensations in animals is more challenging. Consequently, the objective of this study is to determine an acceptable current range that will ensure stable and efficient pacing of the heart while preserving the integrity of the cardiac cells. This includes identifying the minimum current required for successful stimulation and its optimal value.

2.4.1 Pacing module description

For these tests, we opted to apply the biphasic truncated exponential waveform illustrated in Figure 2.4, which had previously proven to be effective. The peak-to-peak amplitude of the differential output was 10 V. To align with the characteristics of our long-term studies requirements, we set pacing frequencies corresponding to the upper physiological and hyperphysiological range of 400, 450 and 500 bpm. To achieve a more precise measure of the current passing through the heart during pacing, we made two major modifications to our prior prototype. First, we removed the variable resistance from the analog conditioning block (see Figure 2.5) and added a resistor bank before the lead. This bank consists of a set of 10 selectable resistors in series, each with a value of 100 kΩ, resulting in a total equivalent resistance of 1 MΩ. Secondly, we connected an oscilloscope in parallel with the equivalent resistor to visualize and record the stimulation's differential output The associated current value was then calculated with Ohm's law.

$$I = \frac{U}{R} \tag{2.6}$$

The block diagram of the updated prototype is pictured in Figure 2.11.

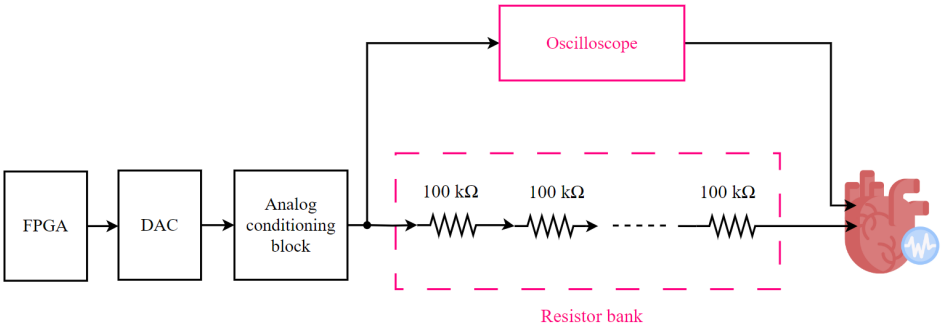

Figure 2.11: Experimental bank for current measure

2.4.2 Experimental protocol and results

Two male Sprague Dawley rats were utilized for the study. The anesthesia procedure and access to the stimulation site (right atrium) were carried out following the same protocol as in our initial experiments [26]. Live arterial pulse waves were recorded using LabChart 8 software (AD Instruments), and the effectiveness of the stimulation was evaluated through visual examination of the heart and ECG signals obtained from electrodes placed on the rodents' upper paws. In accordance with the long-term studies, we did not administrate IVA and maintained the animals' intrinsic cardiac frequency. Their baseline heart rate was measured to be around 260 bpm. To prevent tissue damage, we initially delivered the lowest available current, corresponding to the highest total resistance of 1 MΩ. In each test, we gradually increased the current by reducing the value of the equivalent resistance in 100 kΩ increments.

Figure 2.12: Electrode placement on the rodent heart

As applying stimulation with a sufficient current resulted in steady heartbeats at the targeted rates of 400, 450, and 500 bpm, we decided to collect the data exclusively for the 400 bpm pacing. No evidence of damage was observed in the cardiac tissue. The results showcased interesting insight regarding the

current for effective pacing in rodents. It suggests the following:

- When using the 1 MΩ resistor, stimulation was observed to be inefficient as it was too weak to induce proper pacing.
- Stimulation carried out through the 300 kΩ resistor resulted in a derived current of 20 µA. Although this led to an average cardiac frequency at the desired level, occasional skipped heartbeats were observed.
- Using a resistance of 200 kΩ, we attained a current of 30 µA, which ensued in stable and efficient pacing, thus establishing our threshold value.
- Optimal stimulation was achieved with a current of approximately 60 µA (using R = 100 kΩ), resulting in extremely stable pacing and consistent pressure levels.
- This underscores the complex RC behavior of cardiac tissue, highlighting not only its resistive characteristics, as initially hypothesized, but also its capacitive aspects.

Figure 2.13 shows the currents and pulse pressures obtained during the experiments.

These experiments yield two main conclusions. First, to effectively pace the rodent's heart, a minimum current of 30 µA is required when using the selected biphasic waveform. Second, based on this current requirement, we can roughly estimate the approximate impedance of the cardiac tissues of rats for the specified electrode placement. Let R_{eq} be the equivalent resistor of the resistor bank, R_{load} the equivalent resistance of the pacemaker load, I_{stim} the stimulation current, and V_{pp} the peak-to-peak amplitude of the stimulation. By Ohm's law we have :

$$\frac{V_{pp}}{R_{eq}+R_{load}} = I_{stim} \tag{2.7}$$

Hence,

$$R_{load} = \frac{10}{30.10^{-6}} - 200.10^{3} = 133k\Omega$$

At low frequencies, a capacitance behaves like an open circuit (infinite resistance), thereby the model employed by De Visme can be simplified to an equivalent resistance, R_{eq} = R1 + R. The measured value of R_{load} thus aligns with the resistive part of the heart tissue model considered by [27] cited in Section 2.2.1.

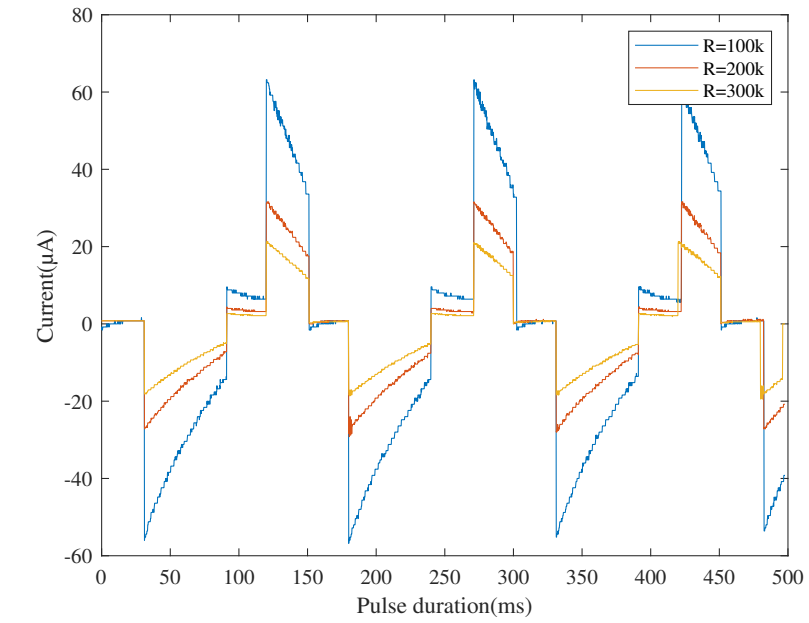

(a)

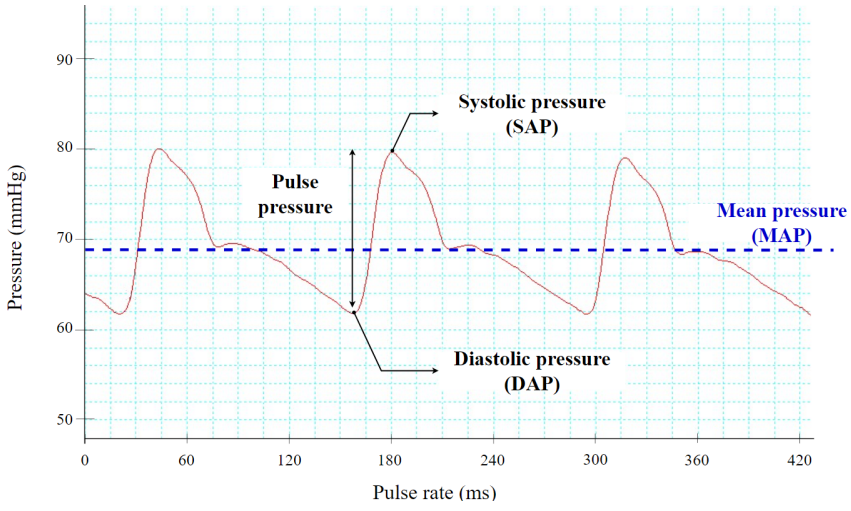

(b)

Figure 2.13: Measured (a) currents, (b) Pulse pressure

2.5 Discussion

Given the limitation of short-term experiments in the scope of this thesis, the long-term effects of chronic pacing on cardiac tissues could not be assessed and should be addressed in future investigations. Additionally, one should keep in mind that the threshold value may require reevaluation over time, as the resistance of the body tissue could potentially increase due to damage

or inherent adaptive abilities of the body. It is also worth mentioning that the electrodes were not affixed and thus the stimulation efficiency may vary depending on their placement.

2.6 Conclusion

In this chapter, we discussed different aspects of the waveform specification for pacing the rat. We started with a synthetic overview of heart models to establish a reliable model for the pacemaker load, along with the exploration of stimulation waveforms commonly employed in human pacemaker development.

This allowed us to consider diverse waveforms options, which we tested and validated through in vivo experiments on rats with an FPGA prototype. The architecture of the system and the mathematical equations governing these waveforms were also detailed. Accordingly, we have shown that our pacing pulse induces successful and safe pacing in the small animal and characterized the orders of magnitude for the current with a second in vivo experiment. Consequently, our objective is to generate a biphasic exponential waveform at varying pulse durations ranging from 100 ms to 150 ms, with a minimum current of 30 µA. Additionally, we have estimated that the pacemaker load can be modeled with an equivalent resistance of 133 kΩ at our specific pacing site, matching with models used in previous studies.

Building upon these insights, the subsequent chapter will delve deeper into the design of our integrated circuit to generate the stimulation pulse. This critical phase represents the bridge between theoretical insights and practical implementation, paving the way to materialize the proposed pacing waveform and contribute to the advancements in cardiac pacing technology tailored for small animal models.

Chapter 3

Design of the integrated circuit for stimulation

3.1 Introduction

With the stimulation waveform now defined, our attention turns towards the design of the associated integrated circuit (IC).

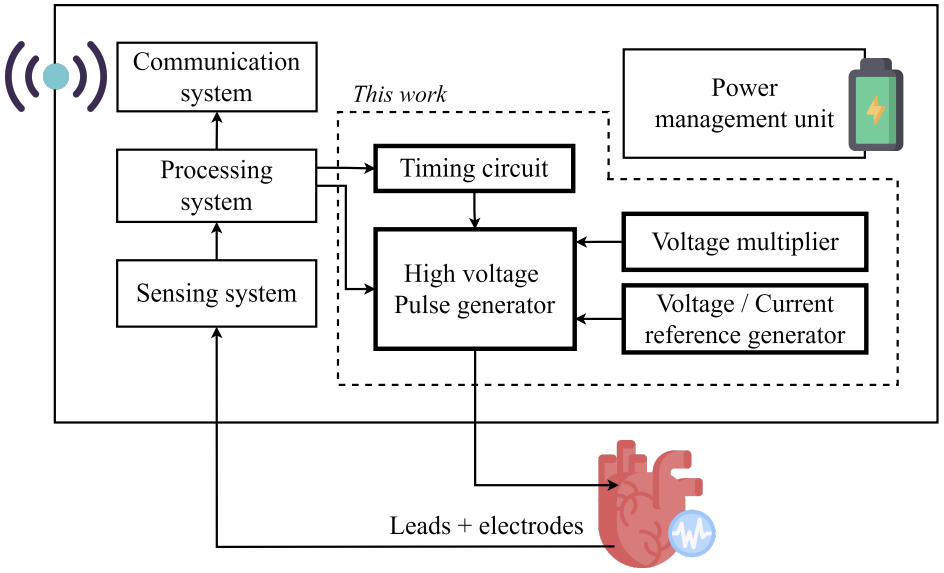

Figure 3.1: Block diagram of a modern pacemaker

As outlined in Chapter 1, the general architecture of a modern pacemaker encompasses various blocks, including a power management unit, sensors, and a processing system, among others. In this thesis, we place our focus on the stimulation aspect which stands as the most important feature. As implied in Figure 3.1, our stimulation system comprises two key elements: the high-voltage pulse generator, responsible for shaping and generating appropriate

pacing pulses to small rodents, and the oscillator, which orchestrates the system's functions and commands the pulse generator.

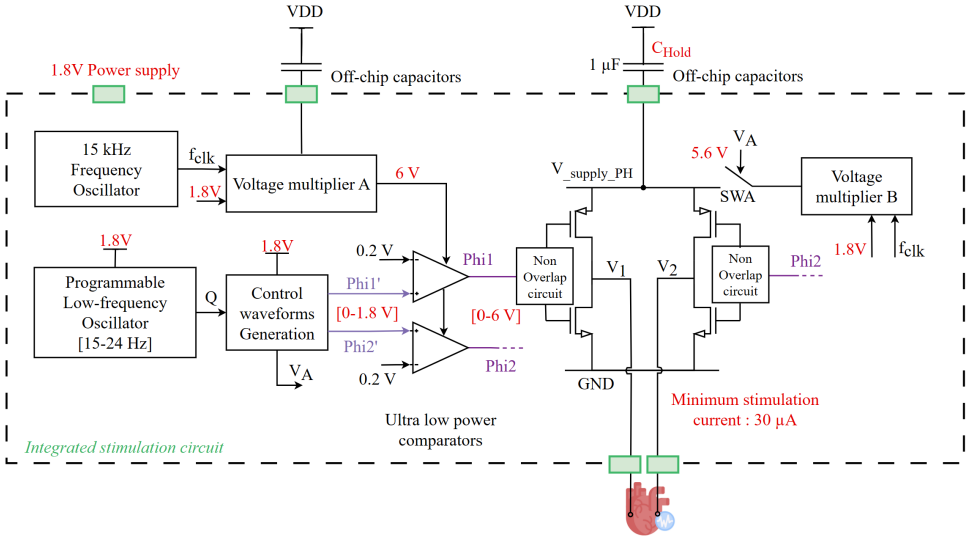

Figure 3.2: Stimulation circuit block diagram

Our review of the literature, along with our experiments on rats for waveform validation and specification, have led us to propose the architecture presented in Figure 3.2. The whole circuit operates on a 1.8 V voltage supply. To obtain the desired waveform with a minimum current of 30 µA, an H-bridge circuit is powered by a 5.6 V supply coming from a voltage multiplier, denoted as voltage multiplier B. This multiplier, must have a short response time to recharge an off-chip capacitor at each waveform repetition. A command signal, named V_A, is necessary to control the charge-discharge cycle of this capacitor by enabling the closure of the P-type switch, SWA. For the command of the H-bridge, signals Phi1 and Phi2 are created with a low-frequency oscillator and a control waveform generator. These control waveforms are reshaped from [0-1.8] V to [0-6] V using an ultra-low power (ULP) comparator supplied by the voltage multiplier A. Both multipliers are driven by a 15 kHz voltage controlled oscillator (VCO). The following sections will provide a comprehensive breakdown of the H-bridge and the generation of its command signals, detailing the function and simulation results of each individual block. The presentation of the voltage multipliers, driven by the 15 kHz VCO requires an understanding of the nested behavior of both circuits and will thus be explained in the next chapter. Figure 3.3 illustrates the different control signals Phi1, Phi2 and VA, as well as V_{supply_PH} the supply of the H-bridge stemming from the capacitor's charge and discharge, and V_{Heart}, the stimulation waveform.

The power consumption of each block was calculated during transient simulations by integration of the current leaving the 1.8 V power supply to obtain the average current, which is then multiplied by 1.8 V.

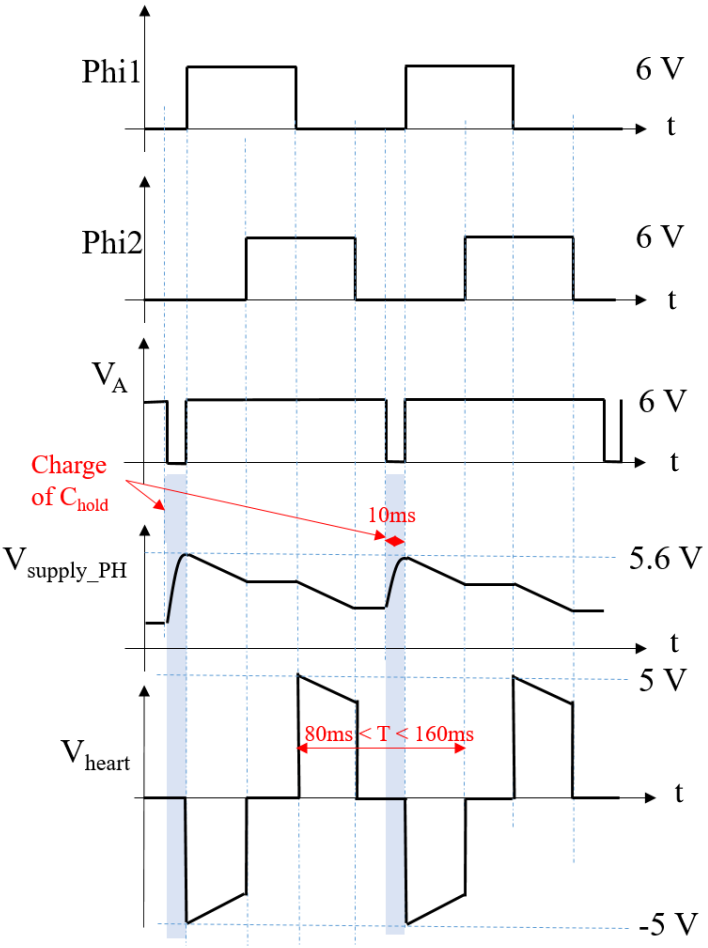

Figure 3.3: Waveforms of the stimulation circuit

We designed every block on Cadence Virtuoso using the XFAB 0.18 µm technology. The XH018 technology is a mature technology suitable for mixed analog/digital design up to several hundred megahertz for diverse applications (automotive, biomedical, etc.). This technology offers various types of transistors: isolated well transistors for independent well biasing and the resulting advantages, low-threshold voltage transistors for delivering more current, and high-voltage transistors suitable for a 3.3 V supply instead of 1.8 V. It also provides libraries of analog and digital components, as well as intellectual property (IP), meaning directly usable blocks, such as low power memories. This modularity and XFAB being certified ISO 13485 for medical devices [94] makes it a technology particularly well-suited for our application context.

Except for the pulse generator and voltage multiplier A, we opted to use Low-V_{th} neli and peli transistors, characterized by a lower threshold voltage (V_{th}) compared to conventional MOS transistors. This grants them a higher gain for an equivalent surface area, consequently reducing the circuit's size,

making them particularly appropriate for miniaturized low power applications. In addition, these are "isolated" transistors, which signifies that a special doping zone, known as a Deep N-Well, isolates them from the silicon substrate supporting the chip. This allows for individual biasing of their bulk regions at specific voltages. Both neli and peli have an absolute value of V_{th} of 0.35 V. For the pulse generator and multiplier A, we chose to use ne3i and pe3i transitors as they have to withstand the higher range voltages we want to apply to the heart. Their threshold voltages are V_{th_P} = - 0,65 V for PMOS transistors and V_{th_N} = 0,58 V for NMOS transistors.

Please note that all transistor sizes displayed in the figures are written as W[µm]/L[µm], with W being the width and L the length of the transistor. As pictured in Figure 3.4, bold transistors represent high-voltage ne3i/pe3i transistors while low-V_{th} neli/peli transistors are depicted with fine lines.

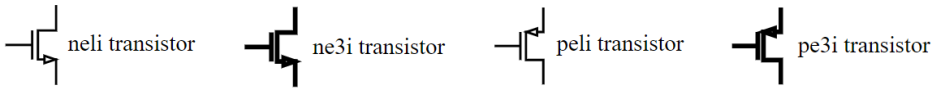

Figure 3.4: Transistor representation in the following figures

3.2 H-bridge

The generation of pulses is achieved by the charge and subsequent discharge of a capacitor. In order to generate the desired biphasic waveform, we opted for the classic structure of an H-bridge which is already employed for capacitor discharge in several defibrillators, as demonstrated in US Patent 2012/0123492 A1 [95]. The fundamental principle of the H-bridge relies on the control of four switching elements, here CMOS transistors. It has two parallel branches, each with two switches in series connected to the load (the heart) at midpoint by another branch (bridge), giving the circuit an "H" form, hence the name. The selection of the appropriate switch combination at specific time points defines the polarity of the voltage applied to the heart, providing the sequential negative (cathodal) and positive (anodal) phases as can be seen in phases 1 to 4 in Figure 3.5. This process allows for several configurations:

- Closing P1 and N4 results in direct current flow through the heart/ positive voltage applied across the heart.
- Closing P2 and N3 leads to current flow in the reverse direction.
- Closing either P1 and P2 or N3 and N4 (within the same horizontal row)

utilizes the current as an electromagnetic brake. This action helps maintain voltage at a specific level before it reaches zero potential difference.

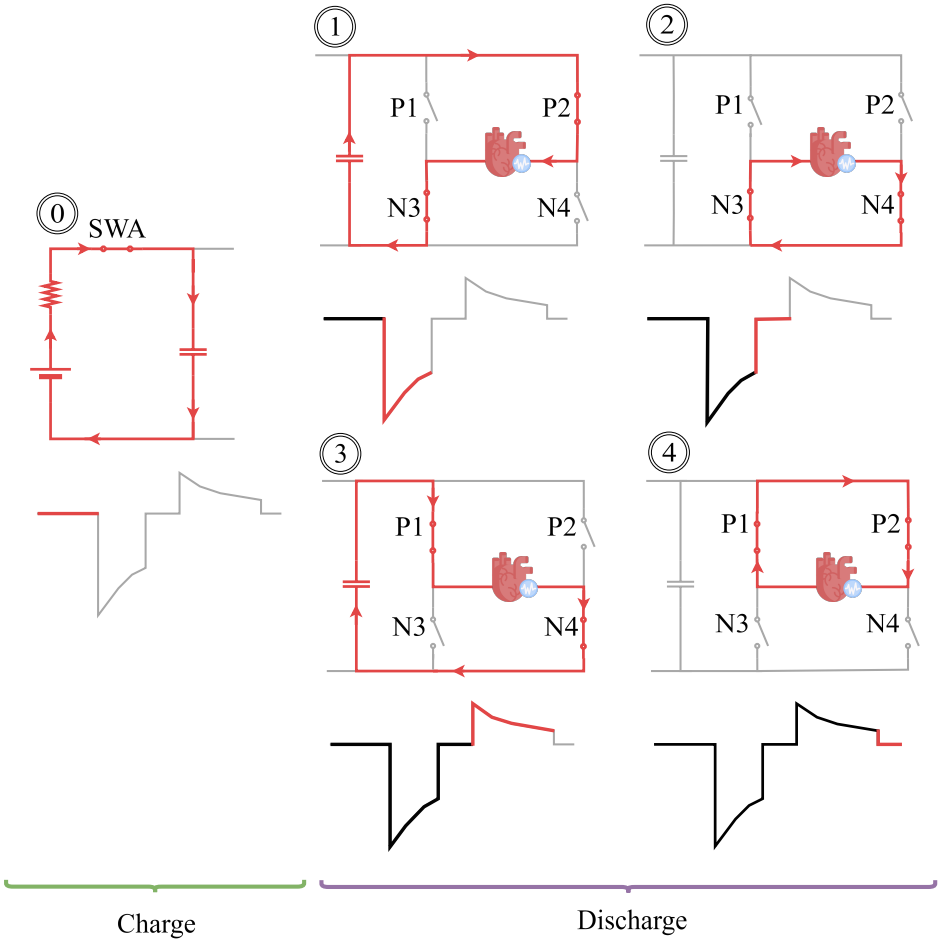

Figure 3.5: Charge and discharge phases of the pulse generator

It is imperative to prevent any potential short circuits, which can occur if P1 and N3 or P2 and N4 are closed simultaneously, or if all switches are closed at once. Such a scenario, called "shoot-through" would result in overheating, rapid battery discharge, and heavy damage to the circuit. Therefore, it is very important to strictly adhere to the switching times and moments of the switches and to include a non-overlapping circuit (Figure 3.7).

To obtain the exponential discharge form, we have added a capacitor prior to the H-bridge structure. The capacitor is connected to the voltage supply through a switch SWA and is either charged through the voltage supply or discharged into the heart according to the state of SWA. The overall process of impulse generation within our pacemaker can be illustrated as in Figure 3.5.

To attain a sufficient stimulation amplitude, we chose an external capacitance of 1 µF. A large capacitance also guarantees the absence of DC flow

within the heart tissues, thereby resulting in no residual charge [33]. The heart is modeled with a 133 kΩ resistance according to our prior results for the in vivo tests. For homogeneity of NMOS and PMOS switches, we seek that the on-resistance of PMOS transistors is equal to that of NMOS's with:

$$R_{on_N} \approx \frac{1}{K_N \frac{W_N}{L}(V_{GS} - V_{th_N})} \tag{3.1}$$

and

$$R_{on_P} \approx \frac{1}{K_P \frac{W_P}{L}(V_{GS} - |V_{th_P}|)} \tag{3.2}$$

Knowing
K_P = 70 µA/V², K_N = 270 µA/V², V_{th_P} = - 0,65 V, V_{th_N} = 0,58 V.

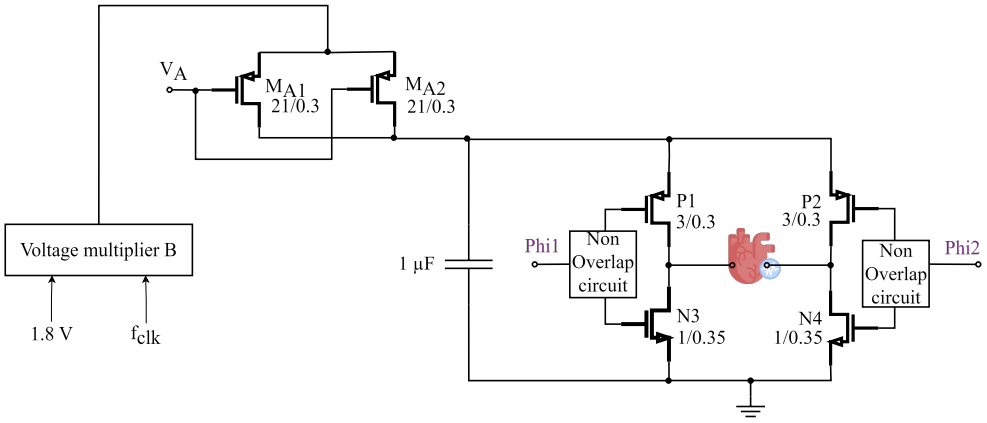

Figure 3.6: Schematic of the pulse generator

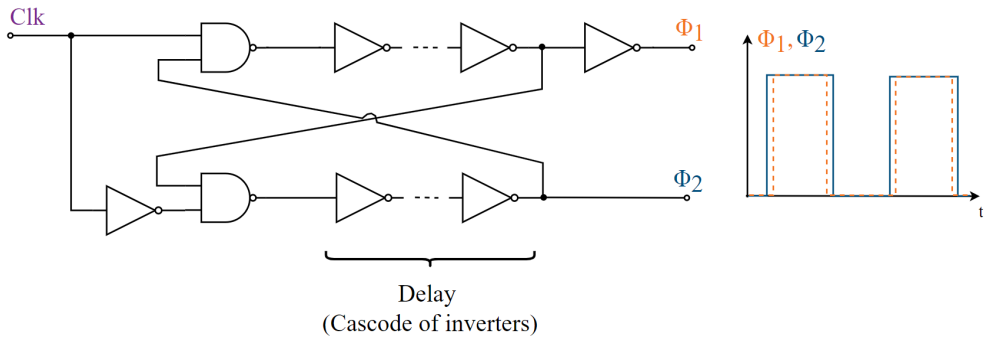

Figure 3.7: Block diagram of the non-overlapping circuit

The pe3i transistors must therefore be about four times larger than the ne3i. Moreover, it is easy to see that by maximizing the W/L ratio, i.e., the size of

the transistors, we can minimize the R_{on}. Accordingly, the gate lengths L of the transistors were kept to their minimum value of 0.3 µm (PMOS) and 0.35 µm (NMOS). With size of transistors as depicted on Figure 3.6, we have $R_{on_P} = 1.06$ kΩ and $R_{on_N} = 1.24$ kΩ which was sufficient for our application. Further reducing the R_{on} value by increasing W or introducing additional transistors would lead to a significant increase in the parasitic capacitance, which would be harder for the ULP commands to drive efficiently.

Switch SWA responsible for the charging of the capacitor was made of a pair of pe3i transistors of size 21 µm/0.35 µm, with an on-resistance amounting to 72.4 Ω.

The power consumption for the H-bridge, supplied by multiplier B, reaches 100 µW.

3.3 Ultra-low power, low frequency oscillator

The need to minimize power consumption in implantable medical devices, such as our pacemaker, calls for a low power operating system. Oscillators consume a non-negligible part of the overall battery life, and careful consideration must therefore be put in their design. When it comes to low power oscillators, three main architectures are typically considered.

Ring oscillators [96, 97, 98, 99] consist of an odd number of inverters arranged in a loop configuration. While they offer a smaller surface area and more power efficiency compared to crystal oscillators, their output frequency is very susceptible to PVT variations. Moreover, for applications targeting very low frequency operation, in the range of tens of Hz or below, ring oscillators may require either a very large number of stages [100], quite a few D-latches, or putting a bigger load capacitor between each stage [98], all resulting in larger area and high static power consumption. These oscillators also entail a trade-off between noise and power consumption, as the addition of more stages leads to better noise performance at the expense of higher power consumption [101].

Relaxation oscillators (ROSC) [102] are nonlinear circuits defined by a feedback loop involving switching devices that charge a capacitor or an inductance until it reaches a certain threshold voltage, at which point it discharges and the cycle repeats. For lower frequencies, these oscillators have the upper hand in both accuracy and surface area [103, 104, 105, 106, 107] compared to crystal or ring oscillators. This comes at the price of higher clock jitter but for low power applications, it is not a critical factor [108, 107]. While they can be influenced by temperature changes like ring oscillators, this shouldn't pose a significant issue for our circuit, considering it will be implanted inside the rat where temperature fluctuations are expected to be minimal.

Another structure often used in low power applications is Crystal oscillators (XOSC) [109, 110, 111]. They operate based on the inverse piezoelectric effect,

where an alternating voltage applied across the surfaces of a crystal with piezoelectric properties, commonly quartz, causes it to vibrate. This generates a highly stable electrical signal at a very precise frequency, even when subjected to changes in the manufacturing process, power supply, or temperature (PVT). As such, XOSC have a low phase noise and good selectivity, making them particularly well-suited for telecommunication or radio applications with frequencies ranging from a few kHz to hundreds of MHz. While recent developments have established the feasibility of low power nanoscale crystal oscillators [112, 113, 114], the benefits of XOSC are often outweighed by their larger off-chip size, still non-negligible current consumption (of the oscillator circuitry, the crystal itself does not consume much power), and higher costs, which makes them less suitable for low power miniaturized devices. Additionally, this type of oscillator is typically not tunable, limiting its adaptability for applications that necessitate variable or adjustable frequency outputs like ours.

In the context of our oscillator's application, we chose to settle on the second configuration, i.e. the relaxation oscillators, because of the possibility to reduce the power consumption to the minimum. The architecture of our ULP relaxation oscillator, based on [108], is depicted in Figure 3.8. It contains a reference generator, providing current sources I_{ref1} and I_{ref2}, along with threshold voltages $V_{compmax}$ and $V_{compmin}$. It also features a capacitor bank resulting in a total equivalent capacitance C_{tot}, two comparators, and an SR-latch using dynamic leakage suppression (DLS) logic.

3.3.1 Selected architecture

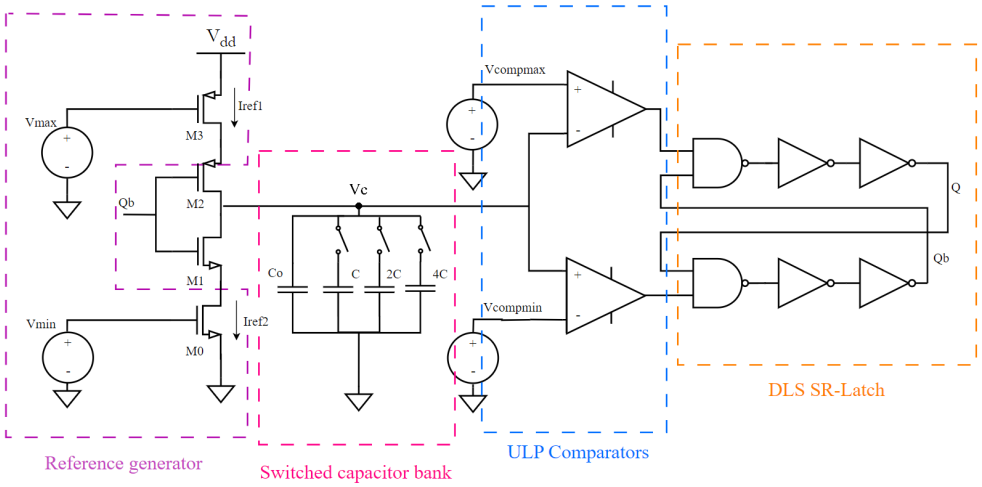

Figure 3.8: ULP relaxation oscillator architecture

The waveforms associated with the operating principle of our ROSC are illustrated in Figure 3.9 and its operation can be outlined as follows. Each

comparator compares the voltage Vc across the capacitor with either $V_{compmax}$ or $V_{compmin}$. The resulting output is fed to the SR-latch, which controls the transmission gates ensuing the charging or discharging of C_{tot}. If Vc exceeds $V_{compmax}$, the output of Comparator 1 goes low, causing Q to switch to a low state and Qb to a high state, leading to the discharge of the capacitor through I_{ref2}. Similarly, when $V_{compmin}$ exceeds the capacitor voltage, Q becomes high, Qb becomes low, and C_{tot} is charged through current source I_{ref1}. Hence, the capacitor alternates between charged and discharged states, generating the oscillations.

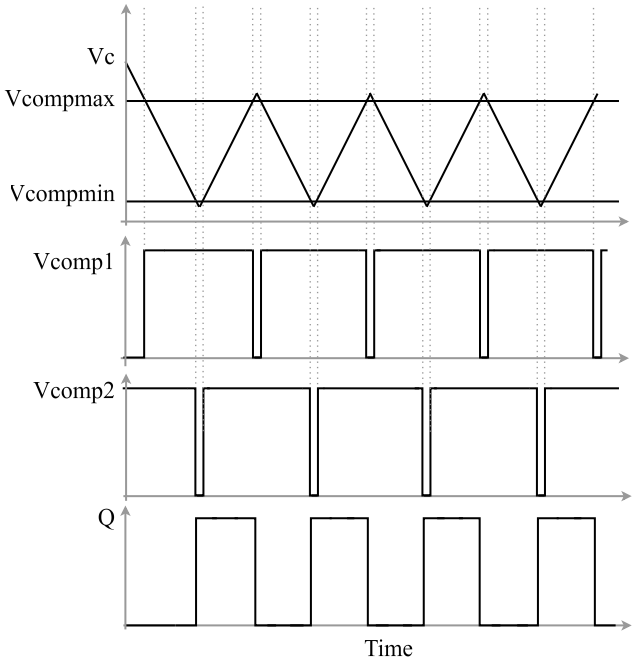

Figure 3.9: Relaxation oscillator waveforms

The oscillation frequency can be determined with :

$$f = \frac{1}{C_{tot}(V_{compmax} - V_{compmin})} \cdot \frac{1}{\frac{1}{I_{ref1}} + \frac{1}{I_{ref2}}} \tag{3.3}$$

And the duty cycle is given by :

$$\alpha = \frac{I_{ref1}}{I_{ref1} + I_{ref2}} \tag{3.4}$$

We can note that when $I_{ref1} = I_{ref2} = I_{ref}$, we obtain a 50 % duty cycle and 3.3 can be simplified to :

$$f = \frac{I_{ref}}{2C_{tot}(V_{compmax} - V_{compmin})} \tag{3.5}$$

Given that our work involves biological signals, our aim is to generate very low frequency oscillations, typically in the range of 10 to 20 Hz. We deliberately selected oscillations twice as fast as the targeted heart rate for our studies, ensuring the generation of appropriate control signals for the pulse generator (refer to Section 3.3.7). Based on Equation 3.3, this involves the utilization of subthreshold nanoscale currents, coupled with a load capacitor in the picofarad range.

The following subsections will present and detail the different blocks that make up our relaxation oscillator.

3.3.2 Charge pump current sources

M0 and M3 are voltage-controlled current sources. For nanoscale current supply, befitting our requirement, the transistors must operate in the subthreshold region where the current leakage can be expressed as [115]:

$$I_{DS,subth} = \mu C_{ox} \frac{W}{L} (\eta - 1)(U_T)^2 exp\left(\frac{V_{GS} - V_{th}}{\eta U_T}\right)\left(1 - exp\left(\frac{-V_{DS}}{U_T}\right)\right) \quad (3.6)$$

Where η is the subthreshold slope factor, Vth the threshold voltage of the transistor and $U_T = \frac{k.T}{q}$ is the thermal voltage.

In the subthreshold region, it is not uncommon to find transistors with a larger L than W. Should the duty cycle of the oscillator have been 50%, I_{Ref1} and I_{Ref2} would have been equal. However, as we want a slightly asymetrical signal to fit the pulse generator command, we introduced a mismatch between the two current sources. Transistors M3 and M0 displayed on Figure 3.8 are biased with Vmax = 1.6 V and Vmin = 200 mV. We thus have $I_{ref2} = 148.2$ pA and $I_{ref1} = 141.5$ pA, for sizes of 6 µm/20 µm and 1 µm/20 µm respectively.

3.3.3 Switched capacitor for variable frequency

The oscillation frequency equation (3.3) highlights three parameters that can be manipulated to adjust the frequency: the current sources, the difference between the threshold voltages, and the capacitor. However, we have seen with Equation 3.4 and Figure 3.9 that the first two parameters also exert a significant influence on the duty cycle. Hence, to achieve frequency adjustments without affecting the duty cycle, we have chosen an approach that focuses on capacitors.

The frequency modulation relies on an array of parallel switched binary weighted capacitors, in addition to a base capacitor C0, where the capacitors within the array have values that are proportional to powers of 2. For example, in our case we chose to have a "3-bit" array, in which we have capacitors with values of 1C, 2C, and 4C, where C stands for the capacitance value.

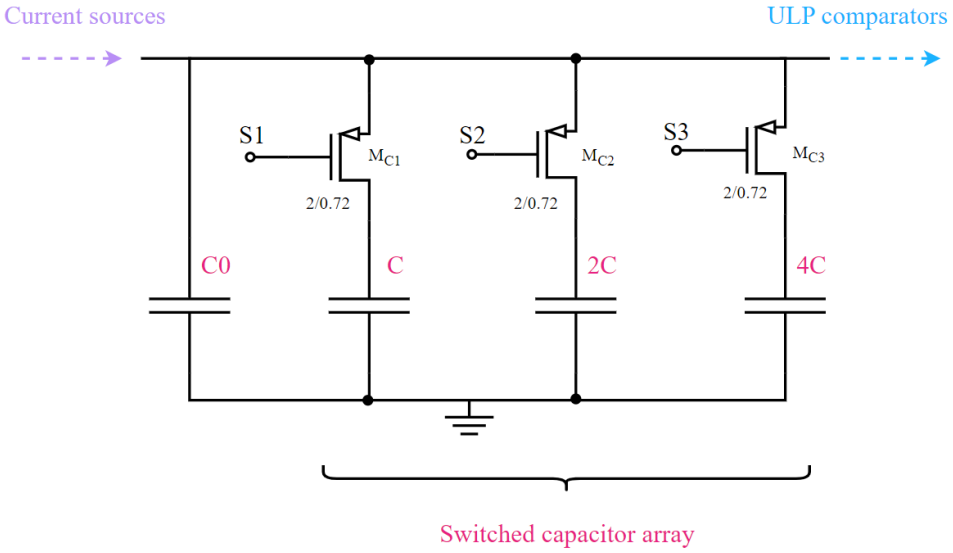

Figure 3.10: Switched capacitor circuit

This configuration, shown in Figure 3.10 allows for a wide range of possibilities with a relatively small number of capacitors. Indeed, with 3 capacitors, we have $2^3 = 8$ possible combinations, which means 8 different frequencies available. Each capacitor, except for C0, are linked to a voltage-controlled switch. An external voltage source, here called S1, S2 or S3, and equal to either 0 V or Vdd, is applied at the gate of each switch to determine if the associated capacitor is selected or not. The equivalent capacitance will then be the sum of C0 and the selected ones, since they are in parallel.

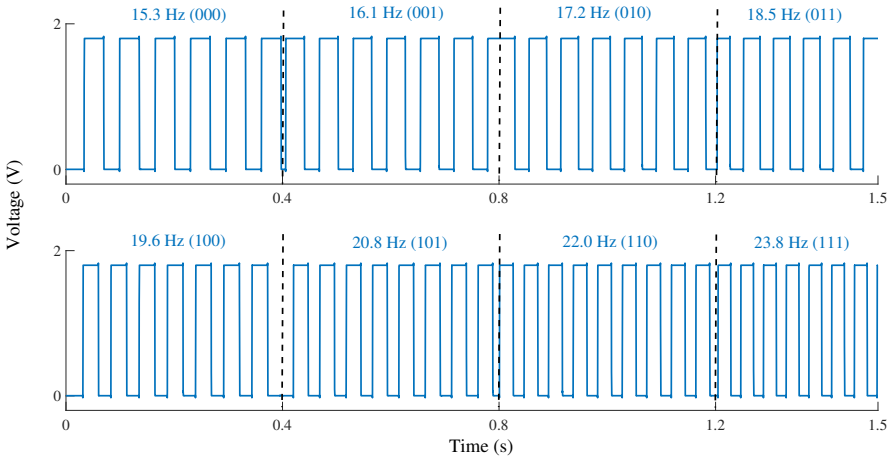

Figure 3.11: Simulated ROSC waveforms for different frequencies with their capacitance combination (S3S2S1)

Thereby, the maximum possible value is determined by

$$C_{totmax} = C0 + 7C \tag{3.7}$$

and C0 is the minimum value.

With C0 = 3,8 pF and C = 330 fF, we can attain with the proposed oscillator frequencies within the targeted range, typically falling between 15.3 and 23.8 Hz. Figure 3.11 illustrates the diverse frequencies achievable for each capacitor value, with the respective switch combinations provided in parentheses. The dimensions of each switch are 2 µm/0.72 µm to have satisfying R_{on} values while keeping a reasonable size.

3.3.4 Dynamic Leakage Suppression logic gates

One of the key challenges in ULP applications lies in managing power consumption efficiently. As the trend of technology scaling leads to the development of nanoscale MOSFETs [116], the primary concern of power dissipation shifts from dynamic power to static power stemming from current leakage. This transition has prompted the exploration of innovative leakage mitigation techniques including transistor stacking and reverse body biasing among others [117, 118]. Both methods' circuits are represented for an inverter gate in Figure 3.12.

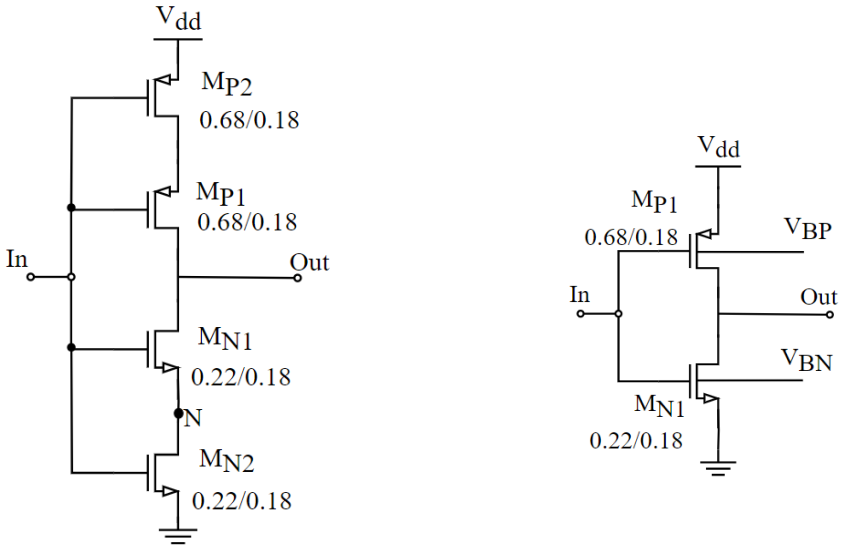

(a) Transistor stacking

(b) Reverse bodybiasing

Figure 3.12: Leakage current mitigation techniques

Transistor stacking, refers to a technique where a transistor is replaced by two or more transistors in series (stacked) [118, 119]. This approach, also called 2T-stacking in the case of a pair of transistors, had first been proposed in the context of SRAM memories to minimize leakage current during standby

mode. When the transistors in series are switched OFF, the intermediate node N settles to positive voltage due to a small drain current, which leads to:

- The gate-source voltage V_{GS1} becoming negative,
- The bulk to source voltage V_{BS1} becoming negative, resulting in an increase in the threshold voltage of M_{N1},
- The drain-source voltage V_{DS1} decreasing significantly.

In submicron/nanoscale transistors, two short channel effects, namely the Drain Induced Barrier Lowering (DIBL), referring to the reduction of the threshold voltage with the increase of the drain voltage, and the body effect, where the threshold voltage increases as the source-bulk voltage increases, are especially prominent in the subthreshold region. Taking these effect into consideration, equation 3.6 can be revised to the following [118] :

$$I_{DS,subth} = I_0 exp\left(\frac{V_{GS} - V_{th0} + \lambda V_{DS} + \gamma V_{BS}}{\eta U_T}\right)\left(1 - exp\left(\frac{-V_{DS}}{U_T}\right)\right) \quad (3.8)$$

With $I_0 = \mu C_{ox}\frac{W}{L}(\eta - 1)(U_T)^2$, λ the DIBL coefficient and γ the body effect coefficient. Therefore, one can see that the leakage current is reduced exponentially [120, 121]. This is what we call the "stacking effect". In concrete terms, with the XFAB CMOS 0.18 µm technology with transistor sizes as indicated in Figure 3.12a, it corresponds to a reduction of current leakage from 122.9 pA in the standard case to 27.9 pA in the 2T-stacking case. The leakage current could be reduced even further by adding a higher number of transistors, but this means we would have a larger circuit surface and a bigger parasitic capacitance (resulting in even more delay).

Most often, we tend to interconnect the source and bulk terminals in CMOS devices. However, leveraging the difference between these two voltages enables the adjustment of the voltage threshold, a phenomenon known as the body effect [122, 118]. The relationship between the threshold voltage and the source-to-bulk voltage can be expressed as:

$$V_{th} = V_{t0} + \gamma(\sqrt{V_{sb} + |2\Phi_F|} - \sqrt{|2\Phi_F|}) \quad (3.9)$$

With V_{t0} the threshold voltage at zero source-to-body voltage, γ the body-effect factor, Φ_F the Fermi potential, and V_{sb} the voltage between the source and substrate [123].

Consequently, as V_{sb} increases (or V_{bs} becomes more negative), the threshold voltage increases, effectively diminishing the leakage current [118, 117, 124]. This method is known as reversed body biasing (RBB) (Figure 3.12b). In practice, employing reverse body biasing equates to a reduction in current leakage to 6.2 pA with V_{BP} = 1.5Vdd and V_{BN} = -0.5Vdd. This approach, however, requires a triple-well technology to bias both PMOS and NMOS transistors as

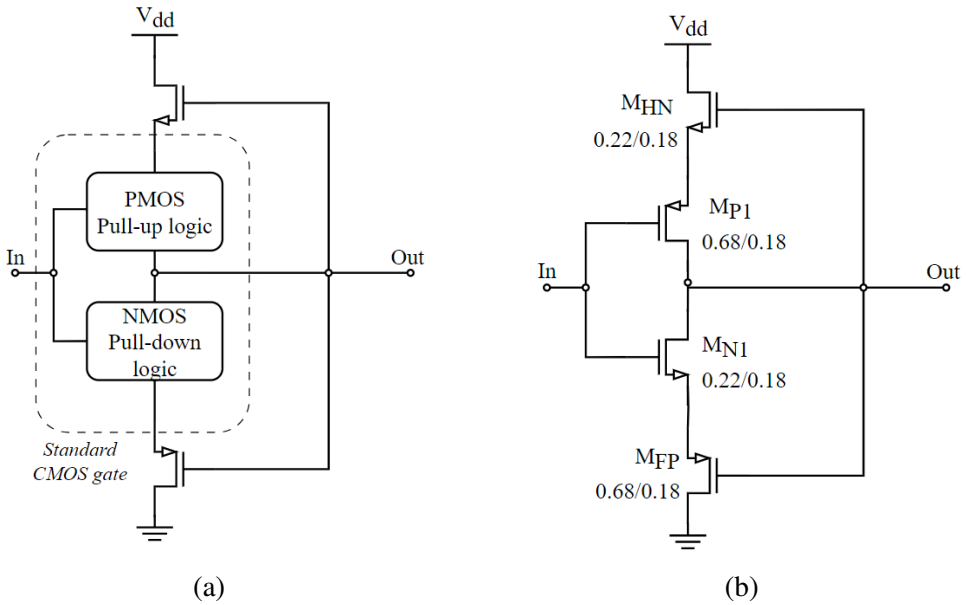

Figure 3.13: (a) DLS principle, (b) DLS inverter gate

well as a bias generation circuit for each bias, making the fabrication process more complex and thus a lot more expensive. Moreover, the extent of threshold control achievable through dynamic biasing is limited [118, 125, 117, 126].

In addition to these, dynamic leakage suppression (DLS) logic, sometimes dubbed ultra-low power logic, has emerged as a promising approach [116, 127, 128]. With this method, we have designed two logic gates, an inverter and a NAND gate, which will be key components in multiple blocks within our oscillator and in generating command signals for the H-bridge.

The concept of DLS gates is based on standard CMOS gates, that consist of a pull-up network (PUN) and a pull-down network (PDN), enhanced by incorporating two transistors, a header NMOS (M_{HN}) and a footer PMOS (M_{FP}). The gates of these additional devices are connected to the output node, resulting in a feedback loop that drives all the leaking devices in a super-cut-off state (Figure 3.13a). In order to better comprehend the operating principle of DLS logic, let us consider the DC characteristics of the DLS inverter presented in Figure 3.13b. When the input is low, the leakage current is derived from the pull-down logic. The gate of MFP being looped to the high state output voltage, the intermediate voltage between MN1 and MFP stabilizes around half the output voltage. This results in both transistors operating with negative Vgs (Vsg), thus entering the super-cut-off state. Similarly, when the input equals VDD, the pull-up network is driven to super-cut-off.

In the inverter, the size of the NMOS transistors is kept to the minimum (0.22 µm/0.18 µm) while the width of the PMOS devices is 3 times larger (0.68 µm/0.18 µm) to compensate for the difference between NMOS and PMOS

carrier mobility and keep comparable rising and falling times for the output. Here, the bulk of each transistor is connected to its source. The leakage current using this method drops to 1.79 pA, more than 60 times lower than for a standard gate.

The super-cut-off feedback loop in DLS logic gives rise to a hysteresis behaviour in the voltage transfer curve, illustrated on Figure 3.14 with distinct rising and falling switching points close to Vdd and ground. This results in a higher static noise margin compared to a standard inverter gate as reported by [129, 130], but it also makes the DLS gates especially stringent with regard to input signals, requiring very clean levels of 0 and 1.8 V.

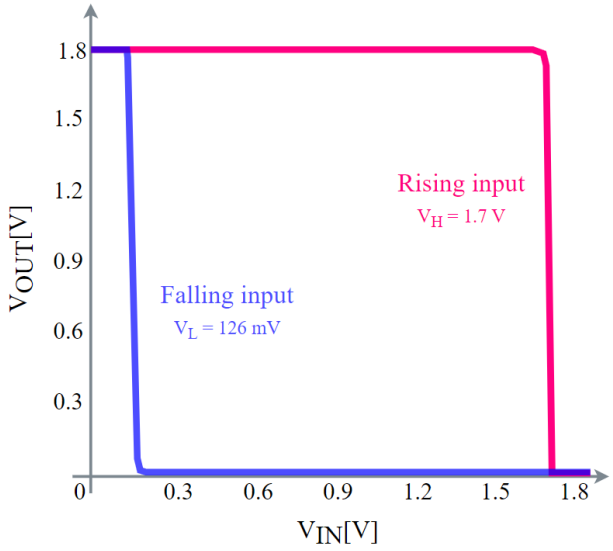

Figure 3.14: DLS inverter voltage transfer curve

The behaviour of the DLS inverter gate was assessed through five different scenarios: the typical case (tm) - where the values are nominal - and four other corners, corresponding to extreme circumstances in manufacturing process variation. They are defined as follows:

- Worst Speed (ws): Transistors are slower than in the typical case and consume little power.
- Worst Power (wp): Transistors are faster than in the typical case and consume a lot of power.
- Worst Ones (wo): PMOS transistors are slow, and NMOS transistors are fast.
- Worst Zeros (wz): PMOS transistors are fast, and NMOS transistors are slow.

The latter two cases are considered the most problematic as the imbalance in the switching speed between both types of MOS can lead to their bias points being too shifted in analog circuits, potentially rendering the circuit inoperable. In the case of logic gates, this imbalance is translated into highly disparate rising and falling times. Note that NMOS or PMOS transistors are considered slow (fast) when their threshold voltage V_{th} is higher (lower) than expected. Electronic blocks are formed by stacking successive layers creating parasitic capacitances. To operate a circuit, voltage variations need to be applied to the input of these blocks. Considering the capacitor charging formula: $I = C.\frac{DV}{DT}$, we get $DT = C.\frac{DV}{I}$. Hence, to be able to reach a certain DV in a certain DT, a larger current I is required (as the parasitic capacitance, inherent to the block structure, cannot be modified). This is why circuits that consume more are also faster and, conversely, those that are slower consume less.

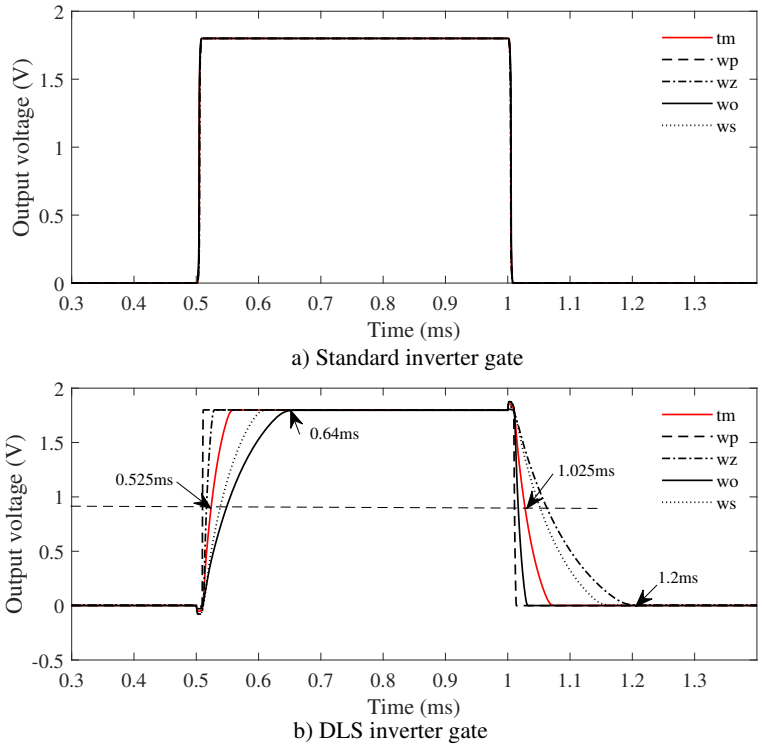

Figure 3.15: Inverter gate worst case analysis waveforms

Figure 3.15 depicts curves of a standard inverter gate with minimal-sized transistors in the typical case, and of the DLS inverter gate obtained for the five cases, all at 1 kHz. We only reported the standard inverter in the typical case because it is very robust at this frequency, and therefore all curves had the same shape. However, we can observe that at this frequency the DLS gate is highly sensitive, and the curves explicitly represent their respective worst

cases.

But first, let's mention that the transition times of the DLS gate in the typical case are slower than those of the simple gate since there is less current. In the Worst Power case, more current is drained, resulting in faster transitions than in the typical case, giving the curve a similar appearance to that of a normal inverter, at the expense of consumption, which rises to 4.7 pA compared to 4 pA in the typical case. However, this remains much lower than a standard inverter gate consuming 122.9 pA in tm. In the Worst Speed case, the rise and fall times are indeed longer, but the power consumption is reduced to 3.96 pA. Finally, for wo (wz), we observe a fast (slow) rise time and a slow (fast) fall time due to the PMOS and NMOS not having the same speed.

Consequently, when increasing the frequency, especially above 1 kHz, the low power DLS approach is not viable because the currents are not sufficient to drive the capacitances. Alternative low power approaches presented earlier, such as stacked inverters, which can handle higher frequencies, are required.

Nevertheless, for all logic blocks operating at a frequency lower than, for example, 100 Hz, the DLS logic will be favored because the impact of rise/fall time even in the worst cases is very negligible.

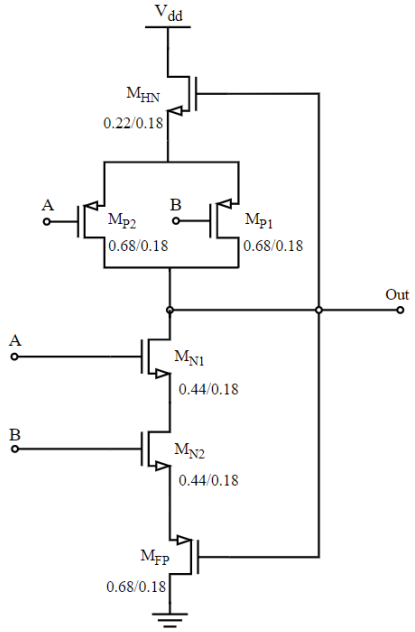

(a)

A	B	Out
0	0	1
0	1	1
1	0	1
1	1	0

(b)

Figure 3.16: (a) DLS NAND gate, (b)Truth table for a two inputs NAND gate

The dimensions of the NAND gate have been designed in accordance with those of the inverter's in order to maintain equivalent delay times. In the PUN, both PMOS transistors are sized the same as in the inverter given that there is only one parallel combination of devices between Vdd and the output. On

the other hand, for the PDN, as the two NMOS are in series, the on-resistance would be doubled. To compensate for this, each NMOS transistor of the NAND gate must have a (W/L) ratio twice as large as that of the inverter's NMOS [131]. PMOS and NMOS gates of the PUN and PDN thus have respective sizes of (0.68 µm/0.18 µm) and (0.44 µm/0.18 µm). The diagram and truth table of the NAND gate can be found in Figure 3.16.

3.3.5 ULP Comparator

Principle and dimensioning of the proposed comparator

The main requirements for the comparator in the relaxation oscillators are the following:

- The power budget should be reduced to the minimum, which is why we propose the use of DLS inverters as described in what follows.
- As much as possible, the transistors should work in subthreshold.
- As much as possible, the references used for the comparison should be the ones already available in the circuit, i.e. 200 mV and 1.6 V.

Other performances like sensitivity and offset are secondary for this comparator. This is why, contrary to previously published work [107] where a classical OTA has been proposed, we propose the circuits presented in Figures 3.17 and 3.18. The first stage is composed of two common source circuits loaded by a current mirror, all working in the subthreshold region. Let's consider Figure 3.17 to explain the principle. The first common source (transistor M5) has its gate connected to the static reference V_{refN} (200 mV), leading to a bias current of I_0 (580 pA) in this branch. The second common source created by M6 has its gate connected to the same static reference V_{refN} plus a dynamic input v. It creates a current $I_0 + g_m$v with g_m the transconductance of M6. Because V_{refN} is well below V_{thN} (0.45 V) it places all transistors of the first stage in the subthreshold region. Due to the current mirror (M7-M8) we have an output current which is only the dynamic current g_mv going into the output impedance of the first stage. And because all transistors are in subthreshold and VDS $>$ 0.1 V according to [132, 133], the term in VDS in expression 3.6 can be neglected, leading to a very high output impedance for this first stage. In simulation, the output impedance has been measured always greater than 10 GΩ. Consequently, the voltage $vout_{1N}$ which is equal to g_mv.R_{out} is either greater than 1.7 V or lower than 126 mV guaranteeing a good functioning for the DLS inverter (according to Figure 3.14).

The transistors were dimensioned as displayed in Figures 3.17 and 3.18 and several rules were taken into consideration for optimal sizing [115, 134]:

- Transistor sizes are maximized to avoid mismatches, which are particularly critical in weak inversion. This comes at the expense of a reduced bandwidth which is fortunately not an issue below 100 Hz.

- To ensure that the bias point is in the appropriate region in subthreshold, a larger length than width is essential. Consequently, M7 and M8 have dimensions of 0.22 µm/ 10 µm.

- At low frequency, we are sensitive to flicker noise, which is inversely proportional to WL [122]. The transistors thus need to have a very large surface to minimize it by being after the corner frequency.

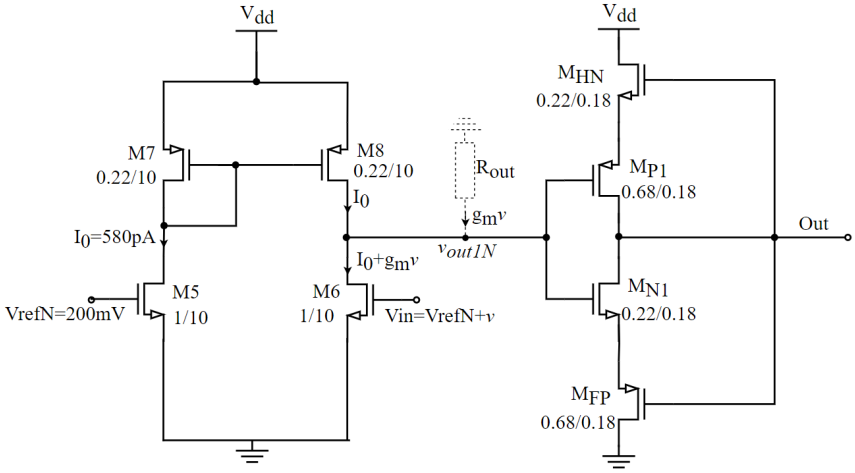

Figure 3.17: ULP NMOS comparator

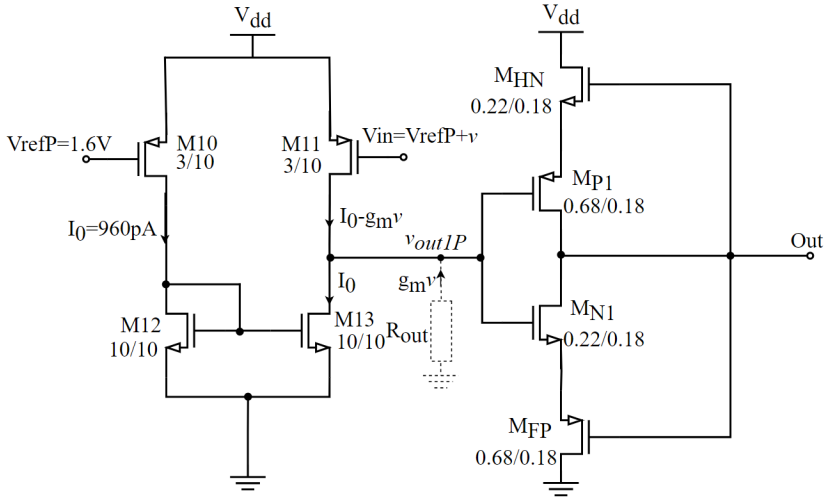

Figure 3.18: ULP PMOS comparator

Performances

The performances of sensitivity, offset and power consumption have been evaluated thanks to a DC sweep simulation as recommended in [96] in typical case and worse cases. The sensitivity, i.e. the minimum difference leading to a change of state at the output comes from the first stage. It is calculated as VDD/A, with A the gain of the first stage. Figure 3.19, resulting from a DC sweep simulation, shows the maximum A obtained for both NMOS and PMOS comparators. Figure 3.20 presents the transient simulation results for typical and worst cases for both comparators when the input is a 10 Hz sine of 50 mV amplitude, which is comparable to practical cases in the relaxation oscillator. All performances are summarized in Table 3.1 and 3.2. As for the offset, there is the one coming from the first stage, and the global offset. Despite its poor sensitivity and offset performances compared to the state-of-the-art [135, 136], the two comparators allow for a drastic reduction in power consumption while offering a satisfying operating behavior. Here, the power consumption was calculated considering the static current.

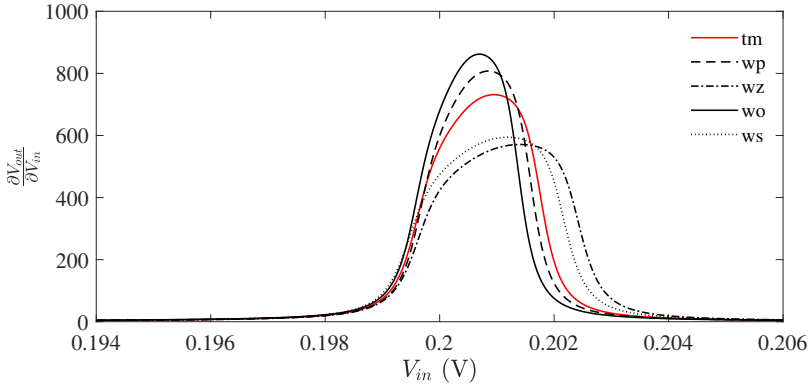

a) NMOS comparator

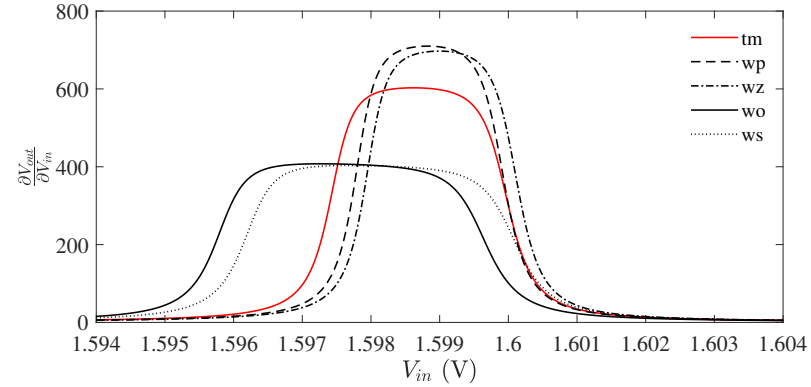

b) PMOS comparator

Figure 3.19: DC sweep simulation : $\frac{dV_{out}}{dV_{in}}$

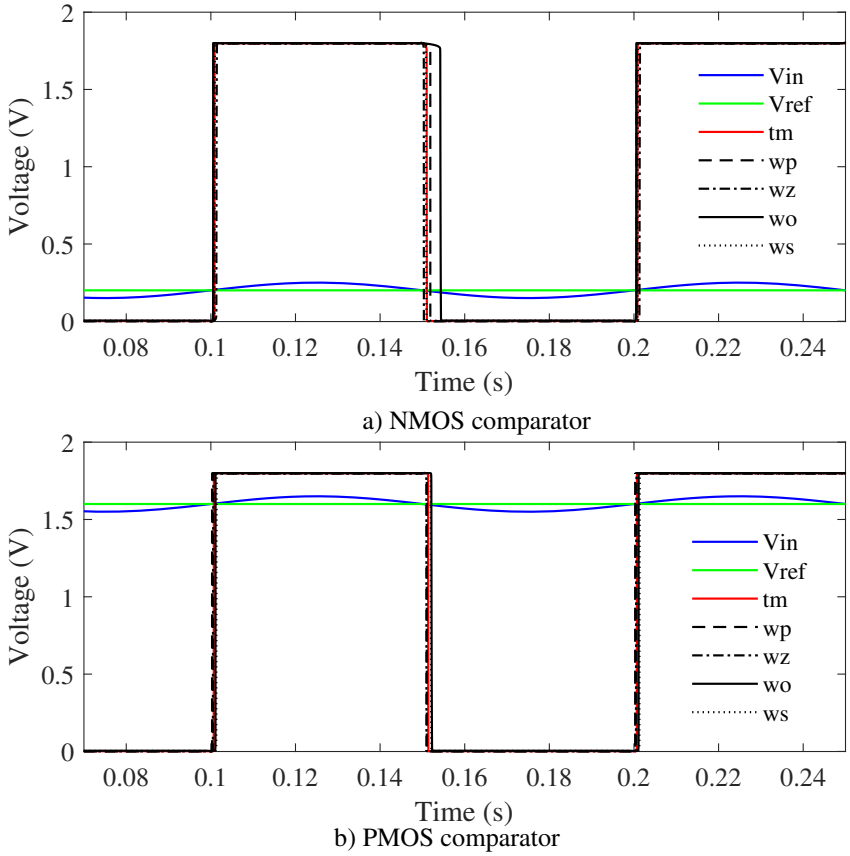

Figure 3.20: Transient simulation results

Comparator for reshaping the H-Bridge commands

In order to control the H-Bridge effectively, it is essential to convert the command voltage range from [0-1.8] V to [0-6] V. This transformation is achieved using the NMOS comparator. As such, adjustments have been made to the transistor sizes, reducing them to be driven by the small power logic.

	Bias current (I_0)	**1^{st} st. offset**	**1^{st} st. sensitivity**	**Total offset**	**Static Power consumption**
tm	580 pA	980 µV	2.5 mV	1.7 mV	1.04 nW
wp	1.38 nA	880 µV	2.2 mV	1.3 mV	2.48 nW
ws	235 pA	1.2 mV	3 mV	1.8 mV	423 pW
wo	1.4 nA	690 µV	2.1 mV	1 mV	2.52 nW
wz	227 pA	1.44 mV	3.2 mV	2.9 mV	409 pW

Table 3.1: NMOS comparator perfomances

	Bias current (I_0)	1^{st} st. offset	1^{st} st. sensitivity	Total offset	Static Power consumption
tm	227 pA	-1.5 mV	3 mV	320 µV	408 pW
wp	577 pA	-1.1 mV	2.5 mV	70 µV	1.04 nW
ws	83 pA	-2.2 mV	4.4 mV	220 µV	149 pW
wo	82 pA	-2.5 mV	4.4 mV	500 µV	147 pW
wz	2.49 nA	-0.9 mV	2.6 mV	1.35 mV	9 nW

Table 3.2: PMOS comparator perfomances

3.3.6 Worst case analysis of the proposed ROSC

In the study of the proposed ROSC architecture, we conducted a process corner analysis of the whole circuit, again considering five cases: typical, worst power, worst speed, worst ones and worst zeroes. Figure 3.21 portrays the resulting waveforms for an oscillation frequency of 15.3 Hz.

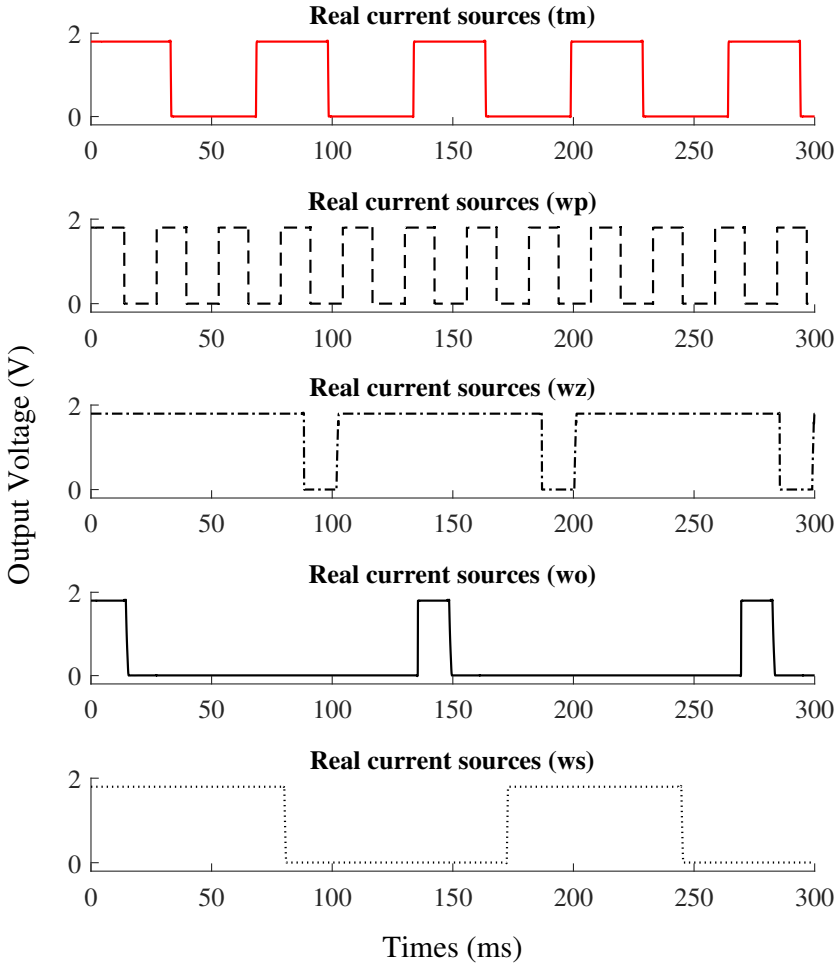

Figure 3.21: ROSC worst case analysis waveforms

The output demonstrates significant variation depending on the case. We suspected the current sources to be the main issue as they are built using a simple transistor. Moreover, the waveforms are good illustrations of the influence of the current on the duty cycle and the frequency of the oscillator as we have seen previously with equations 3.4 and 3.3: a higher (slower) frequency for wp (ws) with a duty cycle similar to that of tm, and a less balanced duty cycle and a lower frequency for both wo and wz.

To investigate whether the circuit's sensitivity stemmed solely from the current sources, we conducted a corner analysis using ideal current sources and sinks. The corresponding waveforms are depicted in Figure 3.22.

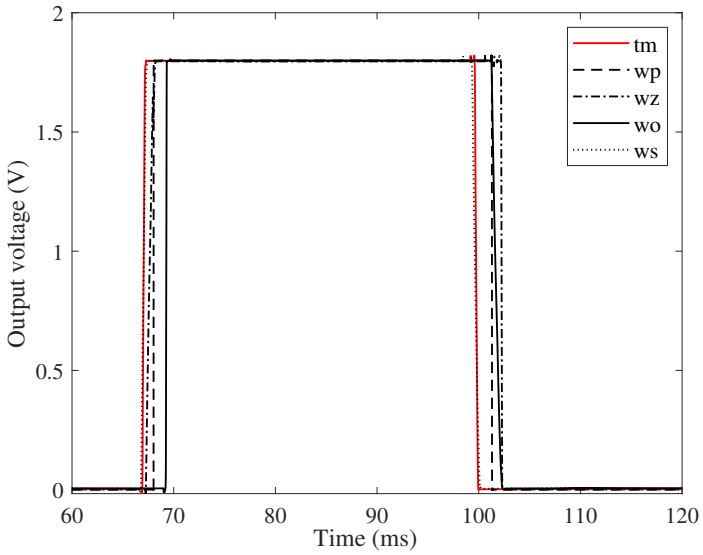

Figure 3.22: ROSC worst case analysis waveforms with ideal current sources

A slight delay can be observed at the start of the different cases, which accumulates over the following periods, causing a progressive shift between the two waveforms. Nonetheless the frequency and duty cycle of the oscillation remain consistent across the cases.

Consequently, careful consideration should be put into the design of robust current sources in further work to achieve a reliable relaxation oscillator circuit for the system. For instance, in [28] Wong et al. briefly presented self-adjusted current sources using large transistors as "constant leakage generators" in addition to a leakage cancellation feedback, while [108] based his work on Hirose et al.'s current generation method [132] to design temperature compensated nanoscale current reference circuits. Another example is [133] where the circuit of a curvature compensated current reference composed of two Complementary to Absolute Temperature (CTAT) and a Proportional to Absolute Temperature (PTAT) current generators is detailed.

3.3.7 Control waveform generation

The control signals for the H-bridge, as illustrated in Figure 3.3, rely on two low frequency signals, namely Phi1' and Phi2', with one shifted by half a period. To derive these signals from our relaxation oscillator, we used an XOR gate.

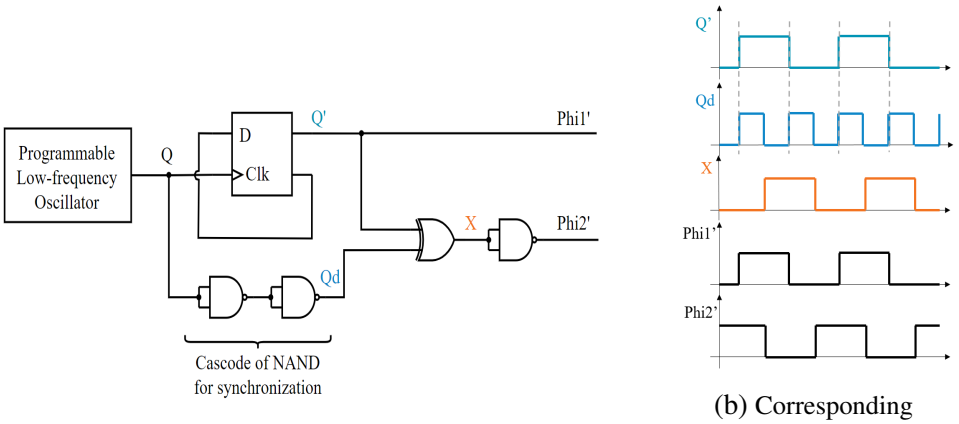

(a) Block diagram of the control waveform generator

(b) Corresponding waveforms

Figure 3.23: Control waveform generation

The XOR gate takes as input Qd, the oscillator's output, and Q', the output with a frequency divided by 2. As such, we need oscillation frequencies twice as fast as the ones targeted for the stimulation. For resynchronization purposes, we added cascades of NAND gates used as inverters. We opted for NAND gates as they are slightly slower, allowing for a reduction in the number of components in the cascade. All the logic gates, including the XOR gate, and the frequency divider use DLS components to limit the power consumption. The block diagram of the entire control circuit, the corresponding waveforms, along with diagrams of components constructed from DLS gates are depicted in Figures 3.23 and 3.24.

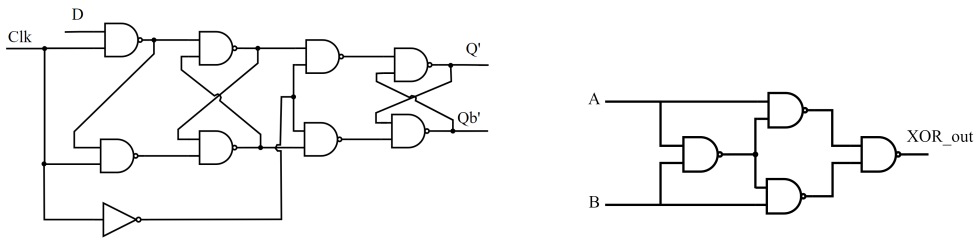

(a) D-Latch

(b) XOR gate

Figure 3.24: Implementation of components using DLS gates

Control signal VA' for switch SWA is obtained with a NAND gate using Phi1', delayed and inverted, as shown in Figure 3.25. All three signals VA',

Phi1' and Phi2' then pass through a comparator to provide the command VA, Phi1 and Phi2 with appropriate amplitude for the high voltage pulse generator. Notably, Phi1 and Phi2 present a 90° phase shift, and VA, which is synchronized with Phi1, remains in a low state for a brief period (∼10 ms) for the PMOS switch to be on, charging the hold capacitor C_{hold}.

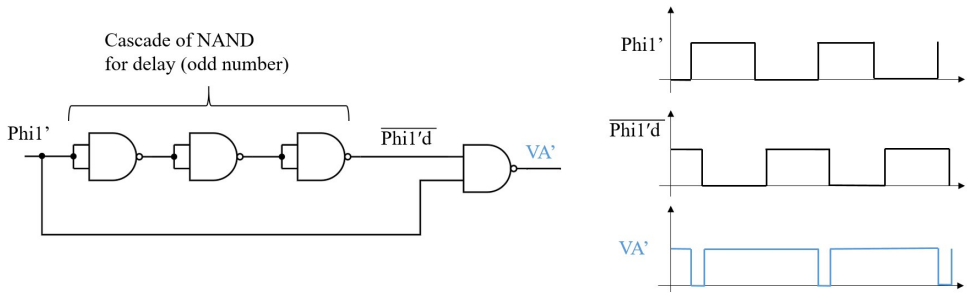

Figure 3.25: VA control circuit diagram and waveform

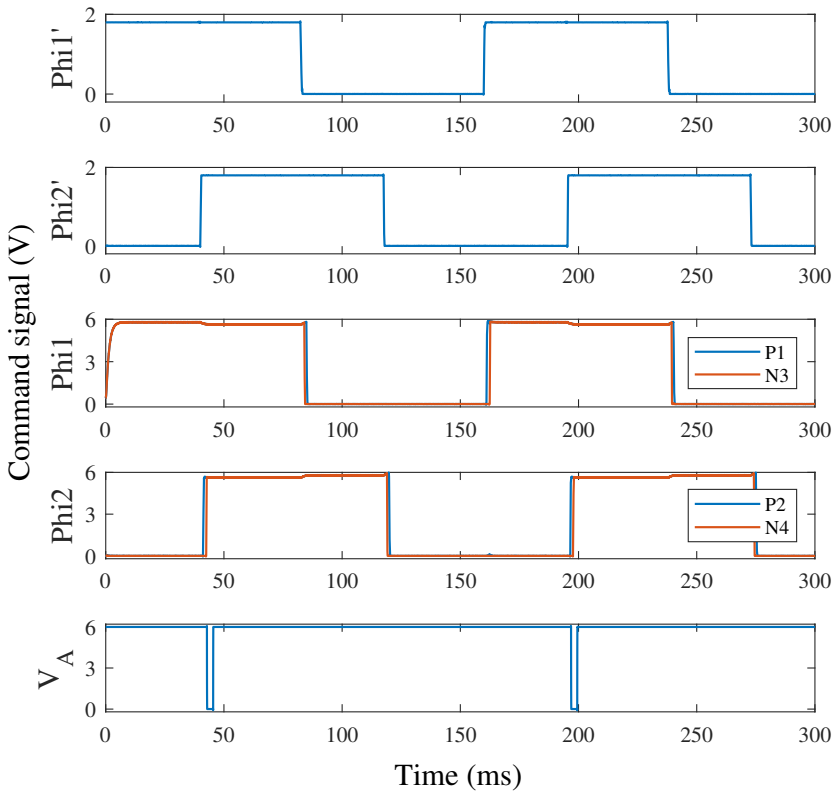

Figure 3.26: Simulated command signals for the H-bridge

Figure 3.26 shows the waveforms issued from the command generator circuit. It displays Phi1' and Phi2', as well as their non-overlapping high-voltage counterparts Phi1 for switches P1 and N3, and Phi2 for switches P2 and N4 of the H-bridge. The high voltage command V_A for switch SWA is also represented. The worst case analysis for command signal Phi1, considering ideal current sources in the relaxation oscillator, is depicted on Figure 3.27.

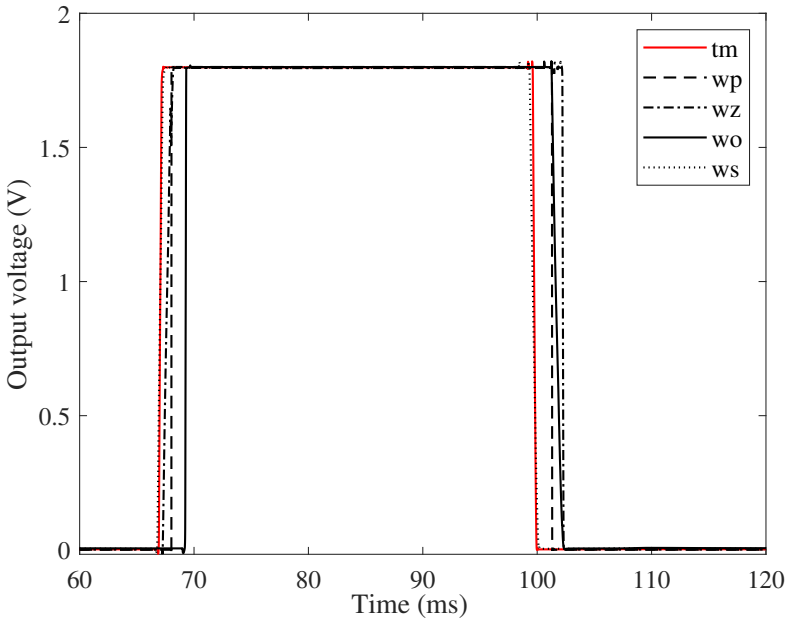

Figure 3.27: Phi1' worst case analysis waveforms with ideal current sources

The power consumption for the ROSC and control waveform circuit, estimated from a transient simulation, is 1.8 µW.

3.4 Conclusion

In this chapter we detailed the different components of our integrated circuit dedicated to providing a stimulation waveform for cardiac pacing in rats.

Supplied with 1.8 V, the circuit relies on an H-bridge commanded by signals stemming from a programmable ultra-low power, low frequency relaxation oscillator. This oscillator operates at variable frequencies between 15.3 and 23.8 Hz, about twice the pace of the cardiac frequencies aimed in our research, as required to generate the proper commands. The oscillator's design is optimized for minimal power consumption, employing DLS logic components, an ULP comparator, and current sources in the subthreshold region. Both the DLS logic blocks and the proposed comparator exhibit high robustness and very low power consumption within the frequency range of our application. This feature

enables the proposed ROSC to maintain robustness against process variation, provided further research and revisions are engaged in the conception of the current references. Furthermore, an interface has been introduced between the relaxation oscillator and the H-bridge to address any potential supply mismatch concerns, while non-overlapping blocks have been incorporated to prevent shoot-through occurrences in the stimulation associated with the H-bridge commands.

The overall power consumption for the command signals generation totals 1.8 µW, and 100 µW for the H-bridge, allowing most of the current to be directed toward the heart.

With the comprehensive review of these block's design and analysis completed, the subsequent chapter will focus on the function of the voltage multiplier with the 15 kHz VCO, before presenting and analyzing the simulation results and analysis of the entire circuit.

Chapter 4

Global simulation results and Discussion

4.1 Introduction

In the previous chapter, we outlined the various components comprising the proposed stimulation circuit presented in Figure 3.1 and conducted an in-depth evaluation of their individual performance. This chapter is dedicated to presenting the simulation results obtained for the circuit as a whole after describing the behaviour and performance of VCO-driven voltage multipliers block. Furthermore, we will delve into analogous pacing circuits documented in the literature, with a similar or comparable objective. This comparative analysis will allow us to discern and appraise the strengths and weaknesses of our circuit within the context of existing alternatives.

4.2 Voltage multipliers and control oscillator

In Chapter 2, we established that we need at least 30 µA to induce pacing and that a 133 kΩ resistance is a suitable model for the pacing load. Applying Ohm's law, it follows that a minimum stimulation amplitude of 4 V would be necessary to ensure effective stimulation. Unfortunately, the low voltage supply of 1.8 V is not sufficient to provide such amplitude as it is.

Level shifters are a recurrent and attractive option when considering higher voltage supply in low power circuits [137, 138]. However their principle centers on translating signals from one voltage level to another, in systems with multiple supply voltages, to ensure the compatibility among different blocks of a system. Consequently, they require the presence of an already existing higher voltage supply in the circuit, which diverges from the essence of our requirements.

As a result, we chose to rely on the use of a cascade of two voltage multipliers (Figure 4.1) to meet our specific needs, as detailed in what follows :

- One multiplier (A) will create the appropriate 6 V DC voltage for the command signals of the H-bridge as well as for the second multiplier which works with high voltage commands. In this case, a capacitive load in the order of magnitude of 100 pF suffices to maintain the 6 V while supplying all the low power digital gates. Additionally, this first multiplier should be able to operate efficiently with 1.8 V commands.
- The other multiplier (B), supplying the H-bridge, must have a capacitive load of 1 µF to achieve the desired waveform during the capacitance discharge through the H-bridge as stated in Section 3.2. It must also have a very short rising time (∼10 ms according to VA's pulse duration) to be able to reach about 6 V before each stimulation instance, as shown in Figure 3.3.

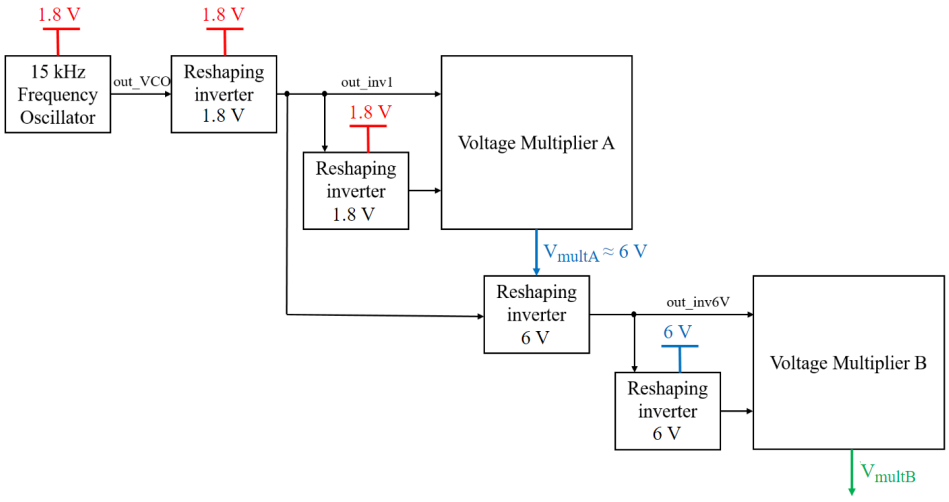

Figure 4.1: Cascade configuration of the VCO-driven voltage multipliers

4.2.1 Selected voltage multipliers

Voltage multipliers generate a high DC output voltage from a lower DC voltage supply through the storage and transfer of accumulated charges across multiple stages containing capacitors. As such, they are sometimes called charge pumps and are particularly used in low power applications where high voltages are needed despite a small Vdd [139, 140]. Dickon voltage multiplier (DVM) [141, 142, 143] are one of the most common charge pump topologies used in low power systems.

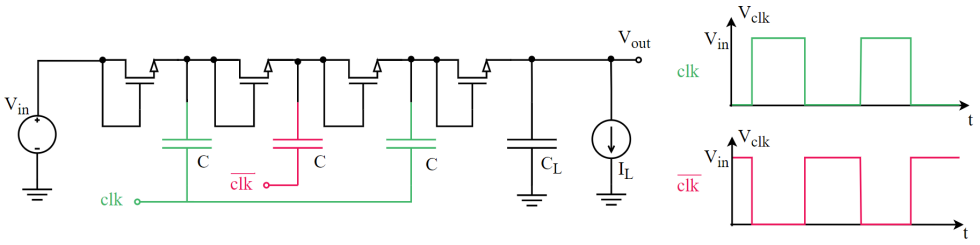

Figure 4.2: 3-stage Dickson voltage multiplier with diode-connected MOSFETs and the associated clock signals

The DVM [144], also known as the Dickson charge pump (DCP), operates using a series of diode-capacitor stages arranged in a cascade configuration connected to non-overlapping clocks (one for "odd" positioned capacitors, e.g C1, C3, C5, etc. and one for "even" capacitors, e.g. C2, C4, C6). The circuit functions in the following manner. Let D_i and C_i denote the diode-connected MOSFET and capacitor of the i^{th} stage. Ideally, when the clock signal clk is at a low state, capacitor C1 charges up to Vin = Vdd through D1. As clk transitions to a high state, the top plate of C1 rises to 2Vin. At this point, D1 stops conducting while D2 is turned on (as signals clk and $c\bar{l}k$ are complementary). This allows capacitor C2 to get charged to 2Vdd. During the next cycle, as clk returns to a low state, $c\bar{l}k$ transitions to a high state, leading to the charging of C3 to 3Vdd. As the clock signal cycles, this process continues, transferring the charge up the chain of capacitors [145]. The final output voltage is taken from the load capacitor C_L, last in the cascade, which is connected to ground and not to a clock phase. It comes as a multiple of the input voltage, and this factor is determined by the number of stages in the multiplier. For example, a 3-stage Dickson multiplier as depicted in Figure 4.2 would result in an output voltage of four times the input voltage. If we take into consideration the parasitic capacitances (Cp) that are formed at each stage, the expression of the output voltage for an N-stage DVM can be formulated with:

$$V_{out} = V_{dd} + \sum_{i=1}^{N} \left(\frac{V_{clk} C_i}{C_i + C_{pi}} - \frac{I_{Li}}{f_{clk}(C_i + C_{pi})} - V_{th} \right) \tag{4.1}$$

Which, assuming all stages to be identical, can be simplified to :

$$V_{out} = V_{dd} + N\Delta V \tag{4.2}$$

with $\Delta V = V_{clk} \frac{C}{C+C_p} - \frac{I_L}{f_{clk}(C+C_p)} - V_{th}$ the fluctuation voltage at each pumping stage [146, 142]. V_{clk} is the voltage amplitude of the clock signals, which is supposedly equal to the supply voltage, C is the value of each pumping capacitor, C_p is the parasitic capacitance at each pumping node, I_L is the

output current, f_{clk} is the clock frequency and V_{th} the threshold voltage of the NMOS.

$\Delta V \approx V_{clk} - V_{th} = Vdd - V_{th}$ if both C_p and I_L are sufficiently small and C is chosen sufficiently large. The output voltage and efficiency of DVM thus encounter limitations due to the threshold voltage and body effect coefficient, especially when numerous pumping stages are involved. Still, as we are working with low-V_{th} transistors and a supply of 1.8 V, the output voltage has not been as significantly affected by this constraint.

The rise time can be expressed by [147]:

$$t_r = N^2 \frac{C_{Leq}}{C_T} T ln \frac{(N+1).Vdd - V_{out}(0)}{(N+1).Vdd - V_{out}(t_r)} \tag{4.3}$$

where $C_T = NC$ is the total capacitance of the charge pump, T is the period of the clock, and $C_{Leq} = C_L + \frac{C_T}{3}$ denotes the equivalent capacitance at the output node.

Here, we use a 4-stage DVM with diode-wired low-threshold voltage neli transistors of size 4 µm/0.18 µm and each capacitor, including the load capacitor, has the same value C = 100 pF. This value is sufficient for supplying all the digital gates as the current drain of these gates is extremely low, barely discharging the capacitor.

To produce a stimulation of sufficient amplitude, the multiplier requires a rise time of less than 10 ms with a 1 µF load capacitance. However, achieving this requirement using the Dickson topology is not feasible, as per equation 4.3, as it would need 2.6 s.

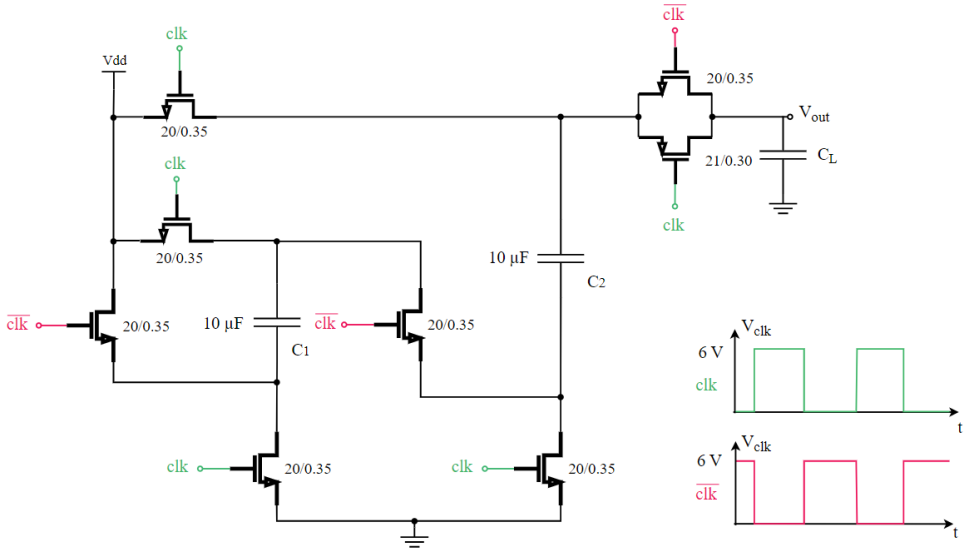

Figure 4.3: Capacitive voltage multiplier

Consequently, we opted for the architecture illustrated in Figure 4.3 for the second multiplier, which was notably used in [28, 138].

It operates using two phases dictated by non-overlapping signals:

- Charging phase : Both pumping capacitors C1 and C2 are charged to Vdd (clk = 1).
- Pumping phase : C1 and C2 form a series connection with the battery, resulting in a voltage equal to 3Vdd, which is transferred to the storage capacitor C_L ($c\bar{l}k = 1$).

In contrast to the DVM controlled by 0 or 1.8 V signals, this capacitive voltage multiplier employs high-level [0-6] V commands. The bulk of the ne3i transistors are connected to ground while the bulk of the pe3i is connected to V_{out}, the highest potential.

To implement these two multipliers, a total of 8 external capacitors are required: 5 capacitors with a value of 100 pF for the DVM, 2 pumping capacitors of 10 µF for the capacitive multiplier, and one load capacitor of 1 µF to be discharged into the H-bridge. For reference, table 4.1 indicates the sizes of the corresponding capacitors that can be found on the market.

Capacitor value	Size	Manufacturer
100 pF	0.25 mm x 0.125 mm x 0.125 mm	Murata Manufacturing
1 µF	0.6 mm x 0.3 mm x 0.3 mm	Taiyo Yuden
10 µF	1.6 mm × 0.8 mm × 1.25 mm	Murata Manufacturing

Table 4.1: External capacitor size chart

4.2.2 Multipliers with the kHz-range oscillator

The purpose of this kHz-range oscillator is to drive the two multipliers in order to charge the capacitors in a sufficiently short period of time. Here, the primary concern lies in power consumption rather than the accuracy of the oscillation frequency. The only condition is to maintain a frequency above 4 kHz even in the worst case to ensure the proper operation of the multipliers, meaning with a sufficiently small rise time. Among the possible low power architectures for this oscillator within this frequency range, the selected design is a subthreshold current-starved VCO [148]. One particularity of the subthreshold oscillator lies in its oscillations not being rail-to-rail nor symmetrical, thus necessitating a reshaping inverter. To avoid an excess of power consumption, current-starved inverters have been dimensioned for reshaping at both 1.8 V and 6 V as presented in Figure 4.1. The subthreshold current-starved kHz-range oscillator is presented in Figure 4.4. It is composed of three stages. The current sources are in subthreshold thanks to the 200 mV reference and the transistors in the middle have been sized with larger and longer dimensions to use their parasitic capacitances to oscillate around 15 kHz.

As presented in Figure 4.1, the operation of multiplier B depends entirely on the output voltage obtained from multiplier A (V_{multA}), which is used for the reshaping inverter to create the commands for multiplier B. To verify the viability of the configuration depicted in Figure 4.1, Figure 4.5 displays the simulation results in the typical case (tm) for all signals: the output of the VCO (out_{VCO}), the output of the 1.8V-reshaping inverter (out_{inv1}), the output of the 6V-reshaping inverter (out_{inv6V}) and the output of the two multipliers V_{multA} and V_{multB}.

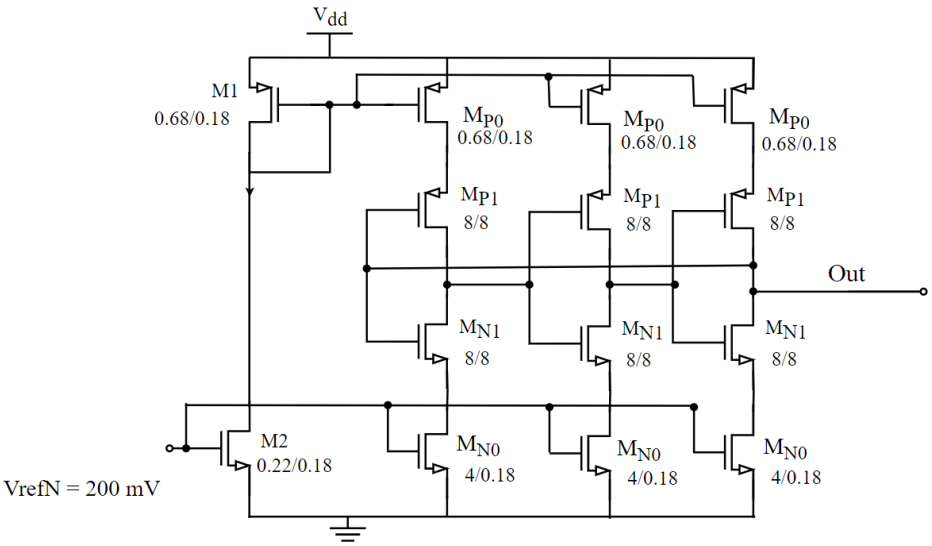

Figure 4.4: Current-starved subthreshold VCO

From this figure, it can observed that the reshaping to 6 V of the command for multiplier B starts only after the reshaping inverter is correctly supplied with 6 V, i.e. after 1 ms. Thereafter, once the reshaping begins, multiplier B can function correctly.

The study of both multipliers A and B was conducted in all five analysis scenarios, namely the nominal case and the four corners.

The oscillation frequency exhibits a strong dependence on threshold voltage variation, varying from 7.2 kHz in ws to 129.8 kHz in wp, and is about 14.7 kHz in tm. Therefore, verifying the operation of the multipliers in each worst case becomes crucial. Figure 4.6 shows the obtained simulation results. For each worst case multiplier B presents a rise time of around 10 ms which is compatible with our application. The complete configuration composed of the VCO, its reshaping circuit and multiplier A, has an overall power consumption of 9.9 µW.

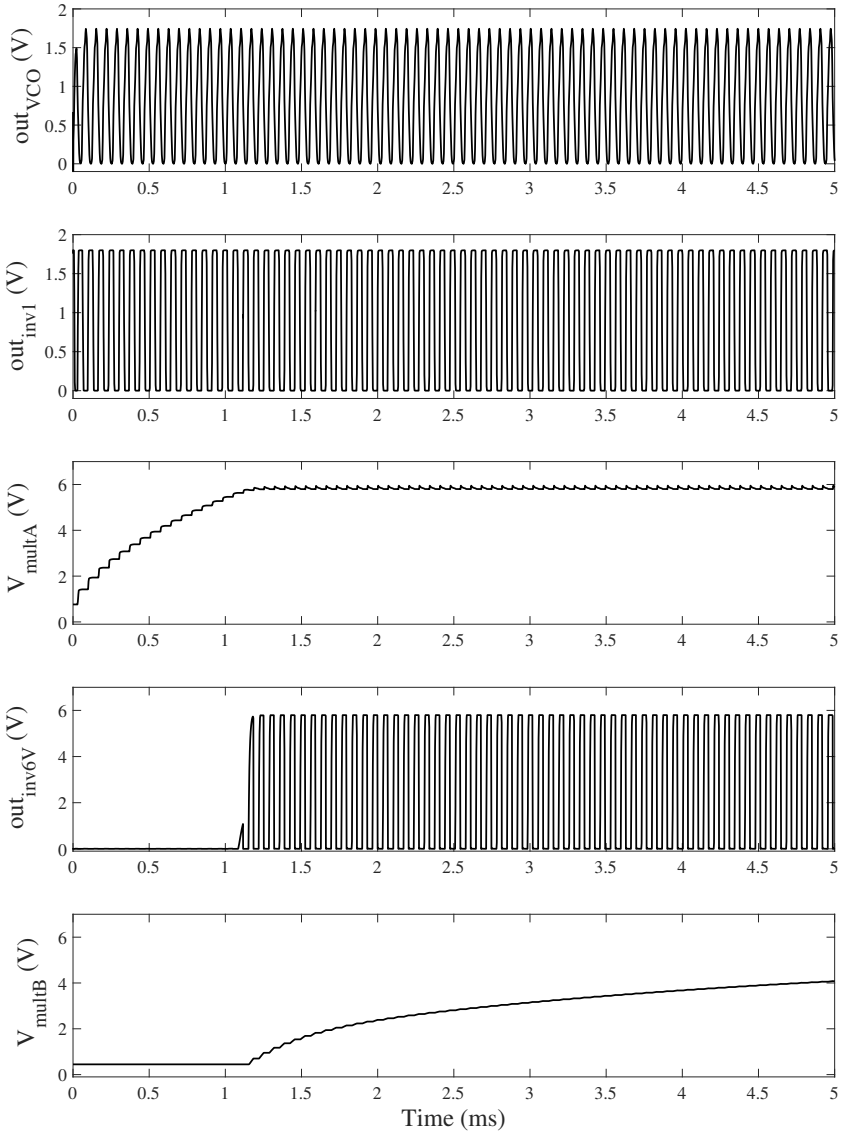

Figure 4.5: Signals from the Voltage Multipliers + VCO configuration

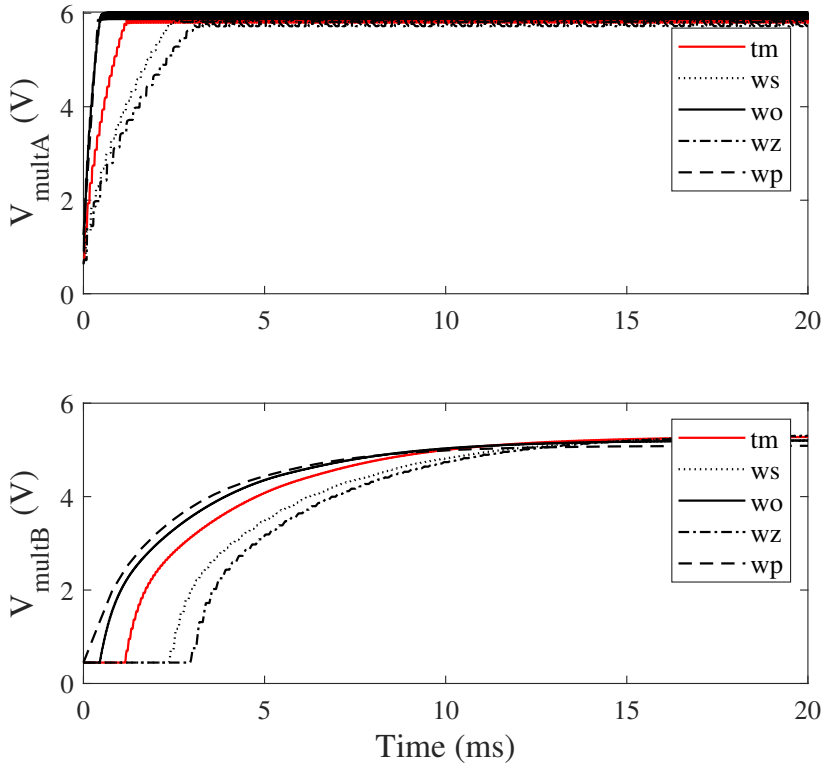

Figure 4.6: Worst case simulation of Multipliers A and B in the common configuration

4.3 Global simulation results

As highlighted in Chapter 3, the complete circuit has been designed with XFAB 0.18 µm CMOS technology and simulated using Cadence Virtuoso. The circuit operates on a 1.8 V voltage supply and the pacemaker load was modeled to align with our observations outlined in Chapter 2, utilizing a 133 kΩ resistance.

Figure 4.7 exhibits biphasic stimulation pulses along with the corresponding current waveform produced by the proposed circuit obtained for a transient noise analysis, with a noise bandwidth set to 100 kHz. While only the lowest (6.8 Hz) and highest (10.1 Hz) frequencies are depicted for clarity, it is important to note that these waveforms can be obtained at various frequencies based on the capacitor combination of the relaxation oscillator. Table 4.2 recapitulates the operable switch combinations along with the corresponding capacitor values and pacing rates in Hertz and beats per minute.

The peak-to-peak amplitude measures 9 V, going from -5 V to 4 V. Additionally, the current of every waveform exceeds 30 µA, meeting the required

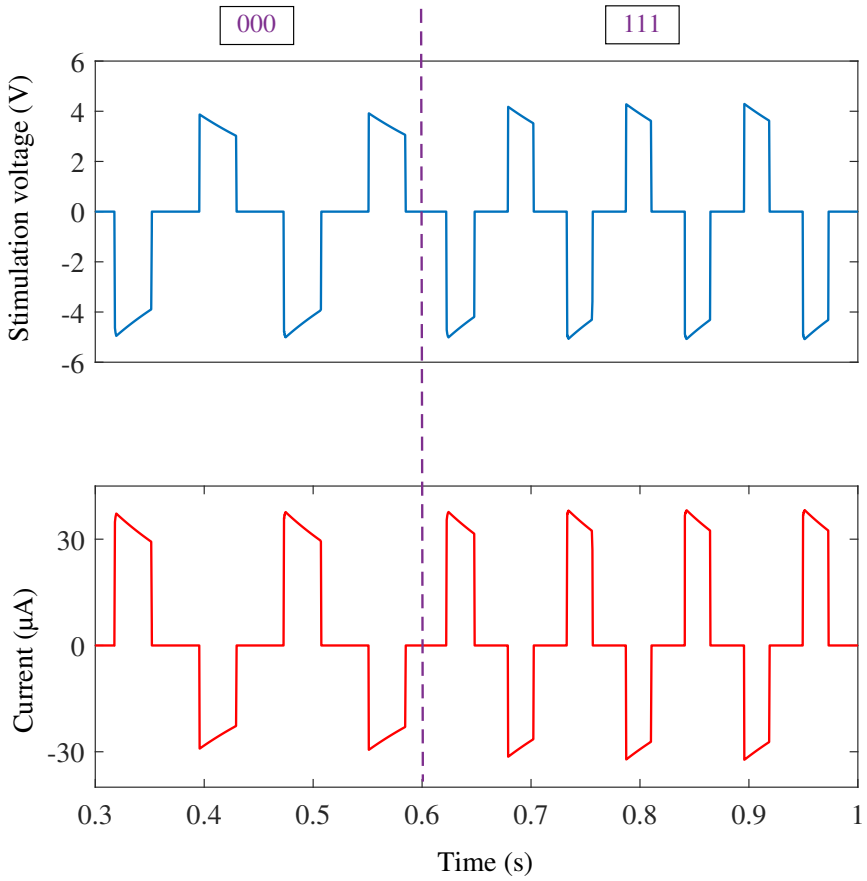

Figure 4.7: Stimulation waveform and current waveform at 6.8 and 10.1 Hz

threshold for effective stimulation. Figure 4.8 reports the power consumption repartition for the stimulation circuit. Its overall power consumption totals 111.7 µW, of which 100 µW is consumed directly by the H-bridge for the stimulation of the heart, which requires two pulses of at least 30 µA per wave period, as established by the in vivo tests. The oscillator in the kHz range with its reshaping and one of the multipliers consumes 9.9 µW. Finally, thanks to the ultra-low power approach adopted in this design, the relaxation oscillator and control synthesis assembly consume only 1.8 µW, i.e. 1.6 % of the total stimulation circuit. A typical battery capacity in pacemakers ranges between 0.5 to 1.2 A.h [149]. If we consider a battery with a capacity of 1 A.h, we could estimate the longevity of our "pacemaker" with continuous pacing to 16129.032 hours, which is almost two years, roughly the lifespan of a rat, which is fairly good. Of course this estimation should be taken with a pinch of salt as it only takes into account the stimulation circuit and a more complete system would drain more current from the additional features. In addition, the power consumption depends on the pacing parameters, i.e. the pacing amplitude and the pacing rate.

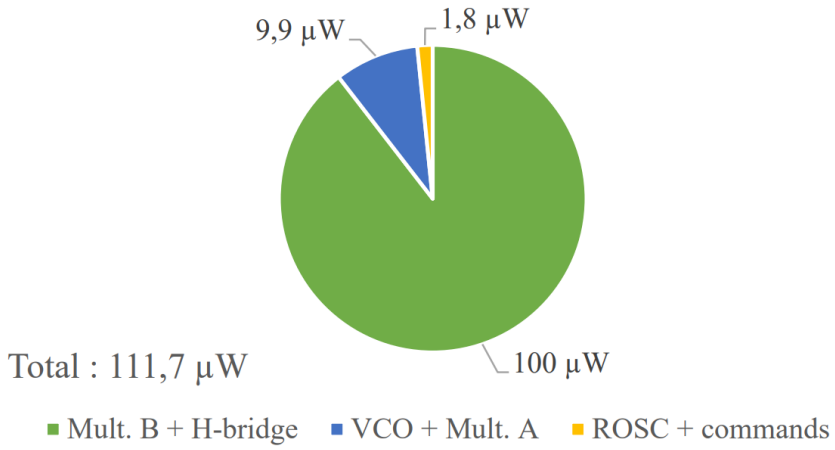

Figure 4.8: Power consumption repartition

S3S2S1	Capacitor value (pF)	Frequency (Hz)	Frequency (bpm)
000	3.8	6.8	408
001	4.13	7.1	432
010	4.46	7.6	456
011	4.79	8	480
100	5.12	8.4	504
101	5.45	8.9	534
110	5.78	9.5	570
111	6.11	10.1	606

Table 4.2: Stimulation pulse rate according to the capacitor value

4.4 Position to the state of the art

To assess and situate the performances of this work, we propose to compare it with integrated stimulation circuits found in the literature. While these studies primarily emphasize other aspects of the pacemaker, specific elements remain relevant for our comparative analysis. Table 4.3 summarizes the key performance metrics of the different circuits. We focused on the stimulation characteristics: type of stimulation, maximum amplitude, and pulse duration, to evaluate the ranges over which circuits with similar purposes to our own can operate. In addition, power consumption and external components are essential to consider for implantability. Indeed, given the limited size and capacity of the battery that can be used in small animal devices, low power consumption allows for extended lifespan of the system. Although some studies rely on batteryless devices, they have the disadvantage of requiring more external components and additional apparel, limiting the scope of experiments.

Wirelessly powered devices, such as those referenced in [14, 31, 33], necessitate at least two modules: a subcutaneous module and an external one. The external module serves to power the device, allowing the subcutaneous

module to operate without a large battery, resulting in a much smaller area, which is practical for implantation. Nevertheless, the wireless transfer of power and data imposes significant limitations on the study environment since both modules must be in close proximity (a couple centimeters) for reliable communication and hence, stimulation delivery. Furthermore, the power consumption stemming from this setup is notably high, typically within the mW range, which is roughly a hundred times higher than our consumption despite us generating a higher output voltage (but it is important to keep in mind that their power consumption encompasses additional features outside stimulation functionalities). In [33], the stimulation module receives intermittent bursts of power from the external transmitter module. The received AC voltage is rectified, causing a capacitor to charge and subsequently increase the output voltage. The capacitor discharges when the transmitter stops transmission, delivering monophasic stimulation with a programmed pulse duration. However, the electrodes require shorting to prevent tissue damage. In contrast, with biphasic stimulation, the second phase enables the heart to return to a neutral charge state, eliminating the need for electrode shortening and reducing the risk of tissue damage.

In [14]'s study, a pacemaker model is introduced that incorporates the combination of electrical and optogenetic stimulus, the latter offering the advantage of targeting specific cells for stimulation. Still, optoelectronic elements need important power to operate, which consequently impacts the overall power consumption of the system. Among the compared circuits, [28]'s approach is the most similar. It employs a capacitive voltage multiplier alongside a high-voltage output DAC, enabling the delivery of a rectangular pulse with customizable voltage and pulse width. Wong's focus on optimizing his circuit is apparent in the achieved power consumption, which amounts to 8 µW for a 2.8 V stimulation, yet he doesn't give information on the power consumption for his maximum amplitude stimulation. In addition, our pulse duration is much longer to ensure the safety of the rat's tissue, partially explaining why we have a higher consumption.

Overall, the circuit described in this thesis shows its value over the current literature when combining all previous points: it is able to deliver the highest pulse voltage and a large frequency range fitted to our application, while conserving a relatively low power consumption. It is thus very well-suited to meet the specific needs that studying PAH in small mammals entails. Indeed, having large ranges of voltage and frequency allows to explore more comprehensively the impact of cardiac frequency in PAH, and a very low power consumption will allow for experiments to be conducted in the long term while using a small battery that is well-fitted for the size of rats or mice.

	JSSC04 [28]	TBioCas11 [29]	Nature2017 [30]	Nature2019 [14]	TBioCas19 [31]	AICSP19 [32]	TBME22 [33]	This work
Process	0.5 µm	0.35 µm	-	-	0.18 µm	0.18 µm	0.18 µm HV	0.18 µm
Stimulation type	Voltage	Voltage	Voltage	Voltage + Optical	Voltage	Voltage	Voltage/Current	Voltage
Max. pulse voltage	7.5 V	3.2 V	2 V	2.2 V	3.6 V	3 V	5.5 V	9 Vpp
Stimulation frequency	-	0.5 - 31.25 Hz	1 Hz	5 - 10 Hz	-	100 Hz -100 kHz	1 Hz	6.8-10.1 Hz
Pulse duration	0.5 ms	0.63 - 1.94 ms	1 ms	250 ms	0.3 ms	-	0.2- 1 ms	25-35 ms
Total power consumption	8 µW	48 µW	1 mW	6 mW	1 W	-	1 mW	111.7 µW
External components	Leads + Capacitors	Lead + Coil + Batteries + Cap.	-	Lead + µLED + Antenna	Coil + LED + Cap.	Crystal	Coil + LED + Resistor + Cap.	Capacitors

Table 4.3: Performance comparison

4.5 Conclusion

This chapter marks the end of three years of work dedicated to designing an integrated circuit for cardiac stimulation in small rodents serving research on cardiovascular disease. The proposed circuit, supplied with 1.8 V, includes two voltage multipliers in the form of a capacitive multiplier and a Dickson charge pump. The first one assures the voltage supply for the charge and discharge of the capacitance in the H-Bridge, while the latter is dedicated to the high-voltage control signals. The stimulation circuit generates a biphasic stimulation with an exponential discharge, having a peak-to-peak amplitude of 9 V and a minimum current of 30 µA, meeting the requirements for reliable stimulation according to our in vivo studies. The pulse frequency is programmable, offering eight frequencies ranging between 6.8 and 10.1 Hz. The total power consumption amounts to less than 112 µW, of which almost 90 % is dedicated to the stimulation. This value aligns with those found in the literature and could potentially be further reduced.

Chapter 5

Conclusion

Pulmonary arterial hypertension (PAH), a rare and severe cardiovascular condition, poses considerable challenges in diagnosis and treatment. As cardiac frequency seems to be highly involved in the progression of the disease, our research strives to investigate heart rate modulation in cardiopulmonary physiology to gain critical insights into PAH and expand the potential treatment options. Understanding the specific role of heart rate in its progression necessitates further exploration, and the most practicable method to pursue this investigation involves the use of animal models, notably rats, owing to the similarities in their cardiac systems to humans' and their high reproductive rate.

However, based on our current understanding, there isn't any pharmaceutical compound known to exclusively increase cardiac frequency without affecting other essential cardiac parameters. Thus, we shifted our focus to an electrical approach employing an artificial cardiac pacemaker.

The lack of commercially available pacemakers tailored for small animals highlights the importance of our exploration for an implantable cardiac stimulating device that meets our research criteria. Developing such a system presents hurdles, notably in achieving a compact size and meeting the ultra-low power demands for implantation. The available literature on pacemakers tends to be limited and guarded, with a sparse amount of comprehensive information. Academic articles extensively discussing pacemakers are relatively few in number, and patents related to this field often date back to earlier years. This scarcity of detailed and openly available information can make it challenging to access thorough and up-to-date resources concerning pacemaker technology and advancements.

This thesis aspired to set out on the development of an integrated pacemaker circuit, with an initial focus on the design of the pulse generator. Our research led to the design and conception of an integrated stimulation circuit capable of delivering a biphasic waveform at adjustable frequencies between 6.8 and 10.1 Hz, corresponding to beats of 408 to 606 bpm.

In Chapter 1, we introduced fundamental contextual knowledge of the functioning of the heart and pacemaker devices, to prepare for what follows. We presented PAH, its symptoms, its causes, and more importantly its relation to cardiac frequency, outlining the driving force behind the creation of a pacemaker device tailored for rats. We elaborated on the circulatory system of the heart, responsible for pumping the blood to the rest of the body, and triggered and coordinated by the electrical activity. This activity derives from the spontaneous depolarization of a specialized group of cells in the heart called pacemaker cells, primarily located in the sinoatrial node (SA node), and often referred to as the heart's natural pacemaker. The SA node generates electrical impulses which travel through a determined conducting pathway, ultimately spreading across the heart's lower chambers. As the impulses propagate, they stimulate the heart muscle cells to contract and relax in a synchronized manner, facilitating the rhythmic beating of the heart. Naturally, we then detailed the general architecture and function of an artificial cardiac pacemaker, primarly used to operate the electrical activity when the heart is impaired. We went on covering the advent of leadless cardiac pacemakers, a promising alternative, bypassing potential complications linked to traditional pacemakers, most commonly involving leads or implantation. This innovation, along with the emergence of wireless and battery-free multimodal pacemakers, highlight the ongoing pursuit of more efficient, minimally invasive, and enduring pacing solutions.

While numerous aspects require attention, one pivotal element lies in specifying the stimulation waveform, which serves as the core function of a cardiac pacemaker. This parameter significantly influences battery consumption, underscoring the necessity to strike a delicate balance between effeciency and power preservation. In Chapter 2, we thus elaborated on various parameters essential for defining the stimulation waveform, offering a comprehensive specification guide. Our approach began with a comprehensive overview of load models and stimulation waveforms commonly utilized in the development of human pacemakers. This foundational understanding enabled us to consider diverse waveforms. Based on two in vivo experiments conducted on rats with the collaboration of the INSERM, we demonstrated and confirmed the validity of the chosen waveform using an FPGA prototype. The proposed stimulation takes the form of a biphasic impulse, with a truncated exponential discharge and pulse durations ranging from 100 ms to 150 ms, corresponding to the upper limit within the physiological range and extends into the hyperphysiological range of heart rates in rats. We also identified a minimum current of 30 µA for an efficient stimulation and an equivalent pacemaker load model embodied by a 133 kΩ resistance.

Following the waveform specification, Chapter 3 detailed the design process and analysis of the proposed stimulation IC, with a focus placed on each

component. As a whole, the circuit, powered by 1.8 V, incorporates two voltage multipliers driven by a 15 kHz VCO: a capacitive multiplier and a Dickson charge pump. The capacitive multiplier ensures a sufficient voltage supply discharging in the H-Bridge for an effective stimulation, while the Dickson charge pump manages the high-voltage command signals. An essential component for generating the signals that control the H-bridge is a programmable ultra-low power, low frequency relaxation oscillator. Operating at variable frequencies between 15.3 and 23.8 Hz, the proposed ROSC consists of DLS logic components, highly minimizing the leakage current in said components, an ULP comparator, and current sources in the subthreshold region. Within the frequency range of our application, both the DLS logic blocks and the ULP comparator demonstrate notable robustness, which allows the proposed ROSC to uphold its robustness against process variations. Regarding the power consumption of the sub-blocks, 100 µW is consumed directly by the H-bridge and multiplier B for the stimulation of the heart, 9.9 µW for the VCO with its reshaping circuit and multiplier A, and only 1.8 µW for the relaxation oscillator and control synthesis assembly thanks to the ultra-low power approach adopted in its design. This ensures that the majority of the current is channeled toward cardiac stimulation. The number of external components in our architecture may raise concerns regarding the size of the device. However, considering the dimensions of existing capacitors available in the market, our circuit should maintain a reasonable size for potential implantation in future works.

Finally, the developed circuit generates a biphasic stimulation with an exponential discharge, delivering a peak-to-peak amplitude of 9 V and ensuring a minimum current of 30 µA, meeting the criteria established for reliable stimulation based on our studies. It offers programmable pulse frequencies, encompassing a range of eight frequencies varying between 6.8 and 10.1 Hz. The entire stimulation circuit consumes less than 112 µW, which is comparable to circuits in the literature.

Perspectives

This work marks a first step toward a large series of research studies spread over multiple fields, and more extensive work obviously remains essential to develop a fully customized device. For instance, exploring battery management and establishing communication between the device and an external control station, enabling doctors to monitor pacemaker status or adjust parameters, are areas for investigation. However, these aspects fall outside our area of expertise.

For our part, a first area for improvement concerns, as we have seen in Chapter 3, the current sources of the ROSC, to ensure a robust system for the key component. Several studies on ULP nanoscale range current references

with low process sensitivity exists in the literature and an in-depth study deserves to be undertaken given the critical aspect that these sources have on the functioning of the oscillator. We have already started the conception of a circuit based on [108] PTAT current source. Furthermore, as of now, we are still using ideal voltage sources for the voltage references used in the simulations. Therefore, it is necessary to design the circuit for establishing the appropriate voltage references.

Despite completing the layout and post-layout simulation of various blocks, particularly the DLS components, we have yet to undertake the layout process for the entire circuit and perform its post-layout analysis. These simulations, incorporating parasitic capacitors, are essential for obtaining a more accurate depiction of the circuit's behavior and performance. Additionally, they will offer insights into the overall surface area occupied by the circuit.

Since the study was limited to acute testing, it was not possible to assess the long-term effects of the proposed stimulation. Longer experiments are already envisaged using the aforementioned FPGA prototype while waiting for a first version of the IC chip. From a medical point of view, these tests will allow to draw initial conclusions on the influence of heart rate on a rat model of PAH. From an electronic point of view, it will enable to test and improve (and consider new) features of the circuit. The library of ultra-low power logic gates developed as part of this thesis also opens the way for implementing complementary digital algorithms for the pacemaker or for other slow ULP digital processing applications. For instance, this could include heart rate detection on an integrated ECG (iECG) to verify that the rat's heart beats at the expected rate. An amplitude adaptive circuit could also be worth exploring. Adjusting the stimulation's strength based on real-time physiological changes within the body, would ensure that the stimulation remains effective and safe for each individual, preventing over- or understimulation.

The potential use of such a small stimulation device could be extended, not only to other laboratory animals but also to pets. Additionally, to another extent, it holds promise for addressing the needs of newborn babies, who still face significant challenges in finding suitable devices.

Publication

F. Pan, E. Avignon-Meseldzija, F. Perros, D. Mika, D. Boulate and A. Kolar, "A programmable pulse generator for atrial pacing in rats for studies on Pulmonary Arterial Hypertension," 2021 28th IEEE International Conference on Electronics, Circuits, and Systems (ICECS), Dubai, United Arab Emirates, 2021, pp. 1-4, doi: 10.1109/ICECS53924.2021.9665487.

Bibliography

[1] Deborah Jo Levine. “Pulmonary arterial hypertension: updates in epidemiology and evaluation of patients.” In: *American Journal of Managed Care* 27 (2021).

[2] *Pulmonary Arterial Hypertension - Symptoms Causes | Mount Elizabeth Hospitals*. URL: https://www.mountelizabeth.com.sg/conditions-diseases/pulmonary-arterial-hypertension/symptoms-causes.

[3] Norris SH Lan et al. “Pulmonary arterial hypertension: pathophysiology and treatment”. In: *Diseases* 6.2 (2018), p. 38.

[4] Nazzareno Galiè et al. “Risk stratification and medical therapy of pulmonary arterial hypertension”. In: *European Respiratory Journal* 53.1 (2019).

[5] Natascha Sommer et al. “Current and future treatments of pulmonary arterial hypertension”. In: *British journal of pharmacology* 178.1 (2021), pp. 6–30.

[6] Fred Kusumoto and Fettache Nora. *Cardiac pacing for the clinician: Second edition*. Jan. 2008, pp. 1–742. ISBN: 978-0-387-72762-2. DOI: 10.1007/978-0-387-72763-9.

[7] Aboutkidshealth. *Components of a pacemaker*. URL: https://www.aboutkidshealth.ca/Article?contentid=980&language=English.

[8] Michel François Laurent. “Les différents types de Pacemakers : Utilisation en Médecine Vétérinaire”. PhD thesis. 2003. URL: https://sofia.medicalistes.fr/spip/IMG/pdf/Les_differents_types_de_pacemakers_utilisation_en_medecine_veterinaire_These_du_Dr_Laurent_Michel_FRANCOIS_.pdf.

[9] D. Hervé and J.-C Troger. “Retrospective study of the implantation of eighteen cardiac pacemakers in the dog”. In: *Pratique Medicale et Chirurgicale de l’Animal de Compagnie* 38 (Mar. 2003), pp. 161–166.

[10] R.A. Santilli et al. “Indications for permanent pacing in dogs and cats”. In: *Journal of Veterinary Cardiology* 22 (2019). Cardiac Pacing, pp. 20–39. ISSN: 1760-2734. DOI: https://doi.org/10.1016/j.jvc.2018.12.003. URL: https://www.sciencedirect.com/science/article/pii/S1760273418301395.

[11] Han OuYang et al. “Symbiotic cardiac pacemaker”. In: *Nature Communications* 10 (Apr. 2019). DOI: 10.1038/s41467-019-09851-1.

[12] Jacob Laughner et al. “A Fully Implantable Pacemaker for the Mouse: From Battery to Wireless Power”. In: *PloS one* 8 (Oct. 2013), e76291. DOI: 10.1371/journal.pone.0076291.

[13] Maarten Hulsmans et al. “A Miniaturized, Programmable Pacemaker for Long-Term Studies in the Mouse”. In: *Circulation research* 123 (Nov. 2018). DOI: 10.1161/CIRCRESAHA.118.313429.

[14] Philipp Gutruf et al. “Wireless, battery-free, fully implantable multimodal and multisite pacemakers for applications in small animal models”. In: *Nature Communications* 10 (Dec. 2019), p. 5742. DOI: 10.1038/s41467-019-13637-w.

[15] Yeon Sik Choi et al. “Fully implantable and bioresorbable cardiac pacemakers without leads or batteries”. In: *Nature Biotechnology* 39 (June 2021), pp. 1–11. DOI: 10.1038/s41587-021-00948-x.

[16] S Serge Barold, Roland X Stroobandt, and Alfons F Sinnaeve. *Cardiac pacemakers and resynchronization step by step: An illustrated guide*. John Wiley & Sons, 2010.

[17] Richard S. Sanders. “The Pulse Generator”. In: *Cardiac Pacing for the Clinician*. Ed. by Fred M. Kusumoto and Nora F. Goldschlager. Boston, MA: Springer US, 2008, pp. 47–71. ISBN: 978-0-387-72763-9. DOI: 10.1007/978-0-387-72763-9_2. URL: https://doi.org/10.1007/978-0-387-72763-9_2.

[18] W.A. Tacker and L.A. Geddes. “The laws of electrical stimulation of cardiac tissue”. In: *Proceedings of the IEEE* 84.3 (1996), pp. 355–365. DOI: 10.1109/5.486739.

[19] OZ Roy and RW Wehnert. “A more efficient waveform for cardiac stimulation”. In: *Medical and biological engineering* 9.5 (1971), pp. 495–501. DOI: https://doi.org/10.1007/BF02474706.

[20] Richard D Klafter and Leonid Hrebien. “An in vivo study of cardiac pacemaker optimization by pulse shape modification”. In: *IEEE Transactions on Biomedical Engineering* 3 (1976), pp. 233–239. DOI: 10.1109/TBME.1976.324636.

[21] KM Kavanagh et al. “Monophasic versus biphasic cardiac stimulation: mechanism of decreased energy requirements”. In: *Pacing and Clinical Electrophysiology* 13.10 (1990), pp. 1268–1276. DOI: https://doi.org/10.1111/j.1540-8159.1990.tb02026.x.

[22] Roessmann Uros Mortimer J. Thomas Kaufman David. “Intramuscular electrical stimulation: Tissue damage”. In: *Annals of Biomedical Engineering* 8.3 (1980), pp. 235–244. DOI: 10.1007/BF02364479.

[23] Krzysztof Iniewski. *VLSI Circuits for Biomedical Applications*. 2008.

[24] Richard D Klafter. “An optimally energized cardiac pacemaker”. In: *IEEE Transactions on Biomedical Engineering* 5 (1973), pp. 350–356. DOI: 10.1109/TBME.1973.324287.

[25] Stuart P Lahtinen and Russell E Anderson. *Low energy pacing pulse waveform for implantable pacemaker*. US Patent 5,782,880. July 1998.

[26] Fanny Pan et al. “A programmable pulse generator for atrial pacing in rats for studies on Pulmonary Arterial Hypertension”. In: *2021 28th IEEE International Conference on Electronics, Circuits, and Systems (ICECS)*. 2021, pp. 1–4. DOI: 10.1109/ICECS53924.2021.9665487.

[27] A. Esmailiyan et al. “A charge-pump based multi-mode stimuli generator for cardiac pacemaking”. In: *2016 14th IEEE International New Circuits and Systems Conference (NEWCAS)*. 2016, pp. 1–4. DOI: 10.1109/NEWCAS.2016.7604752.

[28] L.S.Y. Wong et al. “A very low-power CMOS mixed-signal IC for implantable pacemaker applications”. In: *IEEE Journal of Solid-State Circuits* 39.12 (2004), pp. 2446–2456. DOI: 10.1109/JSSC.2004.837027.

[29] Shuenn-Yuh Lee et al. “A Programmable Implantable Microstimulator SoC With Wireless Telemetry: Application in Closed-Loop Endocardial Stimulation for Cardiac Pacemaker”. In: *IEEE transactions on biomedical circuits and systems* 5 (Dec. 2011), pp. 511–22. DOI: 10.1109/TBCAS.2011.2177661.

[30] Parinaz Abiri et al. “Inductively powered wireless pacing via a miniature pacemaker and remote stimulation control system”. In: *Scientific Reports* 7 (Dec. 2017). DOI: 10.1038/s41598-017-06493-5.

[31] Hongming Lyu et al. “A 430-MHz Wirelessly Powered Implantable Pulse Generator With Intensity/Rate Control and Sub-1 A Quiescent Current Consumption”. In: *IEEE Transactions on Biomedical Circuits and Systems* 13.1 (2019), pp. 180–190. DOI: 10.1109/TBCAS.2018.2879357.

[32] Wei-Hsien Chen et al. “A charge accumulation-free voltage-controlled functional electrical stimulator with bi-phasic sinusoidal stimulation”. In: *Analog Integrated Circuits and Signal Processing* 101 (Nov. 2019). DOI: 10.1007/s10470-019-01417-x.

[33] Usama Anwar et al. “Towards a Leadless Wirelessly Controlled Intravenous Cardiac Pacemaker”. In: *IEEE Transactions on Biomedical Engineering* 69.10 (2022), pp. 3074–3086. DOI: 10.1109/TBME.2022.3161415.

[34] Texas Heart Institute. *Heart Anatomy*. URL: https://www.texasheart.org/heart-health/heart-information-center/topics/heart-anatomy/.

[35] A. C. Guyton and J. E. Hall. *Textbook of Medical Physiology, 11th ed.* UNIT III. Elsevier Saunders, 2006. ISBN: 0-7216-0240-1. URL: https://faculty.ksu.edu.sa/sites/default/files/hall_textbook_of_medical_physiology.pdf.

[36] stanfordchildrens. *Anatomy and function of the heart*. URL: https://www.stanfordchildrens.org/en/topic/default?id=anatomy-and-function-of-the-electrical-system-90-P01762.

[37] R.X. Stroobandt, S.S. Barold, and A.F. Sinnaeve. *ECG from Basics to Essentials: Step by Step*. Wiley, 2015. ISBN: 9781119066422. URL: https://books.google.fr/books?id=UCtcCwAAQBAJ.

[38] WHO. *Top 10 causes of death*. URL: https://www.who.int/news-room/fact-sheets/detail/the-top-10-causes-of-death#:~:text=The%20top%20global%20causes%20of,birth%20asphyxia%20and%20birth%20trauma%2C.

[39] Nazzareno Galiè et al. “An overview of the 6th World Symposium on Pulmonary Hypertension”. In: *European Respiratory Journal* 53.1 (2019). ISSN: 0903-1936. DOI: 10.1183/13993003.02148-2018. eprint: https://erj.ersjournals.com/content/53/1/1802148.full.pdf. URL: https://erj.ersjournals.com/content/53/1/1802148.

[40] Dr. Laurent SAVALE. *PROTOCOLE NATIONAL DE DIAGNOSTIC ET DE SOINS - HYPERTENSION ARTERIELLE PULMONAIRE. (French) [National protocol for diagnosis and care]*. 2020.

[41] Gérald Simonneau et al. “Haemodynamic definitions and updated clinical classification of pulmonary hypertension”. In: *European respiratory journal* 53.1 (2019).

[42] Nazzareno Galiè et al. “2015 ESC/ERS Guidelines for the diagnosis and treatment of pulmonary hypertension”. In: *Kardiologia Polska (Polish Heart Journal)* 73.12 (2015), pp. 1127–1206.

[43] Marc Humbert et al. “Pulmonary arterial hypertension in France: results from a national registry”. In: *American journal of respiratory and critical care medicine* 173.9 (2006), pp. 1023–1030.

[44] Milos Opravil and Daniel Sereni. “Natural history of HIV-associated pulmonary arterial hypertension: trends in the HAART era”. In: *AIDS (London, England)* 22 Suppl 3 (Sept. 2008), S35–40. ISSN: 0269-9370. DOI: 10.1097/01.aids.0000327514.60879.47. URL: https://journals.lww.com/aidsonline/Fulltext/2008/09003/Natural_history_of_HIV_associated_pulmonary.6.aspx.

[45] Kurt W Prins and Thenappan Thenappan. “World Health Organization Group I pulmonary hypertension: epidemiology and pathophysiology”. In: *Cardiology clinics* 34.3 (2016), pp. 363–374.

[46] Raymond L Benza et al. “An evaluation of long-term survival from time of diagnosis in pulmonary arterial hypertension from the REVEAL Registry”. In: *Chest* 142.2 (2012), pp. 448–456.

[47] Neil J Kelly and Stephen Y Chan. “Pulmonary Arterial Hypertension: Emerging Principles of Precision Medicine across Basic Science to Clinical Practice”. In: *Reviews in cardiovascular medicine* 23.11 (2022).

[48] Xin-Fang Leong, Chun-Yi Ng, Kamsiah Jaarin, et al. “Animal models in cardiovascular research: hypertension and atherosclerosis”. In: *BioMed research international* 2015 (2015).

[49] Helene Hardin-Pouzet and Serban Morosan. “Mice, rats and men: how rodent models are still required to produce knowledge”. In: *Medecine sciences: M/S* 35.5 (2019), pp. 479–482.

[50] D Papadimitriou et al. “The use of mice and rats as animal models for cardiopulmonary resuscitation research”. In: *Laboratory Animals* 42.3 (2008). PMID: 18625581, pp. 265–276. DOI: 10.1258/la.2007.006035.

[51] Theofilos Kolettis et al. “Characterisation of a rat model of pulmonary arterial hypertension”. In: *Hellenic J Cardiol* 48.4 (2007), pp. 206–10.

[52] Tingting Zhang et al. “Silibinin efficacy in a rat model of pulmonary arterial hypertension using monocrotaline and chronic hypoxia”. In: *Respiratory research* 20.1 (2019), pp. 1–12.

[53] Tian Jia et al. “Experimental rodent models of cardiovascular diseases”. In: *Frontiers in cardiovascular medicine* 7 (2020), p. 588075.

[54] Xiao-Han Wu et al. “Experimental animal models of pulmonary hypertension: Development and challenges”. In: *Animal Models and Experimental Medicine* 5.3 (2022), pp. 207–216.

[55] Houman Savoji et al. “Cardiovascular disease models: a game changing paradigm in drug discovery and screening”. In: *Biomaterials* 198 (2019), pp. 3–26.

[56] Piotr Konopelski and Marcin Ufnal. “Electrocardiography in rats: a comparison to human”. In: *Physiological research* 65.5 (2016), p. 717.

[57] Nima Milani-Nejad and Paul ML Janssen. “Small and large animal models in cardiac contraction research: advantages and disadvantages”. In: *Pharmacology & therapeutics* 141.3 (2014), pp. 235–249.

[58] Jerrold Tannenbaum and B Taylor Bennett. “Russell and Burch’s 3Rs then and now: the need for clarity in definition and purpose”. In: *Journal of the American association for laboratory animal science* 54.2 (2015), pp. 120–132.

[59] Harry G Mond and Alessandro Proclemer. “The 11th world survey of cardiac pacing and implantable cardioverter-defibrillators: calendar year 2009–a World Society of Arrhythmia’s project”. In: *Pacing and clinical electrophysiology* 34.8 (2011), pp. 1013–1027.

[60] Wilson Greatbatch. *"Medical cardiac pacemaker" U.S. Patent 3,057, 356*. Oct. 1962.

[61] Medtronic Inc. *"Leadless pacemaker system", US Patent 9,375,580 B2*. June 2016.

[62] Sandro Augusto Pavlik Haddad and Wouter A Serdijn. *Ultra low-power biomedical signal processing: an analog wavelet filter approach for pacemakers*. Springer Science & Business Media, 2009.

[63] MayoClinic. *pacemaker*. URL: https://www.mayoclinic.org/tests-procedures/pacemaker/about/pac-20384689.

[64] Haris M Haqqani, Laurence M Epstein, and Joshua M Cooper. “Engineering and construction of pacemaker and ICD leads”. In: (2011).

[65] Siva Mulpuru et al. “Cardiac Pacemakers: Function, Troubleshooting, and Management”. In: *Journal of the American College of Cardiology* 69 (Jan. 2017), pp. 189–210. DOI: 10.1016/j.jacc.2016.10.061.

[66] Hiroko Beck et al. “50th Anniversary of the first successful permanent pacemaker implantation in the United States: historical review and future directions”. In: *The American journal of cardiology* 106.6 (2010), pp. 810–818.

[67] Katie Ramm and Laura May. “Cardiac Support Equipment”. In: *Maths, Physics and Clinical Measurement for Anaesthesia and Intensive Care*. Ed. by Hozefa Ebrahim and DavidEditors Ashton-Cleary. Cambridge University Press, 2019, pp. 187–206.

[68] ecgwaves. *Basic cardiac pacing, pacemaker function and pacing*. URL: https://ecgwaves.com/topic/basic-cardiac-pacing-pacemaker-functions-and-settings/#:~:text=atria%20and%20ventricles.-,Sensing,be%20sensed%20by%20the%20pacemaker.l.

[69] Barouh V. Berkovits. *"Demand pacer", US Patent 3,528,428,* Sept. 1970.

[70] Károly Kaszala and Kenneth A. Ellenbogen. “Device Sensing”. In: *Circulation* 122.13 (2010), pp. 1328–1340. DOI: 10.1161/CIRCULATIONAHA.109.919704. eprint: https://www.ahajournals.org/doi/pdf/10.1161/CIRCULATIONAHA.109.919704. URL: https://www.ahajournals.org/doi/abs/10.1161/CIRCULATIONAHA.109.919704.

[71] Ewa Świerżyńska et al. “Rate-Responsive Cardiac Pacing: Technological Solutions and Their Applications”. In: *Sensors* 23.3 (2023). ISSN: 1424-8220. DOI: 10.3390/s23031427. URL: https://www.mdpi.com/1424-8220/23/3/1427.

[72] Clemens Steinwender et al. “State of the art: leadless ventricular pacing: A national expert consensus of the Austrian Society of Cardiology”. In: *Journal of Interventional Cardiac Electrophysiology* 57 (Dec. 2019). DOI: 10.1007/s10840-019-00680-2.

[73] Vaibhav R. Vaidya et al. “Real-world experience with leadless cardiac pacing”. In: *Pacing and Clinical Electrophysiology* 42.3 (2019), pp. 366–373. DOI: https://doi.org/10.1111/pace.13601. eprint: https://onlinelibrary.wiley.com/doi/pdf/10.1111/pace.13601. URL: https://onlinelibrary.wiley.com/doi/abs/10.1111/pace.13601.

[74] Mikhael El-Chami et al. “How to Implant a Leadless Pacemaker With a Tine-Based Fixation”. In: *Journal of cardiovascular electrophysiology* 27 (Sept. 2016). DOI: 10.1111/jce.13092.

[75] Toshimasa Okabe et al. “Tine-Based Leadless Pacemaker: Strategies for Safe Implantation in Unconventional Clinical Scenarios”. In: *JACC: Clinical Electrophysiology* 6.10 (2020), pp. 1318–1331. ISSN: 2405-500X. DOI: https://doi.org/10.1016/j.jacep.2020.08.021. URL: https://www.sciencedirect.com/science/article/pii/S2405500X20307945.

[76] American College of Cardiology. *Focus on EP | Leadless Technology: A Paradigm Shift in Cardiac Implantable Electronic Devices*. URL: https://www.acc.org/Latest-in-Cardiology/Articles/2021/04/01/01/42/Focus-on-EP-Leadless-Technology-A-Paradigm-Shift-in-Cardiac-Implantable-Electronic-Devices.

[77] Marc Miller et al. “Leadless Cardiac Pacemakers: Back to the Future”. In: *Journal of the American College of Cardiology* 66 (Sept. 2015), pp. 1179–89. DOI: 10.1016/j.jacc.2015.06.1081.

[78] J. William Spickler et al. “Totally self-contained intracardiac pacemaker.” In: *Journal of electrocardiology* 3 3-4 (1970), pp. 325–31. URL: https://api.semanticscholar.org/CorpusID:46634162.

[79] Abbott. *AVEIR VR Leadless Pacemaker*. URL: https://www.cardiovascular.abbott/us/en/hcp/products/cardiac-rhythm-management/pacemakers/aveir-vr-leadless-pacemaker/why.html.

[80] J Sperzel, C Hamm, and A Hain. “Leadless pacing”. In: *Herz* 43.7 (Nov. 2018), pp. 605–611. ISSN: 0340-9937. DOI: 10.1007/s00059-018-4752-9. URL: https://doi.org/10.1007/s00059-018-4752-9.

[81] Abbott. *AVEIR DR Leadless Pacemaker FDA approval*. URL: https://abbott.mediaroom.com/2023-07-05-Abbott-Receives-FDA-Approval-for-Worlds-First-Dual-Chamber-Leadless-Pacemaker.

[82] Vivek Y. Reddy et al. “CI-525-03 DEVICE-TO-DEVICE COMMUNICATION FOR A NOVEL DUAL-CHAMBER LEADLESS PACEMAKER SYSTEM: RELIABILITY OF MAINTAINING ATRIOVENTRICULAR SYNCHRONY IN AN OVINE MODEL OF AV CONDUCTION BLOCK”. In: *Heart Rhythm* 19.5, Supplement (2022). Heart Rhythm 2022: April 29-May 1, San Francisco, California, S39–S40. ISSN: 1547-5271. DOI: https://doi.org/10.1016/j.hrthm.2022.03.650. URL: https://www.sciencedirect.com/science/article/pii/S154752712200875X.

[83] Katarzyna Malaczynska-Rajpold et al. “Leadless Cardiac Pacing: New Horizons”. In: *Cardiology and therapy* 12 (Nov. 2022). DOI: 10.1007/s40119-022-00288-0.

[84] Balint Laczay, Jose Aguilera, and Daniel J Cantillon. “Leadless cardiac ventricular pacing using helix fixation: Step-by-step guide to implantation”. In: *Journal of cardiovascular electrophysiology* 34.3 (Mar. 2023), pp. 748–759. ISSN: 1045-3873. DOI: 10.1111/jce.15785. URL: https://doi.org/10.1111/jce.15785.

[85] Vivek Y Reddy et al. “Retrieval of the leadless cardiac pacemaker: a multicenter experience”. In: *Circulation: Arrhythmia and Electrophysiology* 9.12 (2016), e004626.

[86] Fleur VY Tjong and Vivek Y Reddy. “Permanent leadless cardiac pacemaker therapy: a comprehensive review”. In: *Circulation* 135.15 (2017), pp. 1458–1470.

[87] G. Hoffmann De Visme and A. Furness. “Minimum Energy Pulsing by Cardiac Pacemakers”. In: *IEEE Transactions on Biomedical Engineering* BME-29.7 (1982), pp. 546–549. DOI: 10.1109/TBME.1982.324928.

[88] Kara Bocan, Marlin Mickle, and Ervin Sejdic. “Multi-Disciplinary Challenges in Tissue Modeling for Wireless Electromagnetic Powering: A Review”. In: *IEEE Sensors Journal* PP (Sept. 2017), pp. 1–1. DOI: 10.1109/JSEN.2017.2748338.

[89] Eric McAdams and J Jossinet. “Tissue impedance: A historical overview”. In: *Physiological measurement* 16 (Sept. 1995), A1–13. DOI: 10.1088/0967-3334/16/3A/001.

[90] BRIAN G. CLELAND. “A Conceptual Basis for Pacing Waveforms”. In: *Pacing and Clinical Electrophysiology* 19.8 (1996), pp. 1177–1185. DOI: https://doi.org/10.1111/j.1540-8159.1996.tb04187.x. eprint: https://onlinelibrary.wiley.com/doi/pdf/10.1111/j.1540-8159.1996.tb04187.x. URL: https://onlinelibrary.wiley.com/doi/abs/10.1111/j.1540-8159.1996.tb04187.x.

[91] Thomas Bunch et al. “Pacing and Defibrillation: Clinically Relevant Basics for Practice”. In: Apr. 2021, pp. 1–38. ISBN: 9781119264002. DOI: 10.1002/9781119264002.ch1.

[92] Anna Norlin, Jinshan Pan, and Christofer Leygraf. “Electrochemical Behavior of Stimulation/ Sensing Materials for Pacemaker Electrode Applications: III. Nanoporous and Smooth Carbon Electrodes”. In: *Journal of the Electrochemical Society* 152.9 (2005), J110. DOI: 10.1149/1.1972981.

[93] K. Stokes. “Cardiac pacing electrodes”. In: *Proceedings of the IEEE* 84.3 (1996), pp. 457–467. DOI: 10.1109/5.486747.

[94] X-FAB. *X-FAB: Your foundry partner for medical products*. URL: https://www.xfab.com/medical.

[95] James K. Russell David K. Hunt. *BIPHASIC DEFIBRILLATOR WAVEFORM WITH ADJUSTABLE SECOND PHASE TILT*. Patent US 2012/0123492 A1. May 2012.

[96] R Jacob Baker. *CMOS: circuit design, layout, and simulation*. John Wiley & Sons, 2019.

[97] Vratislav Michal. “On the low-power design, stability improvement and frequency estimation of the CMOS ring oscillator”. In: *Proceedings of 22nd International Conference Radioelektronika 2012*. IEEE. 2012, pp. 1–4.

[98] Ajay Kumar Mahato. “Ultra low frequency CMOS ring oscillator design”. In: *2014 Recent Advances in Engineering and Computational Sciences (RAECS)*. IEEE. 2014, pp. 1–5.

[99] Aman Shivhare and MK Gupta. “Low Power Ring Oscillator at 180nm CMOS Technology”. In: *International Journal of Computer Applications* 144.8 (2016), pp. 25–28.

[100] SK Dash et al. “Design of a Ring Oscillator for IoT Applications”. In: *2023 International Conference on Intelligent Data Communication Technologies and Internet of Things (IDCIoT)*. IEEE. 2023, pp. 101–104.

[101] Assad A Abidi. “Phase noise and jitter in CMOS ring oscillators”. In: *IEEE journal of solid-state circuits* 41.8 (2006), pp. 1803–1816.

[102] Orazio Aiello et al. “A pW-power Hz-range oscillator operating with a 0.3–1.8-V unregulated supply”. In: *IEEE Journal of Solid-State Circuits* 54.5 (2019), pp. 1487–1496.

[103] Giuseppe De Vita, Francesco Marraccini, and Giuseppe Iannaccone. “Low-voltage low-power CMOS oscillator with low temperature and process sensitivity”. In: *2007 IEEE International Symposium on Circuits and Systems*. IEEE. 2007, pp. 2152–2155.

[104] Urs Denier. “Analysis and design of an ultralow-power CMOS relaxation oscillator”. In: *IEEE Transactions on Circuits and Systems I: Regular Papers* 57.8 (2010), pp. 1973–1982.

[105] Yusuke Tokunaga et al. “An on-chip CMOS relaxation oscillator with voltage averaging feedback”. In: *IEEE Journal of Solid-State Circuits* 45.6 (2010), pp. 1150–1158.

[106] Hui Wang and Patrick P Mercier. “A 1.6%/V 124.2 pW 9.3 Hz relaxation oscillator featuring a 49.7 pW voltage and current reference generator”. In: *ESSCIRC 2017-43rd IEEE European Solid State Circuits Conference*. IEEE. 2017, pp. 99–102.

[107] William Teles Medeiros, Hamilton Klimach, and Sergio Bampi. “A 40 nW 32.7 kHz CMOS Relaxation Oscillator with Comparator Offset Cancellation for Ultra-Low Power applications”. In: *2020 IEEE 11th Latin American Symposium on Circuits & Systems (LASCAS)*. IEEE. 2020, pp. 1–4.

[108] Yuchi Ni. “Low-power CMOS relaxation oscillator design with an on-chip circuit for combined temperature-compensated reference voltage and current generation”. PhD thesis. Northeastern University, 2013.

[109] A Priasmoro. “Ultra Low Power Crystal Oscillators”. In: (2005).

[110] Li Xu, David Blaauw, and Dennis Sylvester. “Ultra-Low Power 32kHz Crystal Oscillators: Fundamentals and Design Techniques”. In: *IEEE Open Journal of the Solid-State Circuits Society* 1 (2021), pp. 79–93.

[111] AM Korolev, VM Shulga, and OG Turutanov. “Ultra-low supply voltage crystal quartz oscillator”. In: *Review of Scientific Instruments* 92.5 (2021).

[112] Tzu-Ming Wang, Ming-Dou Ker, and Hung-Tai Liao. “Design of Mixed-Voltage-Tolerant Crystal Oscillator Circuit in Low-Voltage CMOS Technology”. In: *IEEE Transactions on Circuits and Systems I: Regular Papers* 56 (2009), pp. 966–974. URL: https://api.semanticscholar.org/CorpusID:105389.

[113] Keng-Jan Hsiao. “17.7 A 1.89nW/0.15V self-charged XO for real-time clock generation”. In: *2014 IEEE International Solid-State Circuits Conference Digest of Technical Papers (ISSCC)* (2014), pp. 298–299. URL: https://api.semanticscholar.org/CorpusID:46095266.

[114] Hani Esmaeelzadeh and Sudhakar Pamarti. “A Sub-nW 32-kHz Crystal Oscillator Architecture Based on a DC-Only Sustaining Amplifier”. In: *IEEE Journal of Solid-State Circuits* 54.12 (2019), pp. 3247–3256. DOI: 10.1109/JSSC.2019.2942365.

[115] Alice Wang, Benton Calhoun, and Anantha Chandrakasan. *Sub-threshold Design for Ultra Low-Power Systems*. Springer New York, NY, Jan. 2006. ISBN: 978-0-387-33515-5. DOI: 10.1007/978-0-387-34501-7.

[116] David Bol et al. “Building Ultra-Low-Power Low-Frequency Digital Circuits with High-Speed Devices”. In: *2007 14th IEEE International Conference on Electronics, Circuits and Systems*. 2007, pp. 1404–1407. DOI: 10.1109/ICECS.2007.4511262.

[117] Wootaek Lim. “Ultra-Low Power Circuit Design for Miniaturized IoT Platform”. PhD thesis. 2018.

[118] Jan Rabaey. *Low Power Design Essentials*. Springer New York, NY, 2009. ISBN: 978-0-387-71712-8. DOI: https://doi.org/10.1007/978-0-387-71713-5.

[119] Johaira M. Maute et al. “Design Implementation of 10T Static Random Access Memory Cell Using Stacked Transistors for Power Dissipation Reduction”. In: *2018 IEEE 10th International Conference on Humanoid, Nanotechnology, Information Technology,Communication and Control, Environment and Management (HNICEM)*. 2018, pp. 1–6. DOI: 10.1109/HNICEM.2018.8666355.

[120] Mahfuzul Islam et al. “Wide-Supply-Range All-Digital Leakage Variation Sensor for On-Chip Process and Temperature Monitoring”. In: *Proceedings - 2014 IEEE Asian Solid-State Circuits Conference, A-SSCC 2014* 50 (Jan. 2015), pp. 45–48. DOI: 10.1109/ASSCC.2014.7008856.

[121] Jorge Tonfat, Guilherme Flach, and Ricardo Reis. “Leakage current analysis in static CMOS logic gates for a transistor network design approach”. In: *2016 26th International Workshop on Power and Timing Modeling, Optimization and Simulation (PATMOS)*. 2016, pp. 107–113. DOI: 10.1109/PATMOS.2016.7833673.

[122] Behzad Razavi. *Design of Analog CMOS Integrated Circuits*. 1st ed. USA: McGraw-Hill, Inc., 2000. Chap. 7 Noise, pp. 234–236. ISBN: 0072380322.

[123] Theodore C Chan and Taylor Y Cardall. “Electronic pacemakers”. In: *Emergency Medicine Clinics* 24.1 (2006), pp. 179–194.

[124] P. Kalyani, Dr. M. Madhavi Latha, and Dr. P. Chandra Sekhar. “Analysis of MOS transistor behavior with Forward and Reverse Body biasing in Subthreshold region”. In: 2018. URL: https://api.semanticscholar.org/CorpusID:212670755.

[125] Pavan Bikki and Karuppanan Pi. “SRAM Cell Leakage Control Techniques for Ultra Low Power Application: A Survey”. In: *Circuits and Systems* 08 (Jan. 2017), pp. 23–52. DOI: 10.4236/cs.2017.82003.

[126] A. Keshavarzi et al. “Effectiveness of reverse body bias for leakage control in scaled dual Vt CMOS ICs”. In: *ISLPED’01: Proceedings of the 2001 International Symposium on Low Power Electronics and Design (IEEE Cat. No.01TH8581)*. 2001, pp. 207–212. DOI: 10.1109/LPE.2001.945402.

[127] Orazio Aiello, Paolo Crovetti, and Massimo Alioto. “A Sub-Leakage PW-Power HZ-Range Relaxation Oscillator Operating with 0.3V-1.8V Unregulated Supply”. In: *2018 IEEE Symposium on VLSI Circuits*. 2018, pp. 119–120. DOI: 10.1109/VLSIC.2018.8502413.

[128] Jorge Cañada et al. “An On-Chip Ultra-Low-Power Hz-Range Ring Oscillator Based on Dynamic Leakage Suppression Logic”. In: *2020 35th International Technical Conference on Circuits/Systems, Computers and Communications (ITC-CSCC)*. 2020, pp. 378–383.

[129] David Bol et al. “Building ultra-low-power high-temperature digital circuits in standard high-performance SOI technology”. In: *Solid-State Electronics* 52 (Dec. 2008), pp. 1939–1945. DOI: 10.1016/j.sse.2008.06.045.

[130] Wootaek Lim et al. “8.2 Batteryless Sub-nW Cortex-M0+ processor with dynamic leakage-suppression logic”. In: *2015 IEEE International Solid-State Circuits Conference-(ISSCC) Digest of Technical Papers*. IEEE. 2015, pp. 1–3.

[131] S.M. Kang and Y. Leblebici. *CMOS Digital Integrated Circuits: Analysis and Design*. CMOS Digital Integrated Circuits: Analysis and Design. McGraw-Hill, 2003. Chap. 7 COMBINATIONAL MOS LOGIC CIRCUITS, pp. 266–273. ISBN: 9780072460537. URL: https://books.google.fr/books?id=gRBGAQAAIAAJ.

[132] Tetsuya Hirose et al. “A nano-ampere current reference circuit and its temperature dependence control by using temperature characteristics of carrier mobilities”. In: *2010 Proceedings of ESSCIRC*. 2010, pp. 114–117. DOI: 10.1109/ESSCIRC.2010.5619819.

[133] Battu Balaji Yadav et al. “67ppm/°C, 66nA PVT Invariant Curvature Compensated Current Reference for Ultra-Low Power Applications”. In: *2020 IEEE International Symposium on Circuits and Systems (ISCAS)*. 2020, pp. 1–5. DOI: 10.1109/ISCAS45731.2020.9180857.

[134] Alexander J. Casson and Esther Rodriguez-Villegas. “A 60 pW g_mC Continuous Wavelet Transform Circuit for Portable EEG Systems”. In: *IEEE Journal of Solid-State Circuits* 46.6 (2011), pp. 1406–1415. DOI: 10.1109/JSSC.2011.2125010.

[135] Priyesh Gandhi and Nirnjan Devashrayee. “A novel low offset low power CMOS dynamic comparator”. In: *Analog Integrated Circuits and Signal Processing* 96 (July 2018). DOI: 10.1007/s10470-018-1166-9.

[136] Pradeep Jinka and Ramashri Tirumala. “Design of low power dynamic comparator with reduced kickback noise technique for bio-medical applications”. In: *e-Prime - Advances in Electrical Engineering, Electronics and Energy* 6 (2023), p. 100336. ISSN: 2772-6711. DOI: https://doi.org/10.1016/j.prime.2023.100336. URL: https://www.sciencedirect.com/science/article/pii/S2772671123002310.

[137] Ryo Matsuzuka et al. “An 80-mV-to-1.8-V Conversion-Range Low-Energy Level Shifter for Extremely Low-Voltage VLSIs”. In: *IEEE Transactions on Circuits and Systems I: Regular Papers* 64.8 (2017), pp. 2026–2035. DOI: 10.1109/TCSI.2017.2682320.

[138] Joel Gak, Matías Miguez, and Alfredo Arnaud. “CMOS level shifters from 0 to 18 V output”. In: *Analog Integrated Circuits and Signal Processing* 107 (June 2021). DOI: 10.1007/s10470-021-01827-w.

[139] Gaetano Palumbo and Domenico Pappalardo. “Charge Pump Circuits: An Overview on Design Strategies and Topologies”. In: *IEEE Circuits and Systems Magazine* 10.1 (2010), pp. 31–45. DOI: 10.1109/MCAS.2009.935695.

[140] Andrea Ballo, Alfio Grasso, and Gaetano Palumbo. “A Review of Charge Pump Topologies for the Power Management of IoT Nodes”. In: *Electronics* 8 (Apr. 2019). DOI: 10.3390/electronics8050480.

[141] Ya-Chun Huang, Ming-Dou Ker, and Chun-Yu Lin. “Design of negative high voltage generator for biphasic stimulator with soc integration consideration”. In: *2012 IEEE Biomedical Circuits and Systems Conference (BioCAS)*. 2012, pp. 29–32. DOI: 10.1109/BioCAS.2012.6418477.

[142] Liang Zhang, Xu Cheng, and Xianjin Deng. “A modified Dickson’s charge pump circuit with high output voltage and high pumping efficiency”. In: *Analog Integrated Circuits and Signal Processing* 101 (Dec. 2019). DOI: 10.1007/s10470-019-01531-w.

[143] Andrea Ballo et al. “A Charge Loss Aware Advanced Model of Dickson Voltage Multipliers”. In: *IEEE Access* PP (Jan. 2022), pp. 1–1. DOI: 10.1109/ACCESS.2022.3218901.

[144] J.F. Dickson. “On-chip high-voltage generation in MNOS integrated circuits using an improved voltage multiplier technique”. In: *IEEE Journal of Solid-State Circuits* 11.3 (1976), pp. 374–378. DOI: 10.1109/JSSC.1976.1050739.

[145] Mingliang Liu. *Demystifying Switched-Capacitor Circuits*. Jan. 2006. DOI: 10.1016/B978-0-7506-7907-7.X5011-0.

[146] Huan Peng et al. “CMOS Startup Charge Pump With Body Bias and Backward Control for Energy Harvesting Step-Up Converters”. In: *Circuits and Systems I: Regular Papers, IEEE Transactions on* 61 (June 2014), pp. 1618–1628. DOI: 10.1109/TCSI.2013.2290823.

[147] G. Palumbo and D. Pappalardo. “Charge pump circuits with only capacitive loads: optimized design”. In: *IEEE Transactions on Circuits and Systems II: Express Briefs* 53.2 (2006), pp. 128–132. DOI: 10.1109/TCSII.2005.855732.

[148] Hazem H. Hammam, Khaled M. Hassan, and Sameh A. Ibrahim. “An Ultra-Low-Power Process-and- Temperature Compensated Ring Oscillator”. In: *2022 9th International Conference on Electrical and Electronics Engineering (ICEEE)*. 2022, pp. 1–5. DOI: 10.1109/ICEEE55327.2022.9772521.

[149] Abbott. *Optimizing Device Longevity*. URL: https://www.cardiovascular.abbott/content/dam/cv/cardiovascular/pdf/guides/TI-Optimizing-Device-Longevity-Rev-D-May-2017.pdf.